SURFACE SCIENCE STUDIES OF STRONG METAL-SUPPORT INTERACTIONS IN HETEROGENEOUS CATALYSTS

by

Junxian Gao

A Dissertation

Submitted to the Faculty of Purdue University

In Partial Fulfillment of the Requirements for the degree of

Doctor of Philosophy

Davidson School of Chemical Engineering

West Lafayette, Indiana

May 2022

THE PURDUE UNIVERSITY GRADUATE SCHOOL

STATEMENT OF COMMITTEE APPROVAL

Dr. Jeffrey T. Miller, Chair

Davidson School of Chemical Engineering

Dr. Jeffrey P. Greeley

Davidson School of Chemical Engineering

Dr. Rajamani Gounder

Davidson School of Chemical Engineering

Dr. Dmitry Y. Zemlyanov

Birck Nanotechnology Center

Approved by:

Dr. John. A. Morgan

To my family and loved ones

ACKNOWLEDGMENTS

My Ph.D. experience has been an amazing and valuable journey. I enjoyed the time performing research with talented people and the life in West Lafayette. The completion of my Ph.D. would have not been possible without the mentoring, help, and support from others, so I would like to show my sincere gratitude to these people.

First and foremost, it was my fortune to have Dr. Jeffrey Miller as my advisor. Ph.D. could be a stressful journey for most graduate students, but my advisor made it less stressful for me. Before joining Jeff's group, I could have never imagined that a professor would spend many hours to teach students to analyze data in person. He is so friendly, just as he always says that he is "our colleague, not our supervisor". He gave me freedom to perform research independently, while always asked key scientific questions to keep me on track towards the completion of projects. He also taught me how to prepare ahead, prioritize tasks, and give good presentations. These skills benefited my Ph.D. study a lot and will keep benefiting my future career.

I am also very grateful to Dr. Dmitry Zemlyanov. He is a great mentor during my time at Purdue. He taught me the knowledge of surface science, how to perform UHV experiments (and how to catch Dima-style jokes). I also want to thank my collaborators, especially Dr. Jeffrey Greeley, Dr. Zhenhua Zeng, and Kaustubh Sawant, who worked on the SMSI project and helped to relate my experiments to theory. I would like to thank all my group members in Jeff's group, and my lab mate in Dima's lab. They are: Dr. Johnny Zhu Chen, Dr. Nicole Libretto, Dr. Laryssa Cesar, Dr. Stephen Purdy, Dr. Jiajing Kou, Dr. Rui Ma, Che-Wei Chang, Dr. Wenqing Zhang, Christopher Russell, Matthew Conrad, Arunima Saxena, David Dean, Chrisitan Breckner, Shan Jiang, and Dr. Lina Liu.

Finally, I want to thank my family, my boyfriend, and my friends. I am lucky to have true friends for ten years. My boyfriend has been supportive of me ever since my undergraduate time. My parents have given me so much love in my life. It has never been easy for them to support me from a small town to Beijing and then to the U.S. I have been away from home for many years, and I hope I will be able to meet them in person soon.

TABLE OF CONTENTS

LIST OF TABLES

LIST OF FIGURES

LIST OF ABBREVIATIONS

ALD (atomic layer deposition)

CVD (chemical vapor deposition)

DFT (density functional theory)

HREELS (high-resolution electron energy loss spectroscopy)

IR (infrared spectroscopy)

LEED (low electron energy diffraction)

LEIS (low energy He^+ ion scattering)

MS (mass spectrometry)

NPs (nanoparticles)

ORR (oxygen reduction reaction)

PVD (physical vapor deposition)

RIXS (resonant inelastic X-ray scattering)

SMSI (strong metal-support interaction)

STEM (scanning transmission electron microscopy)

STM (scanning tunneling microscopy)

TEM (transmission electron microscopy)

UHV (ultra-high vacuum)

XANES (X-ray absorption near edge structure)

XAS (X-ray absorption spectroscopy)

XPS (X-ray photoelectron spectroscopy)

XRD (X-ray diffraction)

ABSTRACT

The strong metal support interaction (SMSI) is among the best-known classes of metal-oxide interfacial interactions in heterogeneous catalysis, which is defined by the coverage of surface oxide on metal nanoparticles, forming a metal-oxide interface. However, there is limited insight in the atomic scale understanding of the structure of the SMSI oxide. In this work, surface science techniques including scanning tunneling microscopy (STM), X-ray photoelectron spectroscopy (XPS), high-resolution electron energy loss spectroscopy (HREELS) and low energy electron diffraction (LEED) were employed to investigate interfacial interactions in multiple catalytic systems, including ZnO-Pd, ZnO-Pt, and MoO_x-Pt. To utilize the capabilities of the surface science techniques and to mimic a catalytic metal nanoparticle in SMSI state, ultrathin oxide films were prepared on metal single crystals as inverse model catalysts.

The structural and chemical transformations of ultrathin zinc (hydroxy)oxide films on Pd(111) were studied under varying gas phase conditions (UHV, 5×10^{-7} mbar of O_2 and D_2/O_2 mixture). Under oxidative conditions, zinc oxide forms partially hydroxylated bilayer islands on Pd(111). Sequential treatments of the submonolayer ZnO_xH_y films in D_2/O_2 mixture (1:4) at 550 K evoked structural transformations from bilayer to monolayer and to a PdZn near-surface alloy, in accompany with the reduction of Zn, demonstrating that zinc oxide as a non-reducible oxide, can spread on metal surface and show an SMSI-like behavior in the presence of hydrogen. A mixed canonical – grand canonical phase diagram revealed that the monolayer intermediate structure is a metastable structure formed during the kinetic transformation, and the near-surface alloys are stable under the D_2/O_2 conditions. Grand canonical phase diagram predicted that under real SMSI conditions zinc oxide films on Pd nanoparticles would be stabilized by hydroxylation with stoichiometries such as ZnOH and $Zn_2O_3H_3$. Based on the experimental and theoretical observations, we propose that the mechanism of metal nanoparticle encapsulation involves both surface (hydroxy)oxide formation as well as alloy formation, depending on the environmental conditions.

Hydroxylation plays a more important role in the ZnO/Pt(111) system. Different from Pd(111), zinc oxide tends to form monolayer graphite-like ZnO films on Pt(111) under oxidative conditions at submonolayer coverages. This structure is extremely susceptible to hydroxylation at room temperature, leading to spontaneous formation of honeycomb-like $Zn_6O_5H_5$ films in

hydrogen. The interaction of the two distinct structures with Pt were investigated by XPS, STM, and HREELS with CO, C_2H_4, and NO as probe molecules. Zn exhibits a partially reduced oxidation state in $Zn_6O_5H_5$ and donates negative charge to surface Pt in the confined rings, leading to a switch from linear CO adsorption to bridged CO adsorption in accompany with a 50 cm^{-1} shift of ν(CO) towards lower frequencies. C_2H_4 readily forms ethylidyne (*CCH_3) species at room temperature once adsorbed on Pt(111), while the formation of ethylidyne is weakened on the $Zn_6O_5H_5$/Pt(111) surface. In summary, this study demonstrated a unique metal-hydroxide interaction, which serves as a novel approach for the modification of metal catalysts.

The partial coverage of metal surfaces by oxides could be utilized to passivate specific sites of catalysts, improving the activity and stability. Herein, we studied the structure of surface Mo oxides on Pt(111) and Pt(544) using STM, XPS, and HREELS. At 0.08 ML coverage, Mo oxide tends to form 1~2 nm clusters and the majority of Mo is in +5 oxidation state. The Mo oxide clusters tend to aggregate near the monoatomic Pt steps, showing a higher local density compared to the wide terraces. Therefore, our results provide experimental evidence for the site-selective growth of Mo oxides at step sites, which could prevent the leaching of active component in catalysts under real reaction conditions.

Overall, through atomic-level characterization of inverse model catalysts, we provided insights into the nature of metal-oxide interactions in multiple systems. The surface oxide films influence the property of metal surfaces in various ways, including migration, alloy formation, electronic perturbation, geometric confinement, and site-selective blocking. These findings emphasize the necessity of understanding the real structure of catalytic surfaces under different reaction conditions and shed light on rational design of oxide supported metal nanoparticle catalysts.

1. INTRODUCTION AND RESEARCH OBJECTIVES

1.1 Strong Metal-Support Interaction

Heterogeneous catalysts are used in numerous industrial processes, such as fuel upgrading[1], valuable chemicals production[2,3] and pollution reduction[4]. Many heterogenous catalysts are metal nanoparticles/clusters/atoms supported on metal oxides. Supports stabilize nanoparticles (NPs) and atoms, keeping a large catalytic surface area. Moreover, oxide supports are known to interact with metals in complex ways to modify the catalytic properties of the system. Although such effects have been studied for decades, the molecular-level interactions between the metal and the support, and the impact that these interactions have on catalytic properties, are not well understood. One of the most well-known and important cases is strong metal-support interaction (SMSI), which was first investigated forty years ago by Tauster *et al.*[5] It was observed that the chemisorption capacity of H_2 and CO on the titanium oxide supported metal NPs was considerably suppressed after reduction at 500 °C. Since this first report, multiple pairs of metals and reducible oxides have been found to show this phenomenon[6]. Electron microscopy has confirmed the existence of encapsulating layers consisting of modified support oxides on top of the metal NPs in various related cases (Figure 1.1) [7,8,9].

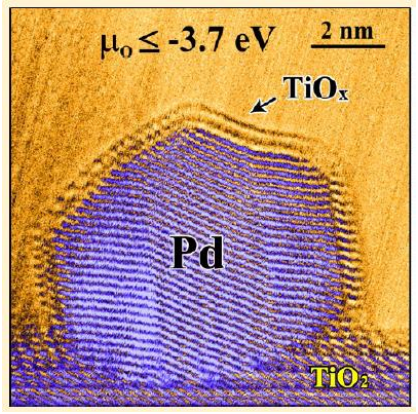

Figure 1.1. Transmission electron microscopy (TEM) image of a Pd/TiO_2 catalyst in SMSI state. Reprinted with permission from Ref 7. Copyright 2016 American Chemical Society.

Although historically SMSI was associated with blocking of catalytic sites, in certain circumstances the SMSI-state catalyst shows improved catalytic properties in various reactions[10].

Multiple explanations have been proposed to resolve the contradiction between blocked active sites and improved catalytic properties, including partial encapsulation of metal surfaces[11], adsorbate-permeable overlayers[12], electronic perturbation between metal and oxide[13,14,15], and alloy formation[16,17,18,19], etc., while each of the explanations may only be applied to a few cases. Moreover, dynamic changes of catalytic surface under reaction conditions can happen[7,20], adding extra complexity into the catalyst systems.

1.1.1 Partial encapsulation of metal surfaces

Originally SMSI is related to suppressed CO and H_2 adsorption measured at room temperature. Therefore, the number of metal active sites measured by CO adsorption becomes questionable. To quantify the metal-oxide interaction and to deconvolute the geometric and electronic effects in traditional SMSI systems, J. Z. Chen *et al.*[11] have studied Pt-Ti/SiO_2 and Pt-Nb/SiO_2 catalysts with ethylene hydrogenation and propane dehydrogenation as probe reactions. TEM showed that TiO_x species were widely dispersed over whole Pt particles, and CO chemisorption decreased by 80% after reduction at 550 °C, indicative of SMSI. XANES, XPS, and RIXS analyses showed that there are no significant changes in the energy of Pt 5d valence orbitals, i.e., electronic effect is excluded, which is also supported by the unchanged turnover rate. However, the conversion of ethylene hydrogenation averaged on the weight of Pt decreased, indicating that the surface covered by SMSI oxides is catalytically inert. In this case, the SMSI effect is solely geometric by decreasing the number of Pt atoms in ensemble sites, which results in the suppression of structure sensitive reactions such as hydrogenolysis.

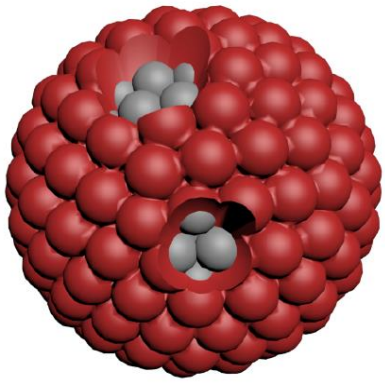

Figure 1.2. Schematics of the "partial coverage" model of the Pt-Ti and Pt-Nb catalysts in SMSI state (red: SMSI oxide, grey: exposed Pt). Reproduced from Ref. 11 with permission from the Royal Society of Chemistry.

1.1.2 Adsorbate-permeable overlayers

Previous studies indicated that even though the metal surfaces are covered by SMSI oxides, the exposure of at least a part of metal atoms is still necessary to enable catalytic reactions. This often contradicts with microscopic observations that the nanoparticles are completely encapsulated by several monolayers of oxides. J. C. Matsubu et al.[12] proposed adsorbate-induced formation of permeable encapsulation layer in Rh/TiO_2 and Rh/Nb_2O_5 catalysts. By studying the structure of Rh/TiO_2 catalyst using *in situ* STEM, it was found that treatment in 5% H_2 at 550 °C for 10 minutes induced the formation of a TiO_x crystalline bilayer (SMSI state) on Rh NPs, while treatment in 20% CO_2 and 2% H_2 at 250 °C for 3 hours resulted in the formation of an amorphous overlayer (A-SMSI state), as shown in Figure 1.3. The former crystalline layer contains exclusively Ti^{3+}, while the latter amorphous layer contains both Ti^{3+} and Ti^{4+}. By comparing the catalytic performance of SMSI Rh/Nb_2O_5 and A-SMSI Rh/Nb_2O_5 for CO_2 hydrogenation, it was found that SMSI formation decreased the production of CH_4 on Rh nanoparticles by 40-fold due to the physical blockage but did not change the production of CO on isolated Rh atoms. These results are consistent with J. Z. Chen et al.'s observation about SMSI on Pt/TiO_2 discussed in section 1.1.1. However, the A-SMSI formation suppressed CH_4 formation by 6-fold and increased CO production by 2.5-fold. The increase in reaction rate indicated that the A-SMSI layer is permeable to gaseous reactants and modifies the chemistry of Rh sites.

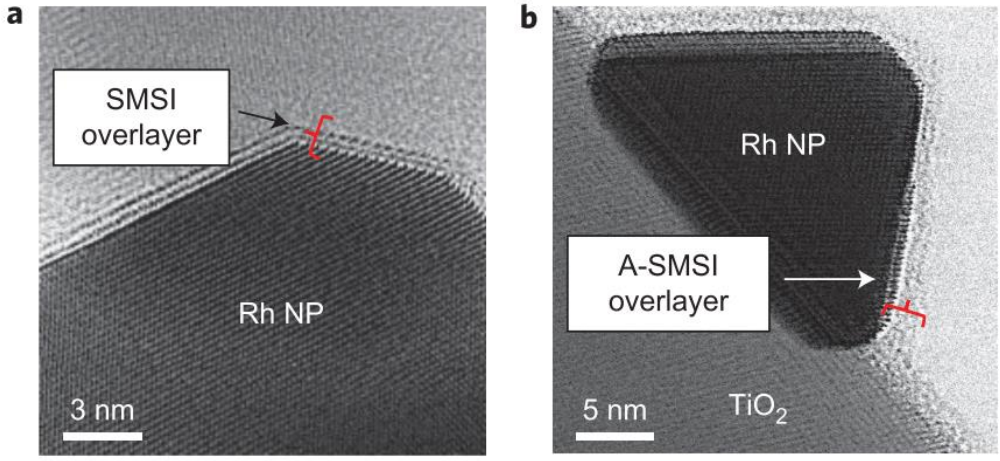

Figure 1.3. STEM images of Rh/TiO_2 catalyst in SMSI state (a) and A-SMSI state (b). Reprinted with permission from Ref. 12. Copyright 2017 Springer Nature.

1.1.3 Alloy formation

Aside from oxide supported metal catalysts, bimetallic catalysts have also been widely studied and utilized. Alloy formation was one of the first early hypotheses for the origin of SMSI[5], and later researchers leaned towards the oxide encapsulation model as evidenced by advanced microscopic studies. However, alloy formation and SMSI still share same features. Bimetallic alloy catalysts are often synthesized by high temperature reduction of noble metal NPs on metal oxide promoters[21], similar to the condition when oxide encapsulation would occur, and the core-shell structure is also consistent with the encapsulation model, although the overlayer composition is different. For example, Z. Wu *et al.*[22] found that the CO chemisorption capacity of Pt_3Mn intermetallic NPs was severely suppressed at room temperature but recovered at −100 °C. The core-shell NPs with Pt core and Pt_3Mn shell exhibited significantly higher selectivity towards propane dehydrogenation, compared to Pt NPs. It is worth noting that the origins of the suppressed CO adsorption are different for the two cases: on bimetallic alloys, the binding energy of CO is weakened due to the modified energy levels of metal valance orbitals, while on SMSI overlayer the metal sites are blocked by inert oxides. However, due to the limitation of characterization techniques, alloy formation sometimes can be mistakenly interpreted as SMSI effect.

1.1.4 Dynamic changes of catalytic surfaces

Many catalysts are pretreated before reactions to form the desired active components. For SMSI-related catalysts, the most common pretreatment is the reduction by pure or diluted H_2 at elevated temperatures. In literature, the structure of the pretreated catalysts is usually characterized by multiple techniques such as TEM, XPS, IR, XAS, etc., while the structure of the used catalysts is paid less attention. In fact, the active sites may undergo further modifications when the environment is switched from pretreatment to reactants at the initial stage. This also applies to SMSI catalysts. T. Lunkenberin *et al.*[20] discovered that the industrial $Cu/ZnO/Al_2O_3$ catalyst formed a ZnO overlayer on the surface of Cu nanoparticles after reduction in H_2. Moreover, such a ZnO overlayer underwent a structural transformation during the HRTEM measurement. Upon the exposure to the electron beam, the overlayer transformed from a graphitic-like phase to the rock salt phase and eventually to the wurtzite phase. D. Li *et al.*[23] studied the kinetics of SMSI of the commercial $Cu/ZnO/Al_2O_3$ catalyst by changing the gas composition and treatment time. Treating the catalyst in H_2/N_2 for 60 minutes resulted in discrete

Cu and ZnO nanoparticles, but the reactants (H_2O and CH_3OH) could facilitate SMSI. Treatment in H_2/N_2 for 50 minutes and then in a $H_2/H_2O/CH_3OH/N_2$ mixture for 10 minutes resulted in the formation of thin ZnO_x overlayers on Cu nanoparticles, while treatment in the $H_2/H_2O/CH_3OH/N_2$ mixture directly for 60 minutes led to thicker ZnO_x overlayers. This finding suggests that the formation of the SMSI overlayer did not reach the equilibrium state and might continue to change with time. In short, these discoveries suggest that often the SMSI processes are not in equilibrium, and the SMSI overlayers are not always thermodynamically stable. Thus, real reaction conditions should be taken into consideration when defining the real active sites.

1.2 Planar Model Catalysts

Atomic-level understanding of such metal-oxide interactions are necessary to identify the pathway of oxide migration and formation of SMSI overlayers, the surface structure and active sites of SMSI catalyst, and the mechanism of catalytic reactions at active sites. With deeper understanding of the nature of SMSI, one can tailor the catalytic surface in a more accurate and effective way to boost the catalytic activity and selectivity towards desired products.

The complexity of technical porous oxide supported metal catalysts makes it difficult to gain a fundamental understanding of the metal-oxide interaction at an atomic level[24]. In a technical catalyst, catalytic surface is hidden inside of porous support, and it is difficult to investigate with modern research tools. Common characterization techniques such as synchrotron X-ray diffraction (XRD), X-ray adsorption spectroscopy (XAS), etc. give the average bulk information of metal NPs, due to the strong penetrating ability of X-ray. X-ray photoelectron spectroscopy (XPS) is regarded as a surface-sensitive technique, but the depth of analysis for XPS measurements is also several nanometers, providing blended information on both surface and bulk chemistry of metal NPs. A powerful tool to obtain chemical information of metal catalyst surfaces is *in situ* infrared spectroscopy (IR) in combination with probe molecules such as CO and H_2 [25], however, this technique is infeasible for study of SMSI due to the low chemisorption of CO and H_2.

To overcome disadvantages of porous technical catalyst, planar model catalysts have served as a powerful tool to study the growth, migration, and structure of oxide thin films on metal surfaces. Planar model catalysts are metal nanoparticles deposited on the flat oxide

supports (conventional model catalysts) or thin oxide films deposited on metal single crystal surfaces (inverse model catalysts). This approach allows researchers to control catalyst preparation more precisely and to use powerful surface science characterization methods to investigate metal-oxide interactions. The boundary between metal nanoparticles and oxide support can play important role in catalytic process[26], but its contribution to the overall measured signal can be very low. To overcome this obstacle, inverse model catalyst can be used to maximize the perimeter of metal-oxide boundary so that it can be profitable for the investigation of metal-oxide interactions.

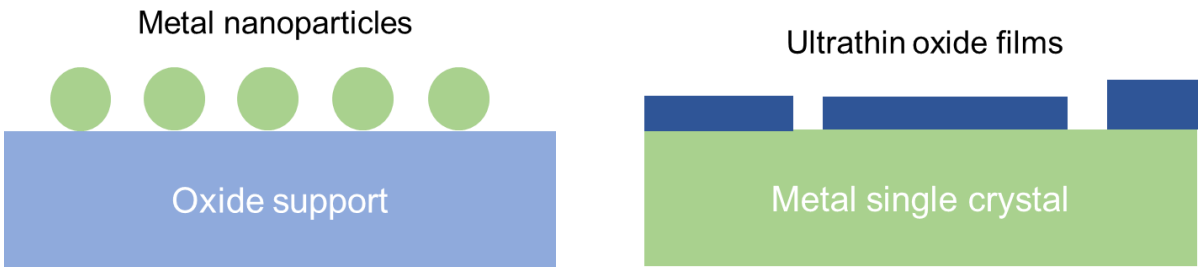

Figure 1.4. Schematic models of conventional model catalyst (left) and inverse model catalyst (right).

Surface science studies on model catalysts have demonstrated the encapsulation of metal nanoparticles by partially reduced oxides in SMSI systems. O. Dulub *et al.*[27] synthesized Pt clusters on TiO_2(110) and annealed it in ultra-high vacuum (UHV) up to 973 K. A complete encapsulation of Pt clusters with reduced titanium oxide layer was confirmed by scanning tunneling microscopy (STM) and low energy He^+ ion scattering (LEIS). For Pd/TiO_2(110), M. Bowker *et al.*[28] observed two different well-ordered structures of the overlayer formed at the surface of Pd NPs (~10 nm diameter) after annealing above 800 K, and CO adsorption was decreased by annealing above 600 K, a typical characteristic of SMSI. XPS indicated the overlayer was partially reduced titanium oxide. Marc G. Willinger *et al.*[29] used high-resolution transmission electron microscopy (HRTEM) to demonstrate that Pt NPs supported on a well-ordered Fe_3O_4 thin film undergo encapsulation by FeO overlayers after annealing in UHV to 850 K. Scanning transmission electron microscopy (STEM) images revealed substantial contrast variation in the regions surrounding Pt NPs, favoring the hypothesis that encapsulation proceeds through surface migration of Fe species from the oxide onto the Pt NP surface against migration through the particle (via alloying). This model catalyst also showed suppressed CO adsorption

but increased CO_2 production rate in catalytic CO oxidation, as compared to bare Pt NPs on Fe_3O_4(111) film without the FeO(111) overlayer[30].

1.3 SMSI of irreducible oxides: ZnO as an example

As discussed above, reduction in pure or diluted H_2 is usually required to evoke the formation of SMSI overlayer[31]. Although UHV annealing is often used alternatively in surface science studies, the effect of residual hydrogen in a UHV chamber cannot be ruled out. The SMSI overlayer has a stoichiometry different from corresponding bulk, and the metal cation in the over layer exhibits a lower oxidation state than that in the oxide support. Thus, the oxide support around metal NPs must be partially reduced before migrating over the metal surface[32], either through reacting with H_2 and forming H_2O, or decomposing and desorbing O_2 in the vacuum. The former pathway also requires reactivity of the metal towards H_2 activation.

J. Schoiswohl *et al.*[33] investigated the structural transformations and mass transport of submonolayer vanadium oxide on Pd(111) and Rh(111). Varying from UHV to O_2 atmosphere at 523 K, vanadium oxide on Pd(111) transformed from (2×2) s-V_2O_3 phase into (4×4) V_5O_{14} phase; pumping out O_2 resulted in a zigzag V_6O_{14} phase, and with a H_2 dose it was reduced into the initial (2×2) s-V_2O_3 phase. By exposing V-oxide/Rh(111) to H_2 at 673 K, they observed a sequence of structures going from V^{5+} to V^{2+} phase, and initial oxide film condensed into more compact islands. Mobile V_6O_{12} clusters were also observed to effectuate the mass transport of oxide on Rh(111) surface. The discovery of such a partially reduced oxide mobile species reinforced the observation that only reducible oxides can show SMSI[6,34], and diffusive MO_x species (M: Ti,[31] Nb,[12] Mn,[35] Fe,[29] where *x* is smaller than the bulk stoichiometry number) are necessary to enable migration of oxide supports.

Recently, non-reducible oxide like ZnO, has also been reported for such an SMSI effect in Cu/ZnO-base catalysts for methanol synthesis[36,37]. M. Behrens *et al.* observed disordered ZnO_x overlayer in highly active Cu/ZnO/Al_2O_3 catalyst at a low partial pressure of hydrogen by HRTEM[38]. T. Lunkenbein *et al.* reported that the ZnO_x overlayer on Cu NP transformed from graphite-like ZnO_x to rock salt ZnO and eventually wurtzite ZnO structure upon electron beam exposure[20]. Depolarized graphite-like overlayer structure was also predicted[39] and observed in ZnO/Ag (111)[40] and ZnO/Pd (111)[41] inverse model catalysts. IR and theoretical analysis

performed by Schott *et al.* suggested that ZnO overlayer showed different chemical properties from the wurtzite bulk structure and seemed to be partially reduced to a less strongly oxidized $Zn^{\delta+}$ state though SMSI[42]. These findings indicate that the structure of ZnO overlayers on metal surfaces is highly dynamic and that SMSI may be observed even on non-reducible oxides. Therefore, a systematic study of the composition, structure, and dynamic changes of ZnO ultrathin films on metal surfaces is required to answer multiple questions:

First, what are the composition and structure of ZnO_x overlayer?

Second, what is the origin of the $Zn^{\delta+}$ oxidation state?

Third, what are the driving force and pathway of zinc oxide migration on metal surfaces?

1.4 Dissertation overview

The goal of this dissertation is to investigate the fundamentals of metal-oxide interactions in the context of SMSI in heterogeneous catalysis. The first two chapters are focused on the studies about zinc oxide ultrathin films on Pd(111) and Pt(111) surfaces, aiming to answer the above questions about the nature of ZnO SMSI. The following chapter is focused on exploring the possibility of selective passivation of under-coordinated metal sites by oxides.

Chapter two presents the study of structural and chemical transformations of ultrathin ZnO films on a Pd(111) surface. In this study, the molecular-level features of the dynamic structural transformations of ZnO on Pd(111), and the general thermodynamic driving force of the SMSI behavior, were investigated by studying the ZnO/Pd(111) inverse model catalyst using surface analysis techniques and DFT calculations. Zinc oxide tends to form partially hydroxylated bilayer islands on Pd(111) under oxidative conditions. Introduction of small amount of hydrogen resulted in the transformation of ZnO bilayer islands to surface and subsurface alloys through a newly discovered (18×18) R20° intermediate structure. Alloying, thus, serves as a driving force for the migration of Zn species on Pd surface.

Chapter three is focused on a comparative study of zinc oxide and zinc hydroxide on a Pt(111) surface. We prepared two ordered monolayer films, graphite-like (6×6)-ZnO and honeycomb-like (4×4)-$Zn_6O_5H_5$ on the Pt(111) surface separately, and studied the electronic and adsorption properties of the two surfaces. The ZnO film is a compact structure which blocks the underneath Pt, and barely affect the electronic property of surface Pt, as evidenced by HREELS

measurement of CO adsorption and desorption. In contrast, the $Zn_6O_5H_5$ film is an open structure which divides infinite Pt atoms into small ensembles, and donates negative charge to the surface Pt atoms, resulting in a change from linear CO adsorption to bridged CO adsorption, in accompany with shifted ν(CO) frequencies. In short, the $Zn_6O_5H_5$ demonstrates a unique metal-hydroxide interaction which tunes the surface properties of Pt.

Chapter four explored the possibility of selective passivation of under-coordinated step sites by oxides, as demonstrated by forming molybdenum oxides on Pt(111) and Pt(544) surfaces. Mo was e-beam evaporated onto the single crystal surfaces and treated under oxidative conditions. As evidenced by STM and XPS, Mo forms 1-2 nm clusters on Pt surfaces and mainly presents as Mo^{5+}. The clusters appear on both terraces and steps, but favorably agglomerate near steps, giving a higher local density. Therefore, it is demonstrated that Mo oxide can selectively passivate step sites. This study provides experimental evidence for the site-selective growth of Mo oxides and explains why Mo doping could improve the stability of Pt-based electrocatalysts.

Chapter five is a summary and outlook for potential future studies inspired by this work. The topics of interest include: 1) structure sensitivity of ZnO SMSI; 2) tuning the porosity of SMSI overlayer in technical catalysts; 3) improving the site selectivity of oxide deposition on metals.

1.5 References

(1) Fisk, C. A.; Morgan, T.; Ji, Y.; Crocker, M.; Crofcheck, C.; Lewis, S. A. Bio-Oil Upgrading over Platinum Catalysts Using in Situ Generated Hydrogen. *Appl. Catal. A Gen.* **2009**, *358*, 150–156.

(2) Zhou, C. H.; Beltramini, J. N.; Fan, Y. X.; Lu, G. Q. Chemoselective Catalytic Conversion of Glycerol as a Biorenewable Source to Valuable Commodity Chemicals. *Chem. Soc. Rev.* **2008**, *37*, 527–549.

(3) Gallezot, P. Catalytic Routes from Renewables to Fine Chemicals. *Catal. Today* **2007**, *121*, 76–91.

(4) Gandhi, H. S.; Graham, G. W.; McCabe, R. W. Automotive Exhaust Catalysis. *J. Catal.* **2003**, *216*, 433–442.

(5) Tauster, S. J.; Fung, S. C.; Garten, R. L. Strong Metal-Support Interactions. Group 8 Noble Metals Supported on TiO_2. *J. Am. Chem. Soc.* **1978**, *100*, 170–175.

(6) Tauster, S. J. Strong Interactions in Supported-Metal Catalysts. *Science.* **1981**, *211*, 1121–1125.

(7) Zhang, S.; Plessow, P. N.; Willis, J. J.; Dai, S.; Xu, M.; Graham, G. W.; Cargnello, M.; Abild-Pedersen, F.; Pan, X. Dynamical Observation and Detailed Description of Catalysts under Strong Metal-Support Interaction. *Nano Lett.* **2016**, *16*, 4528–4534.

(8) Bernal, S.; Botana, F. J.; Calvino, J. J.; López, C.; Pérez-Omil, J. A.; Rodríguez-Izquierdo, J. M. High-Resolution Electron Microscopy Investigation of Metal-Support Interactions in Rh/TiO_2. *J. Chem. Soc. Faraday Trans.* **1996**, *92*, 2799–2809.

(9) Shi, X. Y.; Zhang, W.; Zhang, C.; Zheng, W. T.; Chen, H.; Qi, J. G. Real-Space Observation of Strong Metal-Support Interaction: State-of-the-Art and What's the Next. *J. Microsc.* **2016**, *262*, 203–215.

(10) van Deelen, T. W.; Hernández Mejía, C.; de Jong, K. P. Control of Metal-Support Interactions in Heterogeneous Catalysts to Enhance Activity and Selectivity. *Nat. Catal.* **2019**, *2*, 955–970.

(11) Zhu Chen, J.; Gao, J.; Probus, P. R.; Liu, W.; Wu, X.; Wegener, E. C.; Kropf, A. J.; Zemlyanov, D.; Zhang, G.; Yang, X.; Miller, J. T. The Effect of Strong Metal-Support Interaction (SMSI) on $Pt\text{-}Ti/SiO_2$ and $Pt\text{-}Nb/SiO_2$ catalysts for Propane Dehydrogenation. *Catal. Sci. Technol.* **2020**, *10*, 5973–5982.

(12) Matsubu, J. C.; Zhang, S.; DeRita, L.; Marinkovic, N. S.; Chen, J. G.; Graham, G. W.; Pan, X.; Christopher, P. Adsorbate-Mediated Strong Metal-Support Interactions in Oxide-Supported Rh Catalysts. *Nat. Chem.* **2017**, *9*, 120–127.

(13) Deng, L.; Miura, H.; Shishido, T.; Hosokawa, S.; Teramura, K.; Tanaka, T. Strong Metal-Support Interaction between Pt and SiO_2 Following High-Temperature Reduction: A Catalytic Interface for Propane Dehydrogenation. *Chem. Commun.* **2017**, *53*, 6937–6940.

(14) Du, L.; Qian, K.; Zhu, X.; Yan, X.; Kobayashi, H.; Liu, Z.; Lou, Y.; Li, R. Interface Engineering of Palladium and Zinc Oxide Nanorods with Strong Metal-Support Interactions for Enhanced Hydrogen Production from Base-Free Formaldehyde Solution. *J. Mater. Chem. A* **2019**, *7*, 8855–8864.

(15) Jung, H. K.; Eun, W. S.; Woo, J. K.; Jae, D. P.; Sang, H. M. Selective Hydrogenation of Acetylene on TiO_2-Added Pd Catalysts. *J. Catal.* **2002**, *208*, 310–320.

(16) Kast, P.; Friedrich, M.; Girgsdies, F.; Kröhnert, J.; Teschner, D.; Lunkenbein, T.; Behrens, M.; Schlögl, R. Strong Metal-Support Interaction and Alloying in Pd/ZnO Catalysts for CO Oxidation. *Catal. Today* **2016**, *260*, 21–31.

(17) Resasco, D. E.; Weber, R. S.; Sakellson, S.; McMillan, M.; Haller, G. L. X-Ray Absorption near-Edge Structure Evidence for Direct Metal-Metal Bonding and Electron Transfer in Reduced Rh/TiO_2 Catalysts. *J. Phys. Chem.* **1988**, *92*, 189–193.

(18) Boccuzzi, F.; Chiorino, A.; Ghiotti, G. IR Study of the CO Adsorption on Pt/ZnO Samples: Evidence for a PtZn Phase Formation in the SMSI State. *Surf. Sci.* **1989**, *209*, 77–88.

(19) Beck, A.; Huang, X.; Artiglia, L.; Zabilskiy, M.; Wang, X.; Rzepka, P.; Palagin, D.; Willinger, M. G.; van Bokhoven, J. A. The Dynamics of Overlayer Formation on Catalyst Nanoparticles and Strong Metal-Support Interaction. *Nat. Commun.* **2020**, *11*, 1–8.

(20) Lunkenbein, T.; Schumann, J.; Behrens, M.; Schlögl, R.; Willinger, M. G. Formation of a ZnO Overlayer in Industrial $Cu/ZnO/Al_2O_3$ Catalysts Induced by Strong Metal-Support Interactions. *Angew. Chemie. Int. Ed.* **2015**, *54*, 4544–4548.

(21) Dasgupta, A.; Rioux, R. M. Intermetallics in Catalysis: An Exciting Subset of Multimetallic Catalysts. *Catal. Today* **2019**, *330*, 2–15.

(22) Wu, Z.; Bukowski, B. C.; Li, Z.; Milligan, C.; Zhou, L.; Ma, T.; Wu, Y.; Ren, Y.; Ribeiro, F. H.; Delgass, W. N.; Greeley, J.; Zhang, G.; Miller, J. T. Changes in Catalytic and Adsorptive Properties of 2 Nm Pt_3Mn Nanoparticles by Subsurface Atoms. *J. Am. Chem. Soc.* **2018**, *140*, 14870–14877.

(23) Li, D.; Xu, F.; Tang, X.; Dai, S.; Pu, T.; Liu, X.; Tian, P.; Xuan, F.; Xu, Z.; Wachs, I. E.; Zhu, M. Induced Activation of the Commercial $Cu/ZnO/Al_2O_3$ Catalyst for the Steam Reforming of Methanol. *Nat. Catal.* **2022,** 5, 99-108.

(24) Rainer, D. R.; Xu, C.; Goodman, D. W. Characterization and Catalysis Studies of Small Metal Particles on Planar Model Oxide Supports. *J. Mol. Catal. A Chem.* **1997**, *119*, 307–325.

(25) Lamberti, C.; Zecchina, A.; Groppo, E.; Bordiga, S. Probing the Surfaces of Heterogeneous Catalysts by in Situ IR Spectroscopy. *Chem. Soc. Rev.* **2010**, *39*, 4951–5001.

(26) K. Hayek, R. Kramer, Z. P. Metal-Support Boundary Sites in Catalysis. *Appl. Catal. A Gen.* **1997**, *162*, 1–15.

(27) Dulub, O.; Hebenstreit, W.; Diebold, U. Imaging Cluster Surfaces with Atomic Resolution: The Strong Metal-Support Interaction State of Pt Supported on TiO_2(110). *Phys. Rev. Lett.* **2000**, *84*, 3646–3649.

(28) Bowker, M.; Stone, P.; Morrall, P.; Smith, R.; Bennett, R.; Perkins, N.; Kvon, R.; Pang, C.; Fourre, E.; Hall, M. Model Catalyst Studies of the Strong Metal-Support Interaction: Surface Structure Identified by STM on Pd Nanoparticles on TiO_2(110). *J. Catal.* **2005**, *234*, 172–181.

(29) Willinger, M. G.; Zhang, W.; Bondarchuk, O.; Shaikhutdinov, S.; Freund, H. J.; Schlögl, R. A Case of Strong Metal-Support Interactions: Combining Advanced Microscopy and Model Systems to Elucidate the Atomic Structure of Interfaces. *Angew. Chemie Int. Ed.* **2014**, *53*, 5998–6001.

(30) Lewandowski, M.; Sun, Y. N.; Qin, Z. H.; Shaikhutdinov, S.; Freund, H. J. Promotional Effect of Metal Encapsulation on Reactivity of Iron Oxide Supported Pt Catalysts. *Appl. Catal. A Gen.* **2011**, *391*, 407–410.

(31) Tauster, S. J. Strong Metal-Support Interactions. *Acc. Chem. Res.* **1987**, *20*, 389–394.

(32) Suzuki, T.; Souda, R. Encapsulation of Pd by the Supporting TiO2(110) Surface Induced by Strong Metal-Support Interactions. *Surf. Sci.* **2000**, *448*, 33–39.

(33) Schoiswohl, J.; Surnev, S.; Netzer, F. P. Reactions on Inverse Model Catalyst Surfaces: Atomic Views by STM. *Top. Catal.* **2005**, *36*, 91–105.

(34) Tauster, S. J.; Fung, S. C. Strong Metal-Support Interactions: Occurrence among the Binary Oxides of Groups IIA-VB. *J. Catal.* **1978**, *55*, 29–35.

(35) Baker, R. T. K.; Tauster, S. J.; Dumesic, J. A. Strong Metal-Support Interactions. *ACS Symp. Ser.* **1986**.

(36) Grunwaldt, J. D.; Molenbroek, A. M.; Topsøe, N. Y.; Topsøe, H.; Clausen, B. S. In Situ Investigations of Structural Changes in Cu/ZnO Catalysts. *J. Catal.* **2000**, *194*, 452–460.

(37) Naumann D'Alnoncourt, R.; Xia, X.; Strunk, J.; Löffler, E.; Hinrichsen, O.; Muhler, M. The Influence of Strongly Reducing Conditions on Strong Metal-Support Interactions in Cu/ZnO Catalysts Used for Methanol Synthesis. *Phys. Chem. Chem. Phys.* **2006**, *8*, 1525–1538.

(38) Behrens, M.; Studt, F.; Kasatkin, I.; Kühl, S.; Hävecker, M.; Abild-pedersen, F.; Zander, S.; Girgsdies, F.; Kurr, P.; Kniep, B.; Tovar, M.; Fischer, R. W.; Nørskov, J. K.; Schlögl, R. The Active Site of Methanol Synthesis over $Cu/ZnO/Al_2O_3$ Industrial Catalysts. *Science.* **2012**, *336*, 893–898.

(39) Claeyssens, F.; Freeman, C. L.; Allan, N. L.; Sun, Y.; Ashfold, M. N. R.; Harding, J. H. Growth of ZnO Thin Films - Experiment and Theory. *J. Mater. Chem.* **2005**, *15*, 139–148.

(40) Pan, Q.; Liu, B. H.; McBriarty, M. E.; Martynova, Y.; Groot, I. M. N.; Wang, S.; Bedzyk, M. J.; Shaikhutdinov, S.; Freund, H. J. Reactivity of Ultra-Thin ZnO Films Supported by Ag(111) and Cu(111): A Comparison to ZnO/Pt(111). *Catal. Letters* **2014**, *144*, 648–655.

(41) Weirum, G.; Barcaro, G.; Fortunelli, A.; Weber, F.; Schennach, R.; Surnev, S.; Netzer, F. P. Growth and Surface Structure of Zinc Oxide Layers on a Pd(111) Surface. *J. Phys. Chem. C* **2010**, *114*, 15432–15439.

(42) Schott, V.; Oberhofer, H.; Birkner, A.; Xu, M.; Wang, Y.; Muhler, M.; Reuter, K.; Wöll, C. Chemical Activity of Thin Oxide Layers: Strong Interactions with the Support Yield a New Thin-Film Phase of ZnO. *Angew. Chemie Int. Ed.* **2013**, *52*, 11925–11929.

2. STRUCTURAL AND CHEMICAL TRANSFORMATIONS OF ULTRATHIN ZINC OXIDE FILMS ON A PD(111) SURFACE

This chapter is reproduced from Gao, Junxian, *et al.* "Structural and chemical transformations of zinc oxide ultrathin films on Pd(111) surfaces." *ACS Applied Materials & Interfaces* 2021, 13, 29, 35113-35123. By permission from American Chemical Society. DOI: 10.1021/acsami.1c07510

2.1 Abstract

Structural and chemical transformations of ultrathin oxide films on transition metals lie at the heart of many complex phenomena in heterogeneous catalysis, such as the strong metal-support interaction. However, there is limited atomic scale understanding of these transformations, especially for irreducible oxides like ZnO. Here, by combining density functional theory (DFT) calculations and surface science techniques, including scanning tunneling microscopy (STM), x-ray photoelectron spectroscopy (XPS), high-resolution electron energy loss spectroscopy (HREELS), and low energy electron diffraction (LEED), we investigated the interfacial interaction of well-defined ultrathin ZnO_xH_y films on Pd(111) under varying gas phase conditions (UHV, 5×10^{-7} mbar of O_2 and D_2/O_2 mixture) to shed light on the SMSI effect of irreducible oxides. Sequential treatment of submonolayer zinc oxide films in a D_2/O_2 mixture (1:4) at 550 K evoked reversible structural transformations from bilayer to monolayer and further to a PdZn near-surface alloy, demonstrating that zinc oxide, as an irreducible oxide, can spread on metal surfaces and show an SMSI-like behavior in the presence of hydrogen. A mixed canonical – grand canonical phase diagram was developed to bridge the gap between UHV conditions and true SMSI environments, revealing that, in addition to surface alloy formation, certain ZnO_xH_y films with stoichiometries that do not exist in bulk are stabilized by Pd in the presence of hydrogen. Based on the combined theoretical and experimental observations, we propose that SMSI metal nanoparticle encapsulation for irreducible oxide supports such as ZnO involves both surface (hydroxy)oxide and surface alloy formation, depending on the environmental conditions.

2.2 Introduction

Catalytic activity of an oxide-supported transition metal catalyst is greatly influenced by the nature of metal-oxide interactions. The oxide supports are known to interact with the nanoparticles in highly complex and non-intuitive ways that fundamentally alter the catalytic properties of the system. Although such effects have been studied for decades, the atomic-level interactions between the metal and the support, and the impact that these interactions have on catalytic properties, are not well understood. In particular, the strong metal-support interaction (SMSI) was first investigated forty years ago by Tauster *et al*.[1] It was observed that the ability of titanium oxide-supported metal nanoparticles to bind adsorbates was considerably suppressed after heating at 500°C in a reducing atmosphere. Electron microscopy has confirmed the existence of an encapsulating layer consisting of modified support oxides on top of the metal nanoparticles in various related cases.[2,3] This encapsulation model is consistent with suppressed adsorption, but the model does not exclude other possible SMSI-related effects, including alloying and charge transfer. Although historically associated with coverage and deactivation of catalytic sites, recent developments suggest that, in certain circumstances, the SMSI oxide can modify catalytic active sites, resulting in improved catalytic properties.[4]

Despite many studies related to the electronic and geometric changes in the metal nanoparticles by the SMSI overlayer, and the impact of these effects on catalytic performance, the mechanism of the SMSI remains elusive. Reduction in pure or diluted H_2 is usually required for formation of SMSI overlayers.[5] The SMSI overlayer has a stoichiometry different from corresponding bulk phases, and the metal cation in the overlayer exhibits a lower oxidation state than that in the oxide supports, as observed using X-ray photoelectron spectroscopy (XPS).[6,7] Thus, the oxide support must be partially reduced before migrating over the metal nanoparticle surface,[8] either through reacting with H_2 and forming H_2O, or decomposing and desorbing O_2 in the vacuum. The former pathway also requires reactivity of the metal towards H_2 activation. The discovery of such partially reduced oxide overlayers has been interpreted to signify that only reducible oxides might show SMSI, where the metal cations can show multiple oxidation states; and diffusive MO_x species (M: Ti,[5] Nb,[9] Mn,[10] Fe,[7] where x is smaller than the bulk stoichiometry number) are necessary to enable migration of oxide supports onto the metal surface.

Recently, ZnO, a non-reducible oxide, has also been reported to exhibit an SMSI effect in Cu/ZnO-based catalysts during methanol synthesis.[11,12] M. Behrens *et al.* observed a disordered ZnO_x overlayer on a $Cu/ZnO/Al_2O_3$ catalyst at low partial pressure of hydrogen using high-resolution transmission electron microscopy (HRTEM).[13] T. Lunkenbein *et al.* reported that the ZnO_x overlayer on a Cu nanoparticle transformed from graphite-like ZnO_x to rocksalt ZnO and, eventually, wurtzite ZnO upon electron beam exposure.[14] Further, a depolarized graphite-like overlayer structure was predicted[15] and observed on ZnO/Ag(111)[16] and ZnO/Pd(111)[17] inverse model catalysts.[14] Infrared spectroscopy (IR) and theoretical analysis done by Schott *et al.* suggested that the ZnO overlayer showed different chemical properties compared to the wurtzite bulk structure and seemed to be partially reduced to a less strongly oxidized $Zn^{\delta+}$ state through SMSI.[18] These findings indicate that the structure of ZnO overlayers on metal surfaces is highly dynamic and that SMSI may be observed even on non-reducible oxides.

In the present study, the atomic-level features of the dynamic structural transformations of well-defined ZnO_xH_y ultrathin films on Pd(111) were investigated through surface science. Then, the extrapolation to the general thermodynamic driving forces of SMSI behavior were enabled through first-principles phase diagrams. We chose the current system because of the promising applications of Pd/ZnO catalysts to methanol synthesis and steam reforming of methanol.[19,20,21] Introduction of small amounts of hydrogen under UHV conditions resulted in the reduction of ZnO to surface ZnO_x and further to a PdZn near-surface alloy. By combining these observations with DFT calculations and a mixed canonical-grand canonical phase diagram, we deduced that small ensembles of ZnO on the surface are susceptible to reduction and will subsequently form subsurface alloys. The DFT calculations further demonstrate that certain ultrathin ZnO_xH_y films which are metastable in UHV can, in fact, become stable under SMSI conditions with a higher pressure of hydrogen. From these results, we propose that even irreducible oxides, such as ZnO, can exhibit SMSI-like behavior via favorable formation of ZnO_xH_y films or near-surface alloys, with a dependence on the gas phase conditions, that drives the migration of Zn over metal particles.

2.3 Experimental and computational methods

2.3.1 Experimental methods

All experiments were carried out in an Omicron surface analysis cluster consisting of two main UHV chambers. The preparation chamber (base pressure is ~6×10^{-10} mbar) is equipped with gas manifolds for chemical vapor deposition (CVD) and a Zn evaporator for physical vapor deposition (PVD). The analysis chamber (base pressure is ~6×10^{-11} mbar) is equipped with room temperature Omicron scanning tunneling microscopy (STM), X-ray photoelectron spectroscopy (XPS), high-resolution electron energy loss spectroscopy (HREELS), and low energy electron diffraction (LEED).

The Pd(111) single crystal was cleaned by cycles of Ar^+ sputtering, annealing in 1×10^{-6} mbar of O_2, and annealing in UHV. The cleanliness of the Pd(111) surface was monitored by XPS. ZnO films on Pd(111) were prepared by exposing the surface to diethylzinc at room temperature or by oxidative deposition of metallic Zn in 1×10^{-7} mbar of O_2, followed by post-oxidation in O_2 or a D_2/O_2 mixture at 550 K for 10 min. D_2 was used instead of H_2 throughout our experiments so that we could distinguish the external (intentional exposure) and internal (residual gas) sources of hydrogen by HREELS. The partial pressure of D_2 was calculated by taking into consideration the ionization parameter of the gas. The coverage of ZnO on Pd was controlled by diethylzinc (or metallic Zn) exposure and was calculated using the area of Zn $2p_{3/2}$ and Pd $3d_{5/2}$ XPS peaks under the assumption of a non-attenuating ZnO adlayer.[22] This approach has been well validated and is described in detail elsewhere.[23,24]

After ZnO preparation, the sample stage was cooled rapidly, and the sample was then transferred within 1-2 minutes to the analysis chamber for characterization by HREELS, STM, LEED and XPS. HREELS measurements were performed using an ELS 5000 (LK Technologies). The scattered electrons were collected in specular direction with primary electron beam energy of 5 eV. The FWHM of the elastic peak of the sample was between 2.5~3.0 meV (equivalent to 20~24 cm^{-1}). The intensity of energy loss was normalized to the intensity of the elastic peak.

XPS data were collected using a non-monochromatic Mg Kα x-ray source at an incidence angle of 45°. The emitted photoelectrons were collected using an Omicron EAC 125 analyzer and an Omicron EAC 2000 analyzer controller at a photoemission angle of 45° with respect to the surface normal. Binding energy (BE) values refer to the Fermi edge and the energy scale was calibrated using Au $4f_{7/2}$ at 84.0 eV and Cu $2p_{3/2}$ at 932.67 eV. Since the sample is conductive

and grounded, no charge correction was necessary. The Pd $3d_{5/2}$ peak for the clean Pd(111) surface was observed at 335.2 eV. XPS data were analyzed using CasaXPS software.

STM imaging was performed at a constant current mode at room temperature with tungsten tips, which were prepared by electrochemical etching of 0.25 mm (or 0.175 mm) tungsten wires and cleaned by electron bombardment in UHV. The bias voltage varied from +0.8 to +1.5 V with tunneling current ranging from 0.5 to 1.0 nA. STM images were analyzed using WSxM software.[25]

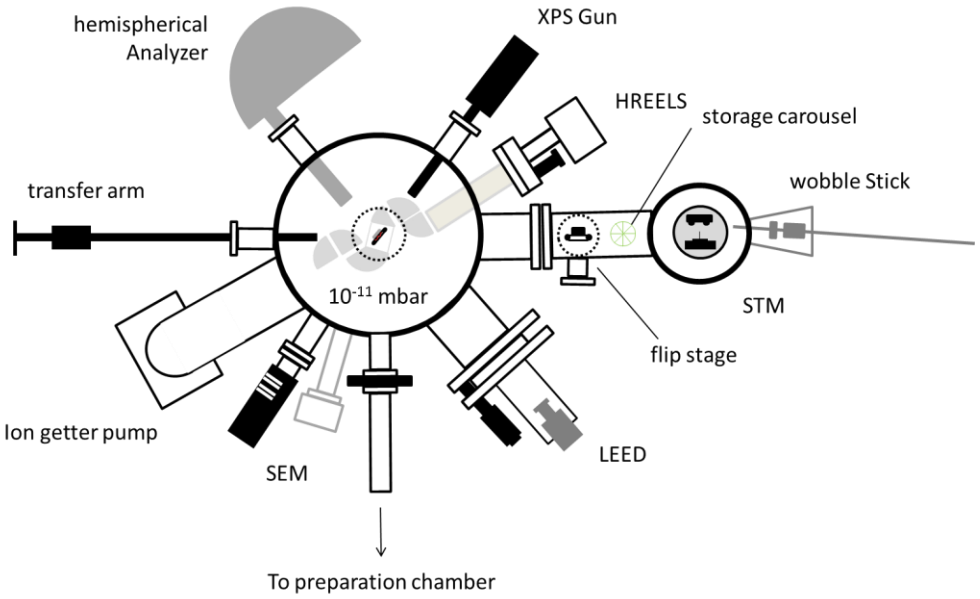

Figure 2.1. Schematic diagram of Omicron surface analysis cluster at Birck nanotechnology center, Purdue University.

2.3.2 Computational methods

Electronic structure calculations

Periodic Density Functional Theory (DFT) calculations were performed as implemented in Vienna *Ab Initio* Simulation Package (VASP)[26,27]. The core electrons were modeled using Projected Augmented Wave (PAW) potentials[28]. The generalized gradient approximation (GGA) developed by Perdew-Burke-Ernzerhof (PBE) was used as the exchange-correlation functional[29]. The energy cutoff for the planewave basis set was 500 eV. The Brillouin zone was sampled using Monkhorst-Pack. A large number of unique unit cells were studied, and we ensured in all cases that the lattice constant times number of K points was 30 Å. The substrates had four metal

layers with the bottom two constrained. A single K point and an orthorhombic unit cell was used for calculations involving gas phase species. The STM images were simulated using Atomic Simulation Environment (ASE) modules[30] and GPAW[31].

Geometric Structures

The ultrathin film structures were primarily made by cutting along different terminations of bulk structures. Since zinc has only one oxidation state (+2), there are only two stable bulk structures – ZnO and $Zn(OH)_2$. In order to study stoichiometries that do not exist in bulk, terminations from stable bulk crystalline polymorphs, such as TiO_2, V_2O_3, LiOH, and NiOOH, were used, where the cation was replaced with Zn. Experimental STM images of the films were also compared to DFT-simulated STM images to refine the proposed film structures. In addition, Pd is known to form an alloy with Zn at reducing conditions[32]. In highly oxidizing conditions, however, Pd is known to dissolve oxygen at the surface[33,34,35,36]. Therefore, both PdZn surface alloys and PdO films on Pd were included in the analysis. To minimize strain in ZnO_xH_y overlayers, ZnO_xH_y/Pd(111) interfaces were modeled using a Morié pattern strategy developed in our previous work[37].

Ab-Initio Phase Diagrams

Ab-initio thermodynamic phase diagrams allow the investigation of thermodynamic conditions under which ultrathin metal oxide films may be stabilized. The pressure and temperature dependence of the thermodynamic stability of surfaces can be understood through the formulation developed by Reuter and Scheffler[38], wherein the environment-dependent interfacial energies of many different surface phases are compared to determine which phase is the thermodynamic ground state at given conditions. This formulation assumes that the catalyst surface is in equilibrium with the gas phase and bulk reservoirs within the grand canonical ensemble. Equation 1 defines the free energy of the surface phase with respect to the various bulk reservoirs at conditions given by the gas phase chemical potentials. Normalizing equation 1 by area will give the surface formation energy. In this analysis, ZnO and Pd are identified as the bulk reservoirs, while the potentials of O and H are independent variables and account for the temperature and pressure dependence.

$$\Omega = E^{DFT}_{Zn_aO_bH_c/Pd(111)} - E^{DFT}_{bare\ Pd(111)} - aE^{DFT}_{ZnO\ bulk} - c\mu_H(T,P) - (b-a)\mu_o(T,P) \quad (1)$$

This thermodynamic formalism is descriptive of realistic SMSI systems, wherein a metal nanoparticle is supported on an oxide. In this case, both the support and the nanoparticle are large enough to be considered as thermodynamic reservoirs, as discussed above. However, in the case of natively grown ultrathin oxides, as are observed in the surface science context with films deposited on single crystal metal substrates, an infinite metal oxide (ZnO) reservoir does not exist, and it is therefore difficult to estimate the chemical potential of Zn. Hence, a pseudo canonical ensemble must be used, where Zn is represented by the number of Zn atoms and not the Zn chemical potential. The definition of the free energy $\Lambda(T, A, \mu_O, \mu_H, \mu_{Pd}, N_{Zn})$ is given by equation 2:

$$\Lambda = U - TS - N_O\mu_O - N_H\mu_H - N_{Pd}\mu_{Pd} \quad (1)$$

$$\frac{\Lambda}{A} = \lambda_A = \gamma + \mu_{Zn}\eta_{Zn}\,;\ \eta_{Zn} = \frac{N_{Zn}}{A} \quad (2)$$

where γ is the interfacial tension. The derivation of surface free energy (λ_A) (equation 3), which is plotted against the ratio of Zn per surface area, referenced to a Pd(111) slab, and the details of the hydrogen and oxygen chemical potentials are discussed in the supporting information. The resulting phase diagram is a classic convex hull, where the stable structures have positive second derivatives. The thermodynamically stable phases can thus be identified for the various Zn coverages, and these can be directly compared to experimental surface science measurements, Although the above equation is derived for the $Zn_aO_bH_c$/Pd system, it can easily be generalized to other systems with varying number of gaseous or bulk species, and the current method developed is therefore appropriate for general comparisons of results with experiments where ultrathin films are grown on substrates.

2.4 Reversible structural transformation from ZnO islands to near-surface alloys through a "5Å-ZnO_x" monolayer structure

We begin our study of the ZnO/Pd system by preparing submonolayer ZnO films on Pd(111) under three different gas phase conditions and at two different temperatures. Isolated islands with irregular shapes are formed (STM image in Figure 2.2a) by deposition of diethylzinc at room temperature, annealing in UHV at 423 K, and post-oxidation in 5×10^{-7} mbar of O_2 at

550 K for 10 minutes. The average apparent height of these islands is 3.4±0.2 Å, suggesting that there are two layers of Zn-O. The magnified image of a bilayer island in Figure 2.2b indicates a non-uniformity of the island, where some regions are higher and appear amorphous, while other areas are lower, and an ordered assembly of atoms can be distinguished. Histograms in Figure S1 show that the average heights of the amorphous and ordered regions are 3.9 Å and 2.9 Å, respectively. HREELS detects a ν(O-H) vibration as a sharp loss peak at 3625 cm^{-1} (Figure 2.3, black line), indicative of hydroxyl species, and suggesting that the 1.0 Å height difference can be attributed to hydroxyl species on the surface of ZnO islands. A small full width at half maximum (FWHM) of the ν(O-H) peak (FWHM = 34 cm^{-1}) can be explained by a homogenous chemical environment of the hydroxyl species. It should be noted that hydroxylated zinc oxide films have also been observed on Pt(111) in the absence of hydrogen[39]. There are, in turn, three hydrogen sources which could result in such hydroxyl formation, including residual hydrogen in the UHV chamber, hydrocarbons from diethylzinc decomposition, and dissolved hydrogen stored in the Pd subsurface and bulk[40]. The coverage of Zn is 0.32 monolayer (ML), as calculated from XPS. Taken together, the data support assignment of the structure to partially hydroxylated, two-layer ZnO islands (labeled as BL in the STM images).

Dynamic change of the bilayer ZnO was investigated by three sequential treatments at 550 K in 5×10^{-7} mbar of D_2/O_2 (1:4) mixture, an intermediate between the oxidative and reducing condition. After the first 10-minute treatment, darker, step-like, narrow terraces started to grow out of the bilayer islands, as indicated by the white arrows in Figure 2.2c. The apparent height of this new structure is 1.4±0.1 Å, suggesting a spreading of ZnO from bilayer to monolayer. The magnified image with atomic resolution reveals a 5.0 Å atomic periodicity and a 49.5 Å superlattice on this monolayer structure (Figure 2.2d); the atomic structure of this monolayer film (labelled as "5Å-ZnO_x") will be discussed later. The first appearance of monolayer "5Å-ZnO_x" at the perimeter implies that the transition occurs first at the metal-oxide boundary and gradually propagates into the inner area of ZnO bilayer islands.

Treating the sample for 10 additional minutes under the same conditions led to the conversion of the remaining bilayer islands to the monolayer structure (Figure 2.2e). The direction of Pd monoatomic steps remained unchanged, but the shape was distorted compared to that in Figure 2.2a. Also, the surface coverage of oxide decreased significantly, suggesting

possible Zn dissolution. The final treatment, for 20 additional minutes, led to irregular Pd steps decorated by smaller monolayer ZnO_x islands (Figure 2.2f).

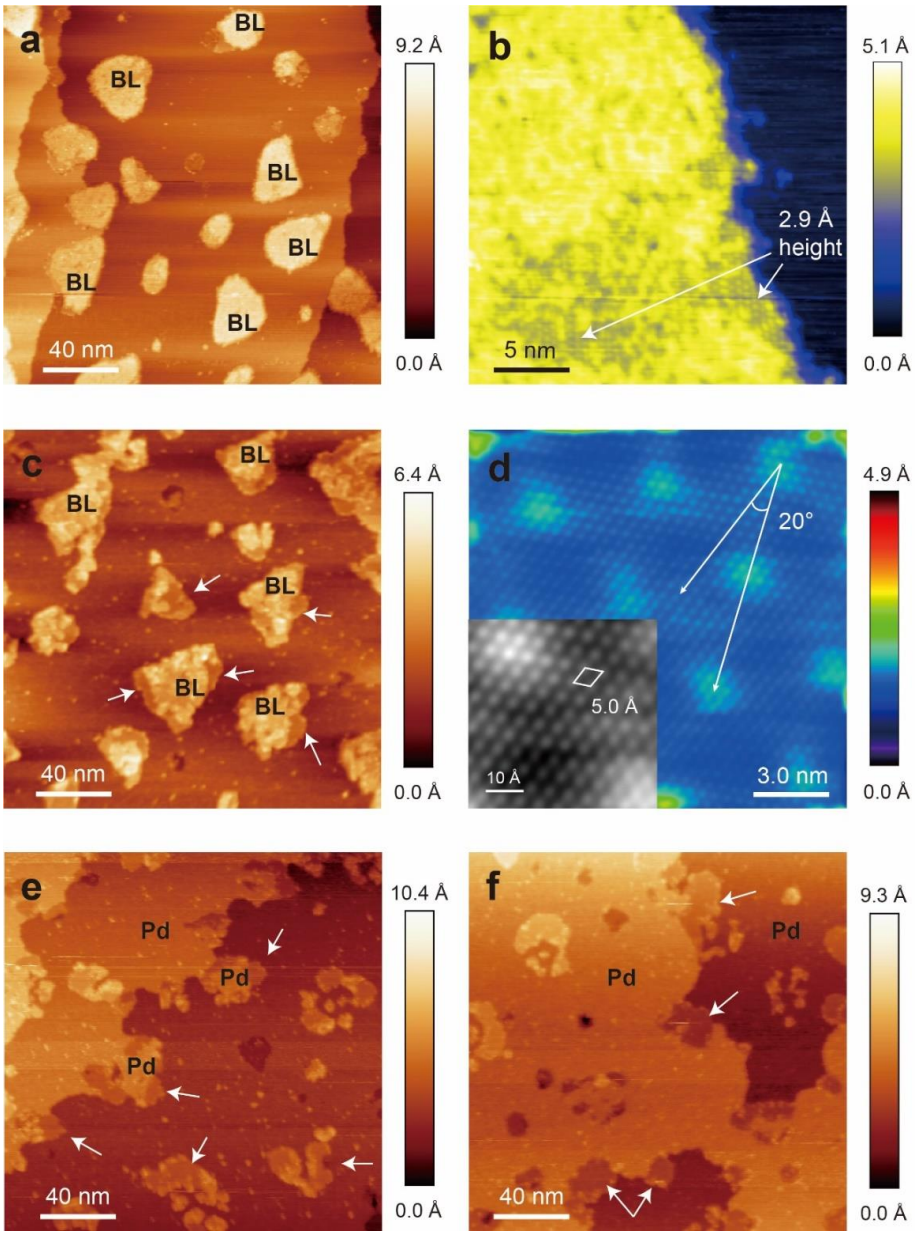

Figure 2.2. STM images of 0.32 ML ZnO_x/Pd(111) with the structural transformation from bilayer ZnO islands to a PdZn alloy through the monolayer "5Å-ZnO_x" structure. (a) Fresh 0.32 ML ZnO_x/Pd(111) surface with dominant bilayer islands (labeled as BL). (b) Magnified image of a bilayer island. The white arrows indicate the atomically resolved regions with 5 Å periodicity and 2.9 Å apparent height. (c) Surface after sequential treatments in a 5×10^{-7} mbar D_2/O_2 (1:4) mixture at 550 K for 10 minutes. (d) Atomic resolution image of the monolayer "5Å-ZnO_x" structure (also denoted as (18×18) R20° based on the superlattice). The two arrows show the rotated 20° angle between the atomic periodicity and superstructure periodicity. The rhombus in the insert indicates the atomic unit cell with a side length of 5.0 Å. (e,f) Surface after second and third treatments in a 5×10^{-7} mbar D_2/O_2 (1:4) mixture at 550 K for 10 and 20 minutes, respectively. The white arrows indicate the monolayer "5Å-ZnO_x" structure.

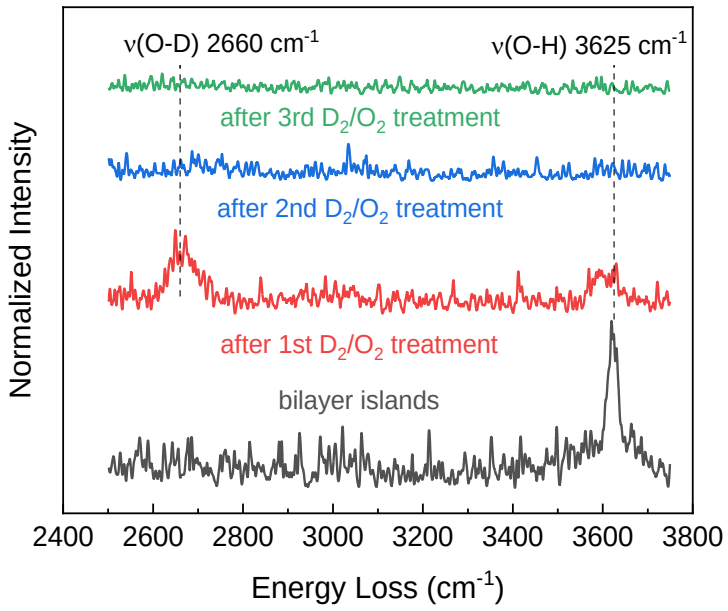

Figure 2.3. HREELS analysis of the as-prepared 0.32 ML ZnO_x/Pd(111) surface with dominant bilayer ZnO islands and the surfaces after three sequential treatments in a D_2/O_2 (1:4) mixture at 550 K for 10, 10, and 20 minutes, respectively. The intensity of the energy loss peaks was normalized to the intensity of the corresponding elastic peaks.

HREELS analysis of the surface after each treatment demonstrated that hydroxyl groups are successively removed from the surface (full-range spectra shown in Figure S2). After the first treatment, HREELS showed a significant ν(O-D) peak at 2660 cm^{-1} in addition to a weakened ν(O-H) peak (Figure 2.3, red line). The centroid of the ν(O-H) peak shifts slightly towards the lower frequencies. The ν(O-D) and ν(O-H) peaks get broader (FWHM = 61 and 51 cm^{-1}, respectively) pointing to an inhomogeneous chemical environment of the hydroxyl species and/or the formation of another hydroxylated zinc oxide phase. As reported, the ultrathin zinc oxide films on Pt(111) also demonstrated the dynamic structural transformations[41]. After the second and third treatments, neither ν(O−D) nor ν(O−H) vibrations (blue line and green lines) were retained on the surface, indicating that the monolayer structure does not contain hydroxyl groups, and OH (OD) vibrations therefore come solely from the bilayer islands. Zn $2p_{3/2}$ XPS spectra were collected to identify the chemical states of Zn during these transformations. As shown in Figure 2.4a (purple line), after diethylzinc deposition and annealing in UHV, diethylzinc was completely decomposed, and Zn formed a near-surface alloy with the Pd substrate, showing a narrow peak at 1020.9 eV with FWHM of 1.2 eV. No carbon signal was detected. Post-oxidation in 5×10^{-7} mbar of O_2 formed bilayer ZnO islands with a broad peak

centered at 1021.5 eV with a FWHM of 2.1 eV, indicating the existence of two or more Zn species in different chemical environments (black line).

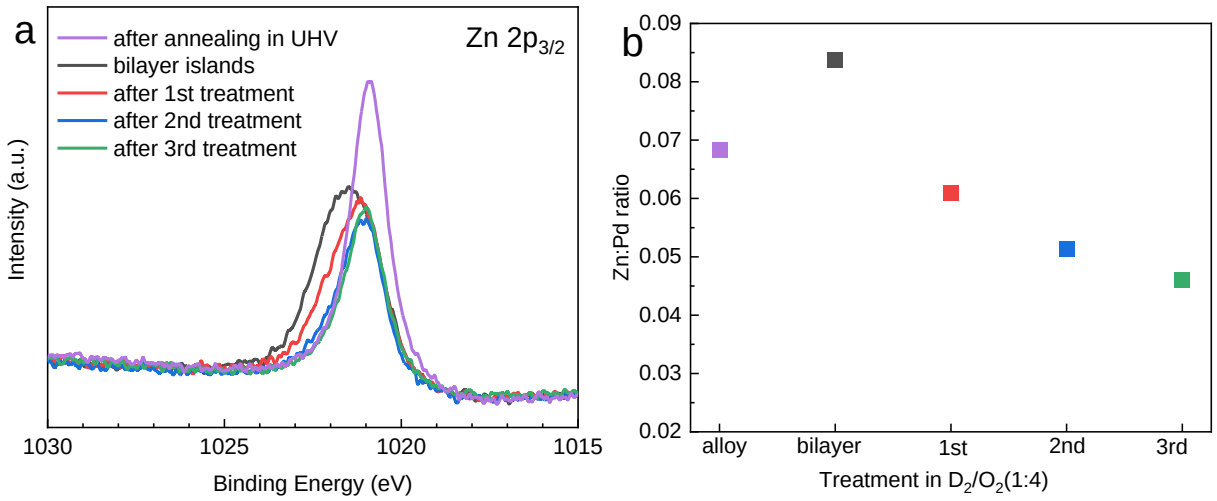

Figure 2.4. XPS analysis of the 0.32 ML ZnO_x/Pd(111) sample. (a) Zn $2p_{3/2}$ XPS peak of the surfaces after diethylzinc deposition and annealing in UHV, after post-oxidation, and after sequential treatments. (b) Zn:Pd atomic ratio of the surfaces calculated from the XPS spectra in (a).

After treating the surface in D_2/O_2, the peak was gradually narrowed and shifted to lower binding energies. After three D_2/O_2 treatments, the Zn $2p_{3/2}$ peak was located at 1021.0 eV with a FWHM of 1.3 eV (green line), which is very similar to the peak shown in purple and therefore corresponds to a PdZn near-surface alloy. Zn LMM auger peaks show corresponding changes, while Pd 3d XPS peaks did not show significant changes due to the large amount of Pd atoms. O 1s signal is overlapped with Pd $3p_{3/2}$ signal and thus cannot be observed in our case (Figure S3).

The atomic ratio of Zn to Pd in the near-surface region was calculated by using the peak areas corrected on Scofield relative sensitivity factors (RSFs) (Figure 2.4b). After the initial diethylzinc deposition and annealing in UHV, the Zn:Pd ratio was 0.060. The ratio increased to 0.084 after post-oxidation to form bilayer ZnO. This change is related to the favorability of Zn dissolution in Pd(111)[42]; once a surface PdZn alloy is formed, some Zn atoms will gradually diffuse into the Pd lattice, and photoelectrons emitted from these Zn moieties will be attenuated when traveling through Pd adlayers, giving a smaller nominal Zn:Pd ratio. Subsequently, during post-oxidation, Zn will be pulled out to form bilayer ZnO islands on the surface, leading to a higher Zn:Pd ratio (similar behavior has been observed for the Pd-Al system[43]). After sequential D_2/O_2 treatments, the Zn:Pd ratio decreased again to 0.061, 0.051, and finally 0.046. Such a

decrease indicates that zinc diffused once again into the subsurface of the Pd crystal during D_2/O_2 treatments.

In aggregate, the above results, including the smaller FWHM, lower binding energy, and smaller Zn:Pd ratio, indicate that Zn was reduced and diffused into the Pd lattice to form near-surface PdZn alloy in the D_2/O_2 (1:4) atmosphere, even in the presence of significant excess O_2. There, bilayer ZnO islands converted to a monolayer "5Å-ZnO_x" structure and then to a near-surface PdZn alloy, where the "5Å-ZnO_x" monolayer structure acts as an intermediate phase and is observed in the short time treatments. It is well known that the PdZn alloys are stable under reducing conditions[44,45], but the above results indicate that even in an O_2 and D_2 (H_2) mixture conditions, local alloy formation and further Zn dissolution are also favorable. The changes imply that alloy formation is the thermodynamic driving force of zinc oxide migration on the palladium surface in this system. It is worth noting that during the treatments in the D_2/O_2 (1:4) mixture, water may inevitably form on the surface. We studied the role of water by introducing D_2O when preparing ZnO films (Figure S8). The formation of the same bilayer islands as that in pure O_2 and the absent of ν(O−D) signal indicate that D_2O was not activated during the preparation, and therefore, the influence of water is negligible.

To study the reversibility of the above structure transitions, we conducted post-oxidation of the near-surface PdZn alloy, as shown in Figure 2.5a and 2.5b. The "5Å-ZnO_x" monolayer structure on Pd(111) with a 0.33 ML coverage was obtained in 5×10^{-7} mbar of a D_2/O_2 (4:7) mixture at 550 K for 10 min. HREELS confirmed that the monolayer structure is free of hydroxyl species (Figure 2.5c, full spectra shown in Figure S4). Subsequent treatment with pure O_2 at 5×10^{-7} mbar at 550 K for 10 min led to formation of the hydroxylated bilayer islands. Therefore, the reversibility of the structure transition was confirmed. In addition, the reversible formation of the alloy phase can also be confirmed from the preparation method itself. That is, after deposition of diethylzinc and annealing in UHV, the collected Zn $2p_{3/2}$ XPS spectra shows that Zn is in metallic state while the O_2 treatment transforms all the alloyed/deposited Zn to bilayer ZnO. This reversible phase transition demonstrates that the zinc oxide/hydroxide film structure on Pd(111) is readily controlled by the gas phase conditions.

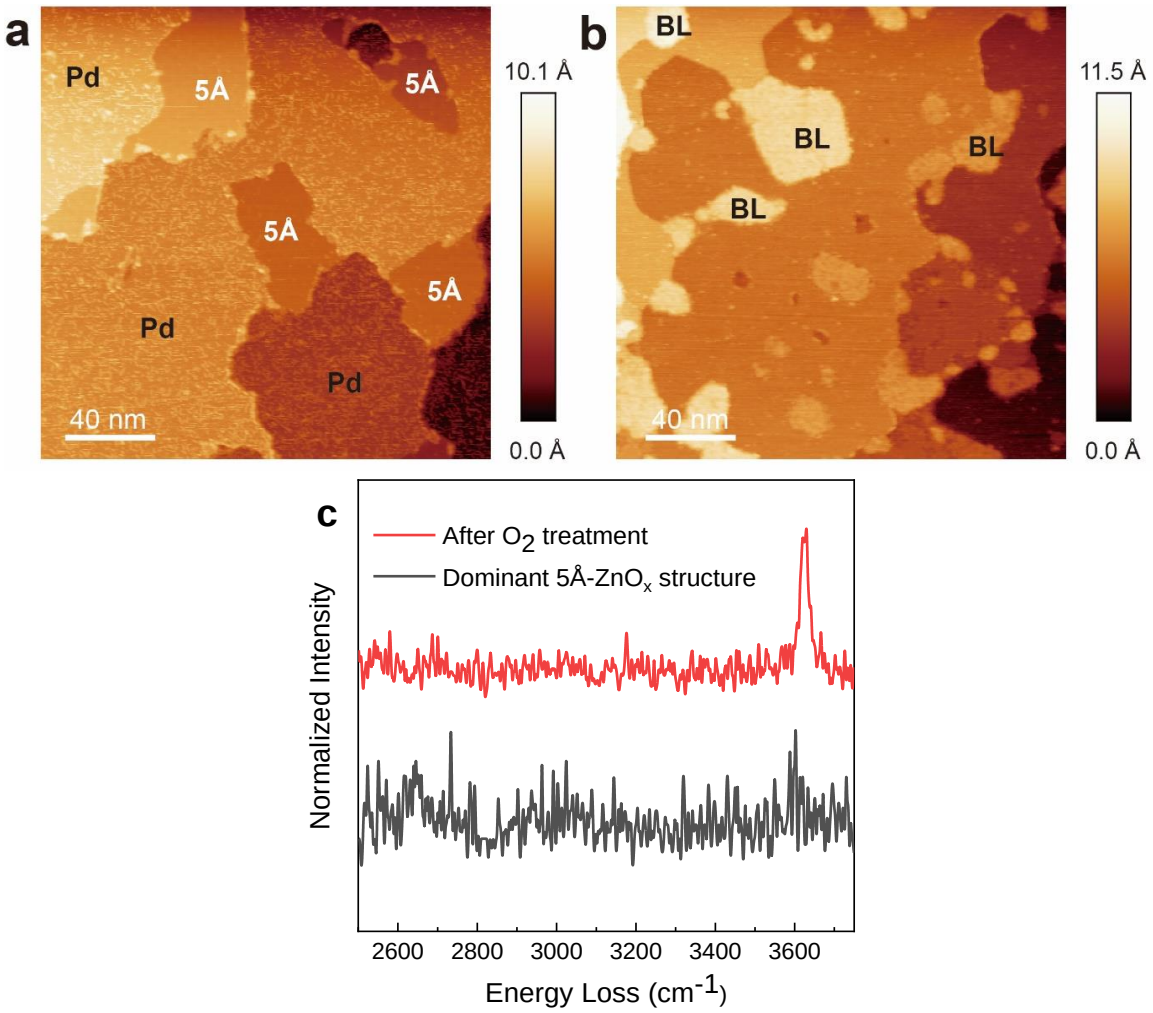

Figure 2.5. STM images and HREEL spectra of the 0.33 ML ZnO_x/Pd (111) sample. The size of the images is 200×200 nm. (a) Fresh surface prepared in a 5×10^{-7} mbar D_2/O_2 (4:7) mixture at 550 K with dominant "5Å-ZnO_x" structure labeled as "5Å" in the image. (b) Surface after treatment in O_2 at 5×10^{-7} mbar at 550 K for 10 min. (c) HREEL spectra as prepared and after treatment in O_2.

To study the influence of the surface coverage on the structure transition, we performed additional experiments by doubling the Zn coverage. Bilayer ZnO islands on Pd(111) with a coverage of 0.68 ML were prepared by oxidative Zn evaporation following post-oxidation in 1×10^{-6} mbar of O_2 at 550 K for 20 minutes (Figure 2.6 a,b). It is worth noting that the formation of bilayer islands is incomplete, and monolayer films were observed between bilayer islands, though atomic resolution was not achieved. Treating the sample in 5×10^{-7} mbar of D_2/O_2 (1:4) mixture at 550 K for 10 minutes resulted in the disappearance of those monolayer films (Figure 2.6 c,d), while another treatment for 20 more minutes led to the appearance of additional monolayer films at the perimeters of bilayer islands (Figure 2.6 e,f). The first D_2/O_2 treatment

indicated that the reduction of the monolayer is faster than the reduction of the bilayer, so the monolayer was cleaned off in the first 10 minutes, while part of the remaining bilayer transformed to a monolayer in the following 20 minutes. A third treatment in 5×10^{-7} mbar of D_2/O_2 (4:7) mixture at 550 K for 10 minutes resulted in complete reduction of zinc oxide and formation of a PdZn near-surface alloy, as indicated by the large Pd patches in STM images (Figure 2.6 g,h). A re-oxidation in 5×10^{-7} mbar of O_2 at 550 K for 5 minutes recovered the bilayer ZnO islands with some small residual Pd patches remaining in close proximity to the newly formed bilayer ZnO (Figure 2.6 i,j). Overall, this reversible transformation between bilayer ZnO and PdZn alloy is similar to the trend observed at low Zn coverages.

2.5 Resolving the "5Å-ZnO_x" monolayer structure

The "5Å-ZnO_x" monolayer film is an important intermediate in the structure transition on Pd(111). Therefore, we employed STM, LEED and DFT modeling to elucidate the atomic-scale details of this structure. Samples with this monolayer phase dominating the surface can be prepared by two approaches: post-oxidation in a D_2/O_2 mixture as described above, or performing the transition from bilayer to alloy at 620 K with a short time to capture the intermediate phase, as shown in Figure S5. The resulting LEED patterns show the superposition of the ZnO_x structure over the Pd(111) substrate. As shown in Figure 2.7, by using the Pd-Pd distance of 2.75 Å as a reference, the periodicity of ZnO_x was calculated to be 5.0 Å, which agrees well with the value measured from STM images. The ZnO reflections are 30° rotated with respect to the Pd(111) reflections, corresponding to a 30° rotation of the ZnO crystallographic structure in respect to the Pd(111) substrate. In addition, the STM image in Figure 2.2d shows a large superlattice on the monolayer island. The periodicity of the superlattice was measured to be 49.5 Å, 18 times that of the Pd−Pd spacing, and is 20° rotated with respect to the 5Å atomic periodicity. Therefore, this "5Å-ZnO_x" structure can also be denoted as (18×18) R20°. To the best of our knowledge, this structure has not been reported in literature.

As discussed above, our results show that the (18×18) R20° structure is an intermediate phase during the transition from bilayer ZnO to PdZn near-surface alloy, since it only forms in D_2/O_2 mixture at elevated temperatures for a limited time, and this structure is resistant to hydroxylation. The distance between bright spots is 5Å, which is not a multiple of the ZnO

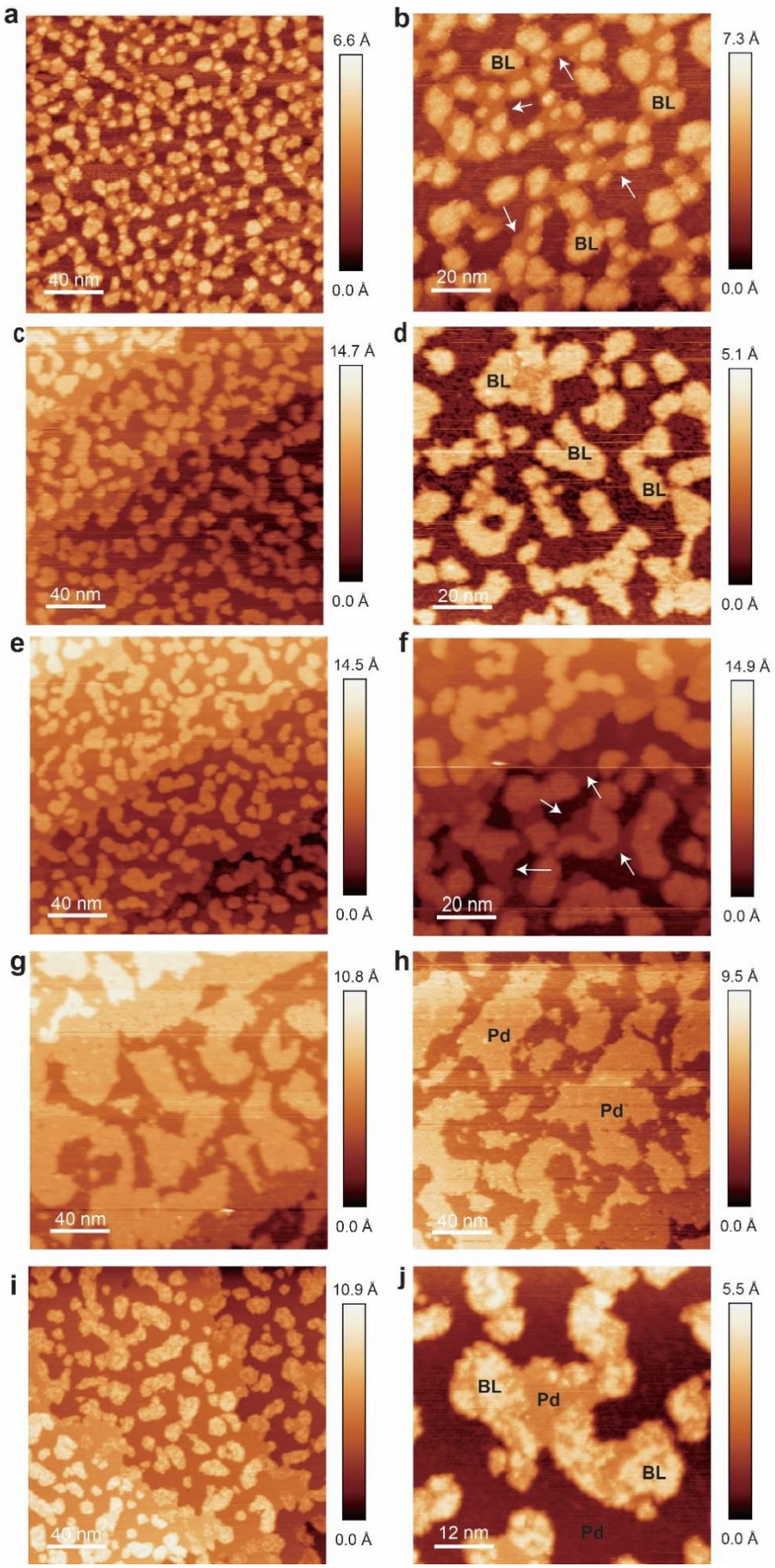

Figure 2.6. STM images of 0.68 ML ZnO_x/Pd(111) with the structural transformation from bilayer islands to PdZn alloy. (a,b) Fresh 0.68 ML ZnO_x/Pd(111) surface prepared by oxidative Zn evaporation and post-oxidation in 1×10^{-6} mbar O_2 at 550 K. (c,d) Surface after first sequential treatment in a 5×10^{-7} mbar D_2/O_2 (1:4) mixture at 550 K for 10 minutes. (e,f) Surface after second treatment in 5×10^{-7} mbar D_2/O_2 (1:4) at 550 K for 20 minutes. (g,h) Surface after third treatment in 5×10^{-7} mbar D_2/O_2 (4:7) at 550 K for 10 minutes. (i,j) Surface after fourth treatment in 5×10^{-7} mbar O_2 at 550 K for 5 minutes. White arrows indicate the monolayer structure.

constant. This result rules out the existence of a pure ZnO phase, as the ZnO lattice constant is close to 3.25Å. There is a 30° rotation between the direction of oxygen alignment and the Pd $<\bar{1}10>$ direction and a 20° rotation between the large superlattice and oxygen alignment, suggesting the superlattice does not originate from the overlap of the upper ZnO_x layer and underlying Pd(111). In fact, in light of the diffusion of zinc atoms into Pd subsurface during the transition, we hypothesize that the (18×18) R20° phase has a PdZn surface alloy as the substrate. The presence of Zn atoms within the vicinity of certain oxygen moieties changes the local density of states (LDOS) which is observed by STM. We used DFT calculations to further elucidate the "5Å-ZnO_x" structure. Using simulated STM, we found a (√3×√3) R30° structure, with oxygen atoms adsorbed onto threefold sites, such that the distance between them is √3 times the Pd-Pd distance, which is close to 5Å (Figure 2.8). The simple model suggests that the local lean surface Zn alloys are the building block for this structure. In the full structure, the Zn atoms will be distributed in the surface and subsurface layers to give the actual STM pattern.

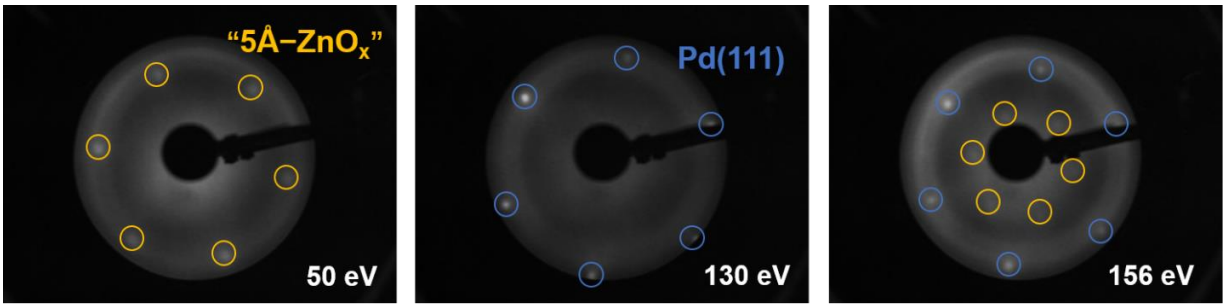

Figure 2.7. LEED patterns of the "5Å-ZnO_x" monolayer structure superimposed on the Pd(111) surface at different electron energies.

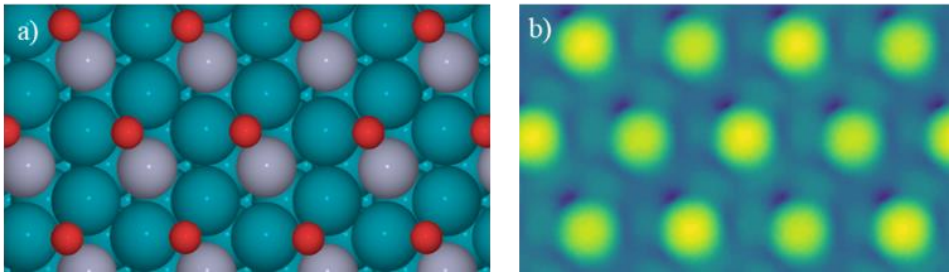

Figure 2.8. (a) DFT simulated image for (√3×√3) R30°, which is a proxy for the (18×18) R20° structure. Blue, red, and purple color are assigned to Pd, O and Zn respectively. (b) Simulated STM image where the dark green spots align with oxygen atoms.

2.6 Theoretical Results

The mixed canonical method was used to plot a surface phase diagram based on the DFT calculations of all relevant surface films, as discussed in Section 2.3 (Figure 2.9). For clarity, only the structures closest to the thermodynamic hull and the structures relevant to the experimental observations are shown in the figure. The chemical potential of oxygen ($\Delta\mu_O$) was fixed at −1.01 eV, which corresponds to 4×10^{-7} mbar O_2 at 550 K, and the chemical potential of hydrogen ($\Delta\mu_H$) was fixed at −0.91 eV, corresponding to 1×10^{-10} mbar H_2; these conditions closely mimic the experimental gas phase conditions. The results demonstrate that hydrogen can adsorb on the ZnO layers[46], and the optimal hydrogen coverage on the topmost ZnO layer is 0.33 ML, or one hydrogen per three surface oxygen atoms (Figure 2.9d). This structure may contribute to the experimentally observed ν(O-H) frequency under these conditions. The other structure on the hull is Pd(111) with adsorbed atomic O (Figure 2.9b). However, monolayer ZnO (Figure 2.9c) and surface alloys (Figure 2.10c) are metastable with respect to the hull, and to reach phase equilibrium, these (or other) phases will always separate to form mixtures of bilayer ZnO and O/Pd(111), with the relative amounts determined by the initial Zn coverage. This is exactly what we see experimentally at these conditions, with the deposited Zn undergoing phase separation to form bilayer ZnO islands and bare Pd.

Introduction of hydrogen causes a shift in the surface phase diagrams. The hydrogen chemical potential ($\Delta\mu_H$) was fixed at −0.75 eV, which corresponds to 1×10^{-7} mbar H_2, and we assume that there is negligible difference between H_2 and D_2 thermodynamics. The dissociation of hydrogen on bare Pd is barrierless, while for oxygen, calculations predict a barrier of 0.64 eV (Figure S14). Therefore, we expect that the surface will be in equilibrium with gas phase hydrogen species but not necessarily with gas phase oxygen. Further, surface hydrogen atoms can rapidly react with surface oxygen and oxygen-containing species to form water (experiments demonstrate the existence of water with a partial pressure on the level of 10^{-9} mbar - Figure S6). The surface oxygen chemical potential will therefore be much lower than the gas phase oxygen chemical potential since oxygen is not replenished as quickly as it is consumed to form water. The water formation equilibrium gives a lower limit for the surface oxygen chemical potential, but since the barrier for water formation on Pd(111) is 0.59 eV, equilibrium will not be achieved, and the actual chemical potential will be higher than this value. As a very simple approximation of this state, we assume the water pressure is within an order of magnitude of the hydrogen

pressure, which has the effect of increasing the oxygen chemical potential to -2.52 eV. Figure 2.10 shows the transformed mixed canonical phase diagram after hydrogen treatment. The extrema are fixed by bare Pd and bilayer ZnO with surface H. The surface alloys drop below the hull and become thermodynamically stable (multiple possible Zn coverages were considered - Figure S9). Further, the subsurface alloys are more stable than the surface alloys. From these observations, we conclude that Zn prefers to dissolve into the Pd lattice rather than segregate to the surface. The Pd lattice effectively acts as a Zn sink and, depending on the kinetics of the diffusion process, lean alloys of Zn will form under these conditions. These predictions are consistent with all available experimental observations.

The combined experimental and computational results present a consistent picture of the evolution of Zn-containing surface phases on Pd substrates under UHV conditions. The ability to elucidate such structures is one of the great strengths of surface science measurements. However, to assess the relevance of such measurements, and the associated structures deduced from computational analysis, for higher pressure conditions relevant to the classic SMSI effect, a modified thermodynamic formalism must be employed to extrapolate to real SMSI conditions. This can be accomplished by modeling the metal nanoparticle and supporting oxide, which may constitute a traditional SMSI system, as infinite reservoirs of Pd metal and ZnO in a grand canonical ensemble (Figure 2.11). Both hydrogen and oxygen chemical potentials are kept open, and the Zn chemical potential is referenced to the bulk ZnO support. As described above, at these conditions, bulk ZnO and O/Pd will be observed if the zinc potential is fixed by bulk ZnO. However, the hydrogen chemical potential is too low to form thermodynamically stabile ZnO_xH_y films in UHV. At realistic SMSI conditions, though, the much higher hydrogen chemical potentials qualitatively change this picture. The green dotted line in Figure 2.11 is plotted at 1 bar H_2 pressure at 550 K. It is seen that, irrespective of the oxygen chemical potential, ZnO_xH_y films will form, although the particular stoichiometry is sensitive to the oxygen chemical potential. It is worth noting that certain surface stoichiometries, such as ZnOH and $Zn_2O_3H_3$, that do not exist in bulk are found to be stable at these conditions. This behavior is traced to both hydrogen incorporation into the films and strong stabilization of the films by the Pd substrates. We note, in passing, that some of the resulting structures could, in fact, have relevance for practical catalysis. For example, ZnOH/Pd (Figure 2.11b) is linear structure and has three phase boundary sites that can be interesting for catalysis. The $Zn_2O_3H_3$ (Figure S10) phase also has

open three phase boundary sites, but closed bilayer structures of $Zn_2O_3H_3$ (Figure 2.11c) are slightly more stable. The $Zn(OH)_2$ (Figure 2.11 d,e) phase is a three-layered continuous structure, such that Zn is sandwiched between two layers of OH with H facing outwards. In the methanol synthesis reaction, the H_2 pressure is generally on the order of 10 bar, and thus DFT calculations predict the formation of these hydroxylated phases. Although experimentally it is difficult to characterize these structures, Xu et al[47] and Kast et al[48] have reported the existence of ZnO_x islands on Pd nanoparticle under reaction conditions.

2.7 Mechanical origin of SMSI behavior of ZnO film on Pd surface

The inverse catalyst model of ZnO_xH_y/Pd(111) considered in this study resembles the oxide overlayer that forms on metal nanoparticle surfaces in SMSI. From the considerations described above, we propose two mechanisms by which SMSI-like effects may occur in the Pd/ZnO system. First, ZnO was observed to be atomically mobile, leading to rearrangement and formation of different phases. However, the newly formed phase grows from the existing phase, which suggests that ZnO species diffuse in two dimensions on the metal surface. As discussed above, our experimental observations indicate that the (18×18) R20° structure forms as an intermediate phase during the transition from bilayer ZnO to a near-surface alloy under D_2/O_2 conditions. Therefore, the oxide is in fact reduced, and zinc atoms subsequently dissolve into the palladium lattice. Zn prefers to form lean alloys with Pd, and so the first layer of ZnO, on top of surface Pd, spreads while breaking into alloys. The second mechanism involves formation of thin ZnO_xH_y films. In this situation, the hydroxylation of the oxide forms a new hydroxyl oxide film on the metal surface with either lower or equal oxidation state to that in ZnO. Under these two circumstances, the SMSI overlayers are different. The former is a ZnO_x overlayer, which eventually transforms into a surface alloy layer, while the latter consists of two dimensional ZnO_xH_y films, which may or may not transform into a surface alloy.

We close by noting that there is an open debate in the literature as to whether the overlayers on SMSI catalysts observed using microscopic and spectroscopic techniques are partially reduced oxides or bimetallic alloys. [48,49,50,51,52] Our results indicate that both scenarios are possible, depending on the gas phase conditions, coverage of oxide on the metal surface, and

reaction quenching to control surface chemical potentials, at least for the transition metals which can form alloys with group VIII noble metals such as Zn.

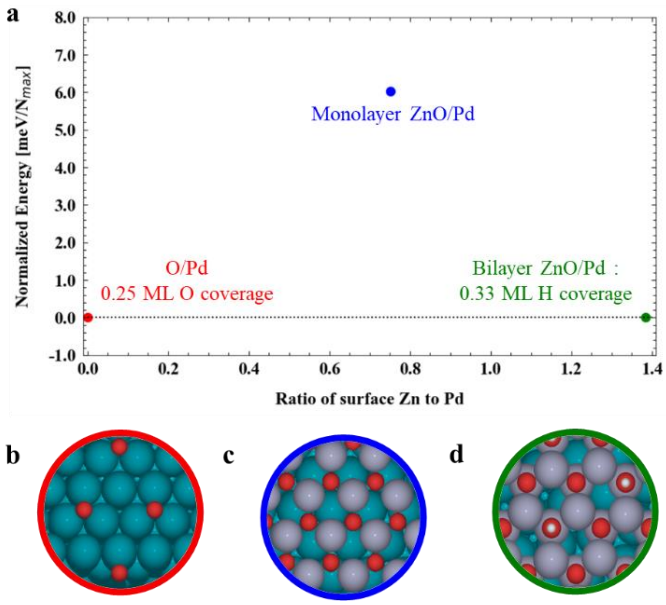

Figure 2.9. (a) Mixed canonical phase diagram plotted at 5×10^{-7}mbar of O_2 pressure. The dotted black line joining O/Pd and bilayer ZnO with 0.33 ML H coverage is the hull line. (b) O/Pd (c) ZnO/Pd (monolayer) (d) $ZnOH_x$/Pd (bilayer).

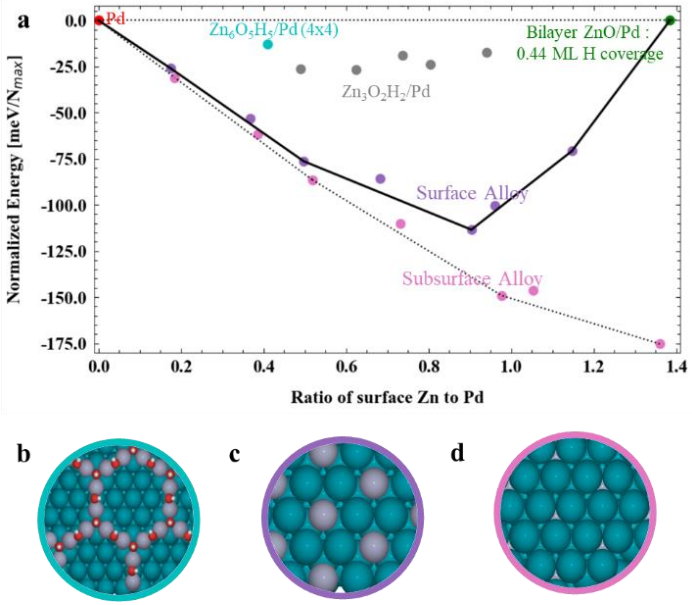

Figure 2.10. (a) Mixed canonical phase diagram plotted at conditions after the hydrogen treatment (10^{-7}mbar of H_2 and 10^{-10} mbar H_2O). The solid black line joining bare Pd – surface alloy – bilayer ZnO is the new hull considering only the surface structures. The dotted line shows the hull with subsurface alloys (b) $Zn_6H_5O_5$ ring structure.[17] (c) Surface PdZn alloy on Pd(111) with 0.33 Zn coverage. (d) Subsurface PdZn alloy on Pd(111) with 0.33 Zn coverage.

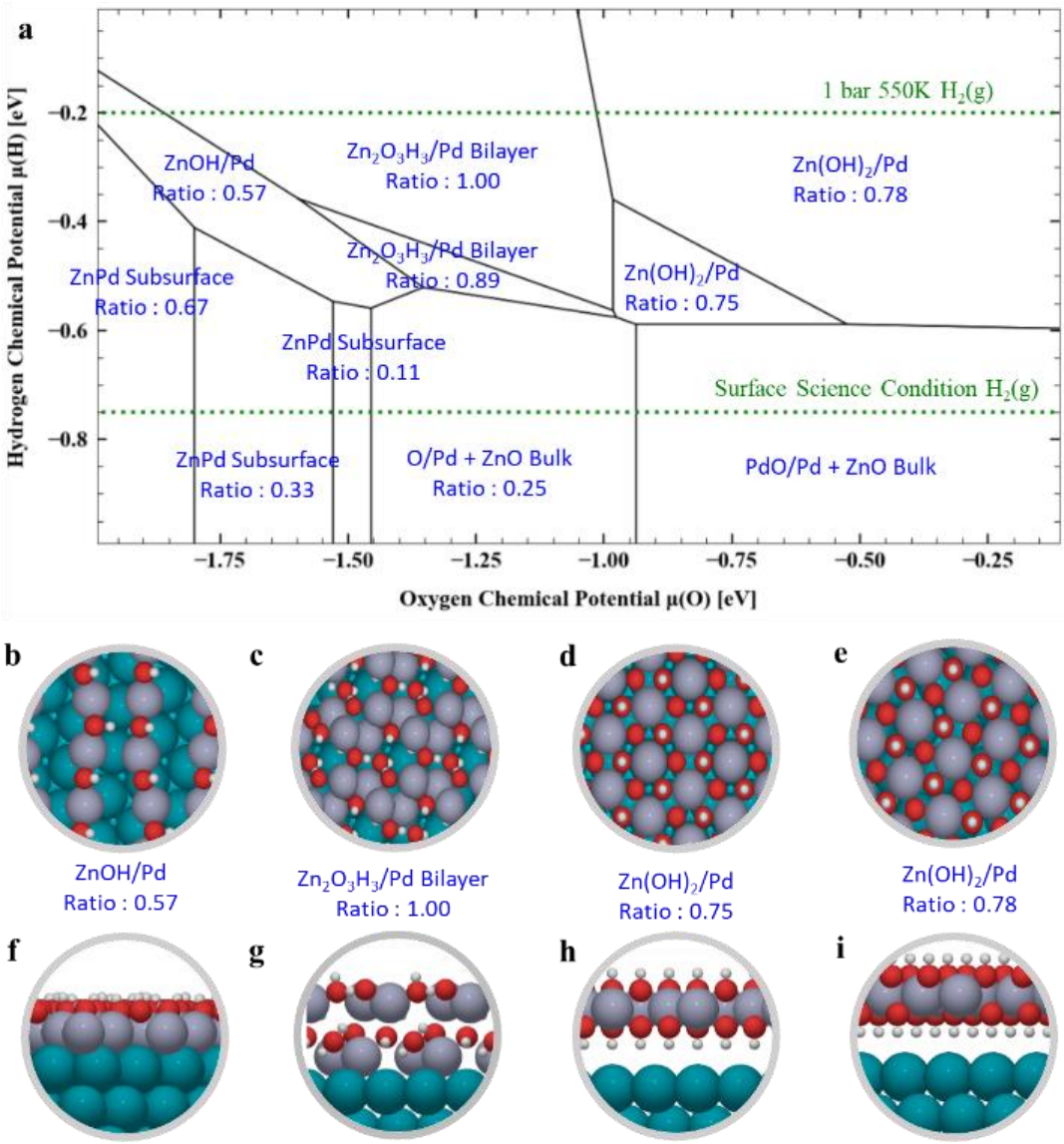

Figure 2.11. (a) Grand canonical phase diagram with reference as H_2(g), O_2(g) and bulk ZnO. The top dotted green line represents the chemical potential of H_2 at 1 bar, 550K and the bottom dotted green line represents the experimental condition i.e., H_2 at 1×10^{-7} mbar, 550K. Top and side view of (b,f) ZnOH/Pd (c,g) $Zn_2O_3H_3$/Pd (d,h) $Zn(OH)_2$/Pd (0.75) and (e,i) $Zn(OH)_2$/Pd (0.78) structures.

2.8 Conclusions

Our experimental and theoretical analyses demonstrate that ZnO can show SMSI-like behavior under weakly reducing surface science conditions (5×10^{-7} mbar of D_2/O_2 (1:4) mixture and 550 K). Aided by the use of DFT calculations and a mixed canonical – grand canonical

phase diagram, the atomic-scale details of these processes are elucidated. Zinc oxide/hydroxide transforms from bilayer islands to a PdZn subsurface alloy through a newly discovered (18×18) R20° intermediate phase, and the transformations are reversible in nature. DFT calculations further reveal that under realistic SMSI conditions, the formation of the other ZnO_xH_y intermediates is favored, which could significantly alter the catalytic behavior of ZnO supported catalysts. The aggregate results suggest that migration and spreading of ZnO on metal surfaces are found to be enabled by two different mechanisms: ZnO_xH_y intermediates formation and surface alloy formation, both of which require the presence of H_2 (D_2).

Although SMSI effects are ultimately system specific, our study serves as a template to help understand the interplay of surface structures and their energetics in a variety of systems. In particular, the two mechanisms for SMSI proposed in this work could, in theory, be applied to the interpretation of a wide variety of SMSI related structure transformations.

2.9 Acknowledgement

The authors gratefully acknowledge the financial support from the National Science Foundation under Award No. 1804712. The use of the Center for Nanoscale Materials (CNM), an Office of Science user facility, was supported by the U.S. Department of Energy, Office of Science, Office of Basic Energy Sciences, under Contract No. DE-AC02-06CH11357. JG and DZ would like to thank Dr. Nathan Guisinger at CNM for the use of STM tip etching tool.

2.10 References

(1) Tauster, S. J.; Fung, S. C.; Garten, R. L. Strong Metal-Support Interactions. Group 8 Noble Metals Supported on TiO_2. *J. Am. Chem. Soc.* **1978**, *100*, 170–175.

(2) Bernal, S.; Botana, F. J.; Calvino, J. J.; López, C.; Pérez-Omil, J. A.; Rodríguez-Izquierdo, J. M. High-Resolution Electron Microscopy Investigation of Metal-Support Interactions in Rh/TiO_2. *J. Chem. Soc. Faraday Trans.* **1996**, *92*, 2799–2809.

(3) Zhang, S.; Plessow, P. N.; Willis, J. J.; Dai, S.; Xu, M.; Graham, G. W.; Cargnello, M.; Abild-Pedersen, F.; Pan, X. Dynamical Observation and Detailed Description of Catalysts under Strong Metal-Support Interaction. *Nano Lett.* **2016**, *16*, 4528–4534.

(4) van Deelen, T. W.; Hernández Mejía, C.; de Jong, K. P. Control of Metal-Support Interactions in Heterogeneous Catalysts to Enhance Activity and Selectivity. *Nat. Catal.* **2019**, *2*, 955–970.

(5) Tauster, S. J. Account of Chemical Research-SMSI. **1987**, *20*, 389–394.

(6) Pesty, F.; Steinrück, H. P.; Madey, T. E. Thermal Stability of Pt Films on TiO_2(110): Evidence for Encapsulation. *Surf. Sci.* **1995**, *339*, 83–95.

(7) Willinger, M. G.; Zhang, W.; Bondarchuk, O.; Shaikhutdinov, S.; Freund, H. J.; Schlögl, R. A Case of Strong Metal-Support Interactions: Combining Advanced Microscopy and Model Systems to Elucidate the Atomic Structure of Interfaces. *Angew. Chemie Int. Ed.* **2014**, *53*, 5998–6001.

(8) Suzuki, T.; Souda, R. The Encapsulation of Pd by the Supporting TiO_2(110) Surface Induced by Strong Metal-Support Interactions. *Surf. Sci.* **2000**, *448*, 33–39.

(9) Matsubu, J. C.; Zhang, S.; DeRita, L.; Marinkovic, N. S.; Chen, J. G.; Graham, G. W.; Pan, X.; Christopher, P. Adsorbate-Mediated Strong Metal-Support Interactions in Oxide-Supported Rh Catalysts. *Nat. Chem.* **2017**, *9*, 120–127.

(10) Baker, R. T. K.; Tauster, S. J.; Dumesic, J. A. Strong Metal-Support Interactions. *ACS Symp. Ser.* **1986**.

(11) Grunwaldt, J. D.; Molenbroek, A. M.; Topsøe, N. Y.; Topsøe, H.; Clausen, B. S. In Situ Investigations of Structural Changes in Cu/ZnO Catalysts. *J. Catal.* **2000**, *194*, 452–460.

(12) Naumann D'Alnoncourt, R.; Xia, X.; Strunk, J.; Löffler, E.; Hinrichsen, O.; Muhler, M. The Influence of Strongly Reducing Conditions on Strong Metal-Support Interactions in Cu/ZnO Catalysts Used for Methanol Synthesis. *Phys. Chem. Chem. Phys.* **2006**, *8*, 1525–1538.

(13) Behrens, M.; Studt, F.; Kasatkin, I.; Kühl, S.; Hävecker, M.; Abild-pedersen, F.; Zander, S.; Girgsdies, F.; Kurr, P.; Kniep, B.; Tovar, M.; Fischer, R. W.; Nørskov, J. K.; Schlögl, R. The Active Site of Methanol Synthesis over $Cu/ZnO/Al_2O_3$ Industrial Catalysts. *Science.* **2012**, *336*, 893–897.

(14) Lunkenbein, T.; Schumann, J.; Behrens, M.; Schlögl, R.; Willinger, M. G. Formation of a ZnO Overlayer in Industrial Cu/ZnO/Al_2O_3 Catalysts Induced by Strong Metal-Support Interactions. *Angew. Chemie Int. Ed.* **2015**, *54*, 4544–4548.

(15) Claeyssens, F.; Freeman, C. L.; Allan, N. L.; Sun, Y.; Ashfold, M. N. R.; Harding, J. H. Growth of ZnO Thin Films - Experiment and Theory. *J. Mater. Chem.* **2005**, *15*, 139–148.

(16) Pan, Q.; Liu, B. H.; McBriarty, M. E.; Martynova, Y.; Groot, I. M. N.; Wang, S.; Bedzyk, M. J.; Shaikhutdinov, S.; Freund, H. J. Reactivity of Ultra-Thin ZnO Films Supported by Ag(111) and Cu(111): A Comparison to ZnO/Pt(111). *Catal. Letters* **2014**, *144*, 648–655.

(17) Weirum, G.; Barcaro, G.; Fortunelli, A.; Weber, F.; Schennach, R.; Surnev, S.; Netzer, F. P. Growth and Surface Structure of Zinc Oxide Layers on a Pd(111) Surface. *J. Phys. Chem. C* **2010**, *114*, 15432–15439.

(18) Schott, V.; Oberhofer, H.; Birkner, A.; Xu, M.; Wang, Y.; Muhler, M.; Reuter, K.; Wöll, C. Chemical Activity of Thin Oxide Layers: Strong Interactions with the Support Yield a New Thin-Film Phase of ZnO. *Angew. Chemie Int. Ed.* **2013**, *52*, 11925–11929.

(19) Kim, C. H.; Lee, J. S.; Trimm, D. L. The Preparation and Characterisation of Pd-ZnO Catalysts for Methanol Synthesis. *Top. Catal.* **2003**, *22*, 319–324.

(20) Iwasa, N.; Masuda, S.; Takezawa, N. Steam Reforming of Methanol over Ni, Co, Pd and Pt Supported on ZnO. *React. Kinet. Catal. Lett.* **1995**, *55*, 349–353.

(21) Chin, Y. H.; Dagle, R.; Hu, J.; Dohnalkova, A. C.; Wang, Y. Steam Reforming of Methanol over Highly Active Pd/ZnO Catalyst. *Catal. Today* **2002**, *77*, 79–88.

(22) Fadley, C. S. Basic Concepts of X-Ray Photoelectron Spectroscopy. *Electron Spectrosc. theory, Tech. Appl.* **1978**, *2*, 1–156.

(23) Paul, R.; Reifenberger, R. G.; Fisher, T. S.; Zemlyanov, D. Y. Atomic Layer Deposition of FeO on Pt(111) by Ferrocene Adsorption and Oxidation. *Chem. Mater.* **2015**, *27*, 5915–5924.

(24) Gharachorlou, A.; Detwiler, M. D.; Nartova, A. V.; Lei, Y.; Lu, J.; Elam, J. W.; Delgass, W. N.; Ribeiro, F. H.; Zemlyanov, D. Y. Palladium Nanoparticle Formation on TiO_2(110) by Thermal Decomposition of Palladium(II) Hexafluoroacetylacetonate. *ACS Appl. Mater. Interfaces* **2014**, *6*, 14702–14711.

(25) Horcas, I.; Fernández, R.; Gómez-Rodríguez, J. M.; Colchero, J.; Gómez-Herrero, J.; Baro, A. M. WSXM: A Software for Scanning Probe Microscopy and a Tool for Nanotechnology. *Rev. Sci. Instrum.* **2007**, *78*, 013705–013712.

(26) Kresse, G.; Furthmüller, J. Efficient Iterative Schemes for Ab Initio Total-Energy Calculations Using a Plane-Wave Basis Set. *Phys. Rev. B* **1996**, *54*, 11169–11186.

(27) Kresse, G.; Furthmüller, J. Efficiency of Ab-Initio Total Energy Calculations for Metals and Semiconductors Using a Plane-Wave Basis Set. *Comput. Mater. Sci.* **1996**, *6*, 15–50.

(28) Kresse, G.; Joubert, D. From Ultrasoft Pseudopotentials to the Projector Augmented-Wave Method. *Phys. Rev. B* **1999**, *59*, 1758–1775.

(29) Perdew, J. P.; Burke, K.; Ernzerhof, M. Generalized Gradient Approximation Made Simple. *Phys. Rev. Lett.* **1996**, *77*, 3865–3868.

(30) Hjorth Larsen, A.; JØrgen Mortensen, J.; Blomqvist, J.; Castelli, I. E.; Christensen, R.; Dułak, M.; Friis, J.; Groves, M. N.; Hammer, B.; Hargus, C.; Hermes, E. D.; Jennings, P. C.; Bjerre Jensen, P.; Kermode, J.; Kitchin, J. R.; Leonhard Kolsbjerg, E.; Kubal, J.; Kaasbjerg, K.; Lysgaard, S.; Bergmann Maronsson, J.; Maxson, T.; Olsen, T.; Pastewka, L.; Peterson, A.; Rostgaard, C.; SchiØtz, J.; Schütt, O.; Strange, M.; Thygesen, K. S.; Vegge, T.; Vilhelmsen, L.; Walter, M.; Zeng, Z.; Jacobsen, K. W. The Atomic Simulation Environment - A Python Library for Working with Atoms. *J. Phys. Condens. Matter* **2017**, *29*, 273002–273031.

(31) Mortensen, J. J.; Hansen, L. B.; Jacobsen, K. W. Real-Space Grid Implementation of the Projector Augmented Wave Method. *Phys. Rev. B* **2005**, *71*, 035109–035119.

(32) Armbrüster, M.; Behrens, M.; Föttinger, K.; Friedrich, M.; Gaudry, E.; Matam, S. K.; Sharma, H. R. The Intermetallic Compound ZnPd and Its Role in Methanol Steam Reforming. *Catal. Rev. Sci. Eng.* **2013**, *55*, 289–367.

(33) Todorova, M.; Reuter, K.; Scheffler, M. Density-Functional Theory Study of the Initial Oxygen Incorporation in Pd(111). *Phys. Rev. B - Condens. Matter Mater. Phys.* **2005**, *71*, 1–8.

(34) Gabasch, H.; Unterberger, W.; Hayek, K.; Klötzer, B.; Kleimenov, E.; Teschner, D.; Zafeiratos, S.; Hävecker, M.; Knop-Gericke, A.; Schlögl, R.; Han, J.; Ribeiro, F. H.; Aszalos-Kiss, B.; Curtin, T.; Zemlyanov, D. In Situ XPS Study of Pd(111) Oxidation at Elevated Pressure, Part 2: Palladium Oxidation in the 10-1 Mbar Range. *Surf. Sci.* **2006**, *600*, 2980–2989.

(35) Han, J.; Zemlyanov, D. Y.; Ribeiro, F. H. Catalytic Combustion of Methane on Palladium Single Crystals. *Catal. Today* **2006**, *117*, 506–513.

(36) Zemlyanov, D.; Aszalos-Kiss, B.; Kleimenov, E.; Teschner, D.; Zafeiratos, S.; Hävecker, M.; Knop-Gericke, A.; Schlögl, R.; Gabasch, H.; Unterberger, W.; Hayek, K.; Klötzer, B. In Situ XPS Study of Pd(1 1 1) Oxidation. Part 1: 2D Oxide Formation in 10^{-3} Mbar O_2. *Surf. Sci.* **2006**, *600*, 983–994.

(37) Zeng, Z.; Chang, K. C.; Kubal, J.; Markovic, N. M.; Greeley, J. Stabilization of Ultrathin (Hydroxy)Oxide Films on Transition Metal Substrates for Electrochemical Energy Conversion. *Nat. Energy* **2017**, *2*, 1–9.

(38) Reuter, K.; Scheffler, M. First-Principles Atomistic Thermodynamics for Oxidation Catalysis: Surface Phase Diagrams and Catalytically Interesting Regions. *Phys. Rev. Lett.* **2003**, *90*, 046103–046106.

(39) Liu, B. H.; Boscoboinik, J. A.; Cui, Y.; Shaikhutdinov, S.; Freund, H. J. Stabilization of Ultrathin Zinc Oxide Films on Metals: Reconstruction versus Hydroxylation. *J. Phys. Chem. C* **2015**, *119*, 7842–7847.

(40) Engel, T.; Kuipers, H. A Molecular-Beam Investigation of the Scattering, Adsorption and Absorption of H_2 and D_2 from/on/in Pd(111). *Surf. Sci.* **1979**, *90*, 162–180.

(41) Liu, B. H.; McBriarty, M. E.; Bedzyk, M. J.; Shaikhutdinov, S.; Freund, H. J. Structural Transformations of Zinc Oxide Layers on Pt(111). *J. Phys. Chem. C* **2014**, *118*, 28725–28729.

(42) Stadlmayr, W.; Rameshan, C.; Weilach, C.; Lorenz, H.; Hävecker, M.; Blume, R.; Rocha, T.; Teschner, D.; Knop-Gericke, A.; Zemlyanov, D.; Penner, S.; Schlögl, R.; Rupprechter, G.; Klötzer, B.; Memmel, N. Temperature-Induced Modifications of PdZn Layers on Pd(111). *J. Phys. Chem. C* **2010**, *114*, 10850–10856.

(43) Gharachorlou, A.; Detwiler, M. D.; Mayr, L.; Gu, X. K.; Greeley, J.; Reifenberger, R. G.; Delgass, W. N.; Ribeiro, F. H.; Zemlyanov, D. Y. Surface Chemistry of Trimethylaluminum on Pd(111) and Pt(111). *J. Phys. Chem. C* **2015**, *119*, 19059–19072.

(44) Chen, Z. X.; Neyman, K. M.; Gordienko, A. B.; Rösch, N. Surface Structure and Stability of PdZn and PtZn Alloys: Density-Functional Slab Model Studies. *Phys. Rev. B - Condens. Matter Mater. Phys.* **2003**, *68*, 1–8.

(45) Bayer, A.; Flechtner, K.; Denecke, R.; Steinrück, H. P.; Neyman, K. M.; Rösch, N. Electronic Properties of Thin Zn Layers on Pd(111) during Growth and Alloying. *Surf. Sci.* **2006**, *600*, 78–94.

(46) Thang, H. V.; Pacchioni, G. H2 Adsorption on Wurtzite ZnO and on ZnO/M(111) (M=Cu, Ag and Au) Bilayer Films. *ChemNanoMat* **2019**, *5*, 932–939.

(47) Xu, J.; Su, X.; Liu, X.; Pan, X.; Pei, G.; Huang, Y.; Wang, X.; Zhang, T.; Geng, H. Methanol Synthesis from CO_2 and H_2 over Pd/ZnO/Al_2O_3: Catalyst Structure Dependence of Methanol Selectivity. *Appl. Catal. A Gen.* **2016**, *514*, 51–59.

(48) Kast, P.; Friedrich, M.; Girgsdies, F.; Kröhnert, J.; Teschner, D.; Lunkenbein, T.; Behrens, M.; Schlögl, R. Strong Metal-Support Interaction and Alloying in Pd/ZnO Catalysts for CO Oxidation. *Catal. Today* **2016**, *260*, 21–31.

(49) Resasco, D. E.; Weber, R. S.; Sakellson, S.; McMillan, M.; Haller, G. L. X-Ray Absorption near-Edge Structure Evidence for Direct Metal-Metal Bonding and Electron Transfer in Reduced Rh/TiO_2 Catalysts. *J. Phys. Chem.* **1988**, *92*, 189–193.

(50) Boccuzzi, F.; Chiorino, A.; Ghiotti, G. IR Study of the CO Adsorption on Pt/ZnO Samples: Evidence for a PtZn Phase Formation in the SMSI State. *Surf. Sci.* **1989**, *209*, 77–88.

(51) Zhu Chen, J.; Gao, J.; Probus, P. R.; Liu, W.; Wu, X.; Wegener, E. C.; Kropf, A. J.; Zemlyanov, D.; Zhang, G.; Yang, X.; Miller, J. T. The Effect of Strong Metal-Support Interaction (SMSI) on Pt-Ti/SiO_2 and Pt-Nb/SiO_2 catalysts for Propane Dehydrogenation. *Catal. Sci. Technol.* **2020**, *10*, 5973–5982.

(52) Beck, A.; Huang, X.; Artiglia, L.; Zabilskiy, M.; Wang, X.; Rzepka, P.; Palagin, D.; Willinger, M. G.; van Bokhoven, J. A. The Dynamics of Overlayer Formation on Catalyst Nanoparticles and Strong Metal-Support Interaction. *Nat. Commun.* **2020**, *11*, 1–8.

3. TUNING ADSORPTION PROPERTIES OF PT(111) THROUGH STRONG METAL-HYDROXIDE INTERACTION

3.1 Abstract

Metal nanoparticles supported over zinc oxide catalyze industrially important reactions like methanol synthesis and methanol steam reforming. The synergistic effect between the zinc oxide support and metals is linked to the formation of ultrathin zinc oxide/hydroxide films on metal surfaces through strong metal-support interaction. For non-reducible oxides including zinc oxide, hydroxylation serves as an essential way to form partially reduced oxide overlayers. However, the nature of metal-oxide interaction and metal-hydroxide interaction are not well understood and distinguished at an atomic level. Herein, we study the ZnO/Pt(111) and $Zn_6O_5H_5$/Pt(111) model catalysts using surface analytical techniques and density functional theory calculations. We found that the graphite-like ZnO interacts weakly with Pt surface and barely affects the surface electronic properties. Whereas the honeycomb-like $Zn_6O_5H_5$ can contribute negative charge to the Pt atoms confined in the rings and tune CO adsorption behavior drastically with little sacrifice of the total number of active sites. Ethylene adsorption and DFT calculations indicated that ethylidyne formation on Pt was weakened once covered by the $Zn_6O_5H_5$ structure, suggesting better resistivity towards deeper hydrogenation of ethylene and coking formation. Therefore, the formation of ordered zinc hydroxide phase can serve as an effective way to tune the chemistry of metal surfaces.

3.2 Introduction

Zinc oxide (ZnO) plays an important role in catalyzing industrial reactions such as water-gas shift reaction[1], methanol synthesis[2], and methanol reforming[3,4]. The active sites of metal/ZnO-based catalysts have been extensively used, and the synergistic effect between ZnO and metals (Pt[5], Pd[6,7], or Cu[1-4]), was demonstrated to be crucial for catalytic performance[8]. Depending on the metal and reaction conditions, both bimetallic alloy formation[7,9] and oxide overlayer formation[10,11,12] are proposed in literature. The latter scenario is a typical example of strong metal-support interaction (SMSI), where oxide support migrates and encapsulates the

metal nanoparticles[13]. Different from the Zn^{2+} in bulk zinc oxide, the ZnO SMSI layer exhibited a partially reduced $Zn^{\delta+}$ ($\delta<2$) oxidation state as determined by electron energy loss spectroscopy (EELS)[12], which is a feature of SMSI phenomenon. The unsaturated oxidation state for Zn can be evolved from surface hydroxylation[14,15], as evidenced by the studies of zinc oxide thin films on metal substrates[16,17] as well as Cu/ZnO-based catalysts[18]. However, it remains difficult to determine the stoichiometry of hydroxylated zinc oxide in technical and industrial catalysts, and the potential metal-hydroxide interactions are largely unexplored compared to traditional metal-oxide interactions.

The surface science experiments over inverse model catalysts, which are ultrathin oxide films on metal single crystal surfaces, enabled fundamental studies about the structure and properties of metal-support interfaces at an atomic level. Thin film zinc oxide has been found to form graphite-like structure[19,20] over multiple metal substrates, such as Ag[20], Au[21], Cu[22], Pt[16], and Pd[17] (111) surfaces. These ZnO films show certain unique properties depending on the underlying metal. For example, ZnO/Ag(111) is immune to hydroxylation upon D_2O dosing[23,24], while ZnO films on Pt(111) and Pd(111) are extremely susceptible to hydroxylation with little amount of residual hydrogen[16,17]. Interestingly, these inverse catalyst models show enhanced activity for C1 chemistries like CO oxidation reaction[25]. Martynova *et al.* reported that CO oxidation rates were much higher on ZnO/Pt(111) than on bare Pt(111) or ZnO(0001)[26]. In a recent study, Liu *et al.* proposed that the reaction goes through a "CO + OH" associative step, which takes place at the hydroxylated ZnO/Pt(111) boundary sites[27]. A comparative study showed that the enhancement in CO oxidation rates is not observed over ZnO/Ag(111) and ZnO/Cu(111)[22]. In conclusion, Pt(111) is unique in its ability to form stable hydroxylated zinc oxide films and is further manifested in CO oxidation rates.

Although it has been demonstrated that hydroxylation is crucial for the stability of zinc oxide films and the enhancement of catalytic performance, the studies mainly focused on the graphite-like structure, which may not be the most stable structure on Pt(111) surface under certain conditions. Liu et al.[16] and Su et al.[28] observed that the graphite-like ZnO transformed to honeycomb-like $Zn_6O_5H_5$ structure on Pt(111) surface due to the background or external hydrogen. This $Zn_6O_5H_5$ phase merits attention for several reasons. First, the honeycomb-like structure is an open structure with interior Pt atoms open for reactions and is hypothesized to exhibit distinct properties. Second, this network structure can maximize the percentage of

hydroxide-metal boundaries compared to surface decoration by compact ZnO islands, offering a perfect model to study the properties of metal-hydroxide interfaces. Third, since this structure is formed in the presence of hydrogen, it might be more stable than ZnO under reducing reaction conditions.

In this work, we investigated and compared two types of ultrathin films, the compact graphite-like ZnO and the open honeycomb-like $Zn_6O_5H_5$ on Pt(111) by scanning tunneling microscopy (STM), X-ray photoelectron spectroscopy (XPS), high-resolution energy loss spectroscopy (HREELS) and density functional theory (DFT) calculations. By vibrational studies with CO as a probe molecule, we found that the graphite-like ZnO islands barely affect the electronic properties of Pt surface, while the honeycomb-like $Zn_6O_5H_5$ network tunes the surface electron density of Pt significantly, as evidenced by the switch from on-top to bridging adsorption sites in accompany with a 50 cm^{-1} shift of ν(CO) towards lower frequencies. DFT calculations revealed that Zn atoms in $Zn_6O_5H_5$ contribute negative charge to the adjacent Pt atoms. Ethene adsorption indicated that the formation of ethylidyne species on Pt at room temperature is inhibited. In summary, this study of ZnO_xH_y/Pt(111) model catalysts distinguish a unique metal-hydroxide interaction from metal-oxide interactions, demonstrating a promising application for the zinc hydroxide phase as a uniform and controllable approach to modifying the surface chemistry of metal catalysts.

3.3 Experimental and computational methods

3.3.1 Experimental methods

Experiments were carried out in an Omicron surface analysis cluster consisting of two ultra-high vacuum (UHV) chambers. The preparation chamber (base pressure is ~6×10^{-10} mbar) is equipped with gas manifolds, a Zn evaporator for physical vapor deposition (PVD), and a mass spectrometer (MS). The analysis chamber (base pressure is ~6×10^{-11} mbar) is equipped with room temperature Omicron scanning tunneling microscopy (STM), X-ray photoelectron spectroscopy (XPS), high-resolution electron energy loss spectroscopy (HREELS), and low energy electron diffraction (LEED).

The Pt(111) single crystal was cleaned by cycles of Ar^+ sputtering, annealing in 1×10^{-6} mbar of O_2, and annealing in UHV up to 973 K. The cleanliness of the Pd(111) surface was monitored by XPS. ZnO films on Pt(111) were prepared by oxidative deposition of metallic Zn in 1×10^{-7} mbar O_2 at room temperature, followed by post-oxidation in 5×10^{-7} mbar O_2 at 550 K for 10 minutes. For hydrogen exposure, ex situ treatment was done by introducing D_2 into preparation chamber, and in situ STM measurement was done by introducing D_2 into the analysis chamber. D_2 was used instead of H_2 throughout our experiments to distinguish the external (intentional exposure) and internal (residual gas) sources of hydrogen by MS and HREELS. The coverage of Zn on Pt was controlled by metallic Zn exposure parameters (current of the power supply and exposure time) and was calculated using the area of Zn $2p_{3/2}$ and Pt 4f XPS peaks under the assumption of a non-attenuating ZnO adlayer.[29] Therefore, one monolayer (ML) is defined as equivalent number of Zn atoms to the number of Pt atoms in a Pt monolayer throughout the paper. This approach has been well validated and is described in detail elsewhere.[30,31]

After zinc oxide film preparation, the sample stage was cooled fast, and the sample was then transferred within 1-2 minutes to the analysis chamber for characterization by HREELS, STM, LEED and XPS. HREELS measurements were performed using an ELS 5000 (LK Technologies). The scattered electrons were collected with a 60° incidence angle and a 50° reflection angle with primary electron beam energy of 7 eV. The FWHM of the elastic peak of samples was between 2.5~5.0 meV (equivalent to 20~40 cm^{-1}). The intensity of energy loss was normalized to the intensity of the elastic peak. The raw data was fitted by using the line shape of the elastic peak and a linear background. CO and C_2H_4 exposures were done in analysis chamber. CO exposure was done after the sample was moved to HREELS position, while for *in situ* C_2H_4 adsorption measurements, the analysis chamber was filled with C_2H_4 prior to sample transfer to avoid residual CO adsorption. NO exposures was done in preparation chamber.

XPS data were collected using a non-monochromatic Mg Kα x-ray source at an incidence angle of 45°. The emitted photoelectrons were collected using Omicron EAC 125 analyzer and Omicron EAC 2000 analyzer controller at a photoelectron emission angle of 45° with respect to the surface normal. XPS data were analyzed using CasaXPS software. Since the sample is conductive and grounded, no charge correction was necessary. The Pt $4f_{7/2}$ peak for the clean Pt(111) surface was observed at 71.0 eV. During characterization, residual CO in the UHV

chamber can be adsorbed on the surface and thus contribute to the O 1s XPS peak. Therefore, when fitting the curve, four components were introduced and allowed for relaxation, including two ZnO species, linear CO, and bridging CO. It turned out that the CO components were eliminated to give a good fitting, which is reasonable since the coverage of CO on the surface is low.

STM imaging was performed at a constant current mode at room temperature with tungsten tips, which were prepared by electrochemical etching of 0.25 mm (or 0.175 mm) tungsten wires and cleaned by electron bombardment in UHV. The bias voltage varied from +0.8 to +1.5 V with tunneling current ranging from 0.4 to 0.8 nA. STM images were analyzed using WSxM software.[32]

3.3.2 Computational methods

Periodic Density Functional Theory (DFT) calculations were performed using Vienna *Ab Initio* Simulation Package (VASP)[33,34]. Projected Augmented Wave (PAW) potentials[35] were used to model the core electrons. The generalized gradient approximation (GGA) exchange-correlation functional, developed by Perdew-Burke-Ernzerhof (PBE) was used[36]. The energy cutoff for the planewave basis set was 500 eV. Monkhorst-Pack was used to sample the Brillouin zone. Since, a huge number of unique unit cells were used, we made sure that the lattice constant times the number of K points was close to 30 Å. The (111) surface slab for each metal (Ag, Au, Cu, Ir, Pd, Pt, Rh) was modelled from converged FCC bulk structure. The slab consisted of four layers with the bottom two layers constrained. The unit cells for ZnO_xH_y monolayer films were made by the procedure described in our previous paper[37]. Using an in-house developed algorithm, the strain in non-pseudomorphic, periodic overlayer structures was minimized[38].

The site preference for CO adsorption on Pt(111) is not well represented by PBE functional[39]. Recently, Saeys et al[40] showed that revPBE-vdw[41,42] functional correctly describes the site preference. Therefore, we use similar VASP settings for the CO adsorption calculations.

3.4 Formation of ZnO and $Zn_6O_5H_5$ films on Pt(111)

We prepared zinc oxide and zinc hydroxide films on Pt(111) following the method reported in literature[16,28]. Zinc oxide films at sub monolayer coverage on Pt(111) surface were prepared by oxidative Zn deposition and post-oxidation in 5×10^{-7} mbar O_2 at 550 K, and zinc

hydroxide films can be prepared by a subsequent hydrogen treatment at room temperature. As shown in Figure 3.1a**,** monolayer films and a few bilayer islands formed on Pt(111) after post-oxidation, with apparent heights of 1.3±0.1Å and 3.1±0.1Å, respectively. The zinc oxide films formed in triangular-like shape and adopted the same orientations as Pt(111) substrate (indicated by the white guidelines in Figure 3.1a), suggesting epitaxial growth and good crystallinity. High resolution image confirmed that the film is the graphite-like (6x6) structure with a 16.8 Å periodicity[16,43], which is 6 times the Pt-Pt spacing (Figure 3.2).

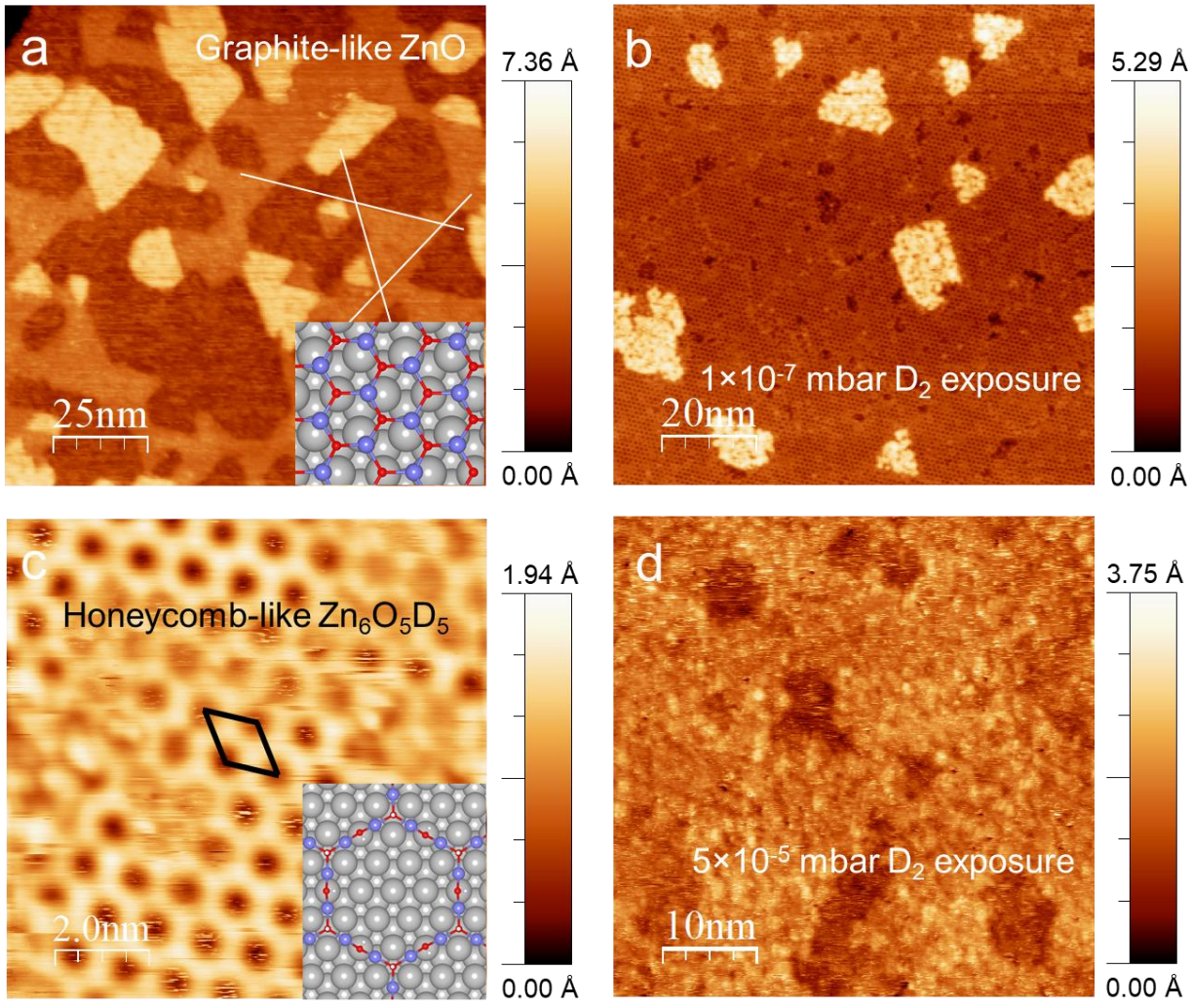

Figure 3.1. STM images of the zinc oxide/hydroxide films on Pt(111). (a) The pristine (6x6) films with a Zn coverage of 0.37 ML. The inset shows the model of the (6x6)-ZnO structure. (b) The surface after a 10-minute treatment in 1×10^{-7} mbar D_2 at room temperature. (c) High resolution image of the surface covered by the (4x4) structure. The rhombus indicates the unit cell. The inset shows the model of the (4x4)-$Zn_6O_5D_5$ structure. (d) Another 0.36 ML ZnO/Pt(111) sample after a 10-minute treatment in 5×10^{-5} mbar D_2 at room temperature. Violet: Zn, red: O, white: H/D, grey: Pt.

To form the honeycomb-like $Zn_6O_5H_5$ structure, the pristine ZnO/Pt(111) surface was treated in 1×10^{-7} mbar D_2 for 10 minutes. We used D_2 instead of H_2 throughout this study to help distinguish between residual and external hydrogen sources. STM showed that the monolayer (6x6) films completely changed into the honeycomb-like (4x4) structure which covers almost the entire Pt surface (Figure 3.1b). High-resolution image confirmed the ring structure with a 10.7±0.3Å periodicity, 4 times the Pt-Pt spacing (Figure 3.1c), which agrees with the (4x4) structure reported in literature and is modeled with a $Zn_6O_5H_5$ stoichiometry (inset of Figure 3.1c) [16,17]. In addition, some rings are filled in the STM image, which can be ascribed to either confined Zn species or adsorbed CO molecules from residual gas in the UHV chamber.

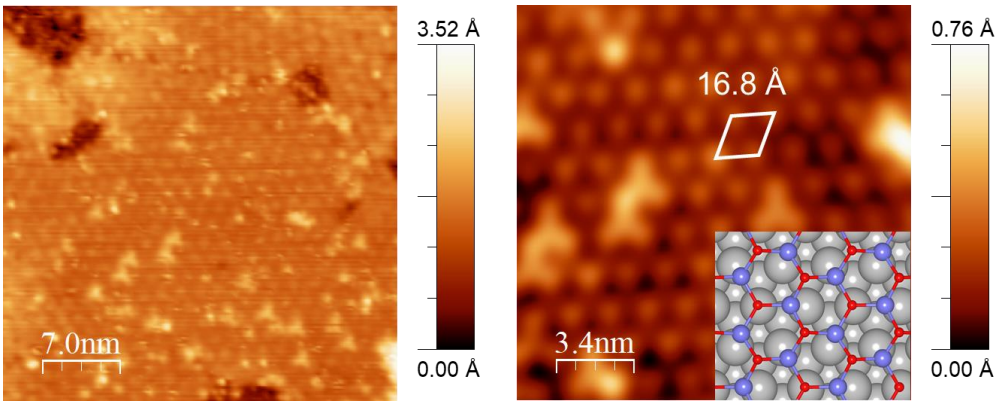

Figure 3.2. Magnified STM image of the graphite-like (6x6) structure. The periodicity of the Moiré pattern is measured to be 16.8 Å. The inset shows the model of the (6x6) structure. Pt, Zn, O atoms are indicated by grey, violet, and red balls, respectively.

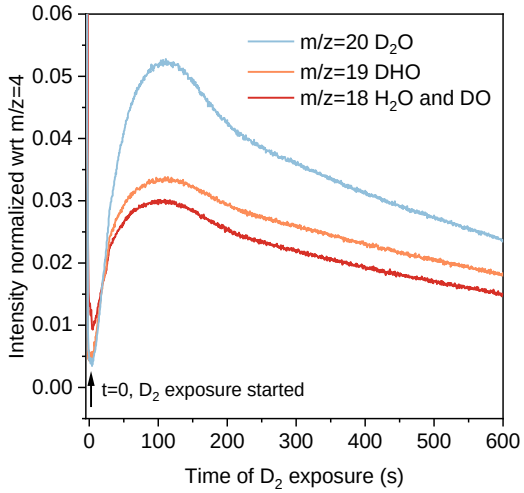

Figure 3.3. Mass spectrum collected during the 1×10^{-7} mbar D_2 treatment of the (6x6) structure.

The reaction of ZnO with D_2 is monitored by mass spectrometer during the treatment. DHO and D_2O fragments were detected to increase once the exposure started (Figure 3.3), thus the reaction can be expressed as $6\,ZnO + \frac{7}{2}\,D_2 \rightarrow Zn_6O_5D_5 + D_2O$. It is likely that D_2 is activated on Pt sites before spillover to ZnO films[16,28]. A highly mobile ZnO_xD_y (or ZnO_xH_y) species, instead of the previously proposed ZnO_x[16], accounts for the migration of zinc oxide on Pt surface. Moreover, when a high pressure of D_2 (5×10^{-5} mbar) was used for the transition, the reaction was too fast, and only amorphous structure was formed (Figure 3.1d). XPS and HREELS of the amorphous structure show similar features compared to the (4x4) structure (spectra not shown), indicating that they share the same building block, although the former failed to self-assemble into an ordered structure. This is analogous to the crystallization process that fast cooling results in poor crystallinity. Therefore, a moderate hydrogen pressure is required for successful assembly of ZnO_xD_y into the highly ordered (4x4).

3.5 Surface vibrations and oxidation states of ZnO and $Zn_6O_5H_5$

The percentage of hydroxylation was determined by the intensity of surface vibrations and O 1s XPS excitations. As shown in Figure 3.4a, an asymmetric ν(O-H) peak was observed on the (6x6) film, which can be deconvoluted into a major peak at 3589 cm^{-1} and a minor peak at 3515 cm^{-1}, accounting for the hydroxyl groups on the surface of the film and at the boundaries or defects[44], respectively. For the (4x4) structure, ν(O-D) peak at 2662 cm^{-1} and ν(O-H) peak at 3609 cm^{-1} were observed. The 20 cm^{-1} shift of the ν(O-H) peak towards high frequencies suggests different chemical environments of the hydroxyl groups on the (6x6) and (4x4) structures. The peak intensity of the (6x6) surface is also one order of magnitude smaller than that of the (4x4) surface, indicating that the major component of the (6x6) film is still non-hydroxylated zinc oxide, which will further be confirmed by XPS. Therefore, the (6x6) phase is referred to as ZnO throughout the text regardless of the partial hydroxylation, and the (4x4) phase is referred to as $Zn_6H_5O_5$.

The fitted O 1s XPS peak of the (6x6) shows two components at 529.0 eV and 531.3 eV, which can be attributed to Zn-O and Zn-O-H, respectively (Figure 3.4b). The latter one takes 16% of the total oxygen species, which agrees with HREELS measurement that the extent of

hydroxylation is small. In contrast, the O 1s signal of the (4x4) phase shows a major peak at 531.5 eV and a minor peak at 530.0 eV. Ideally the (4x4) phase only consists of a hydroxyl component, so the small portion at 530.0 eV can be ascribed to the bilayer islands remaining on the surface. There is a 0.2 eV difference between the hydroxyl groups on (6x6) and on (4x4), in agreement with the 20 cm^{-1} shift observed in the HREELS measurement.

As shown in Figure 3.4c, the Zn $2p_{3/2}$ XPS peak of the (6x6) structure is centered at 1020.7 eV, while the peak of the (4x4) structure shifted 0.7 eV towards higher binding energy, in agreement with the results obtained by Su et al.[28], suggesting a significant change in the chemical states of Zn in the two phases. Zn LMM auger peaks also showed corresponding changes. The auger peak involves multiple excitations and thus is interpreted in a fingerprint way. As shown in Figure 3.4d, the auger peak of the (6x6) is broad and centered at kinetic energy of 991.5 eV, while the auger peak of the (4x4) is narrowed and centered at 991.3 eV. Normally metallic Zn gives a narrow auger peak at 992.4 eV while Zn^{2+} gives broader peak centered at 989.0 eV[45,12], thus the (4x4) structure exhibits a lower oxidation state than Zn^{2+} but is not metallic. Taken together, the (4x4)-$Zn_6O_5H_5$ structure is unique in that the chemical composition and the geometry are significantly different from those of the common graphite-like ZnO structure on metal surfaces, and thus show a great potential for special modification of the catalytic properties of metal surfaces.

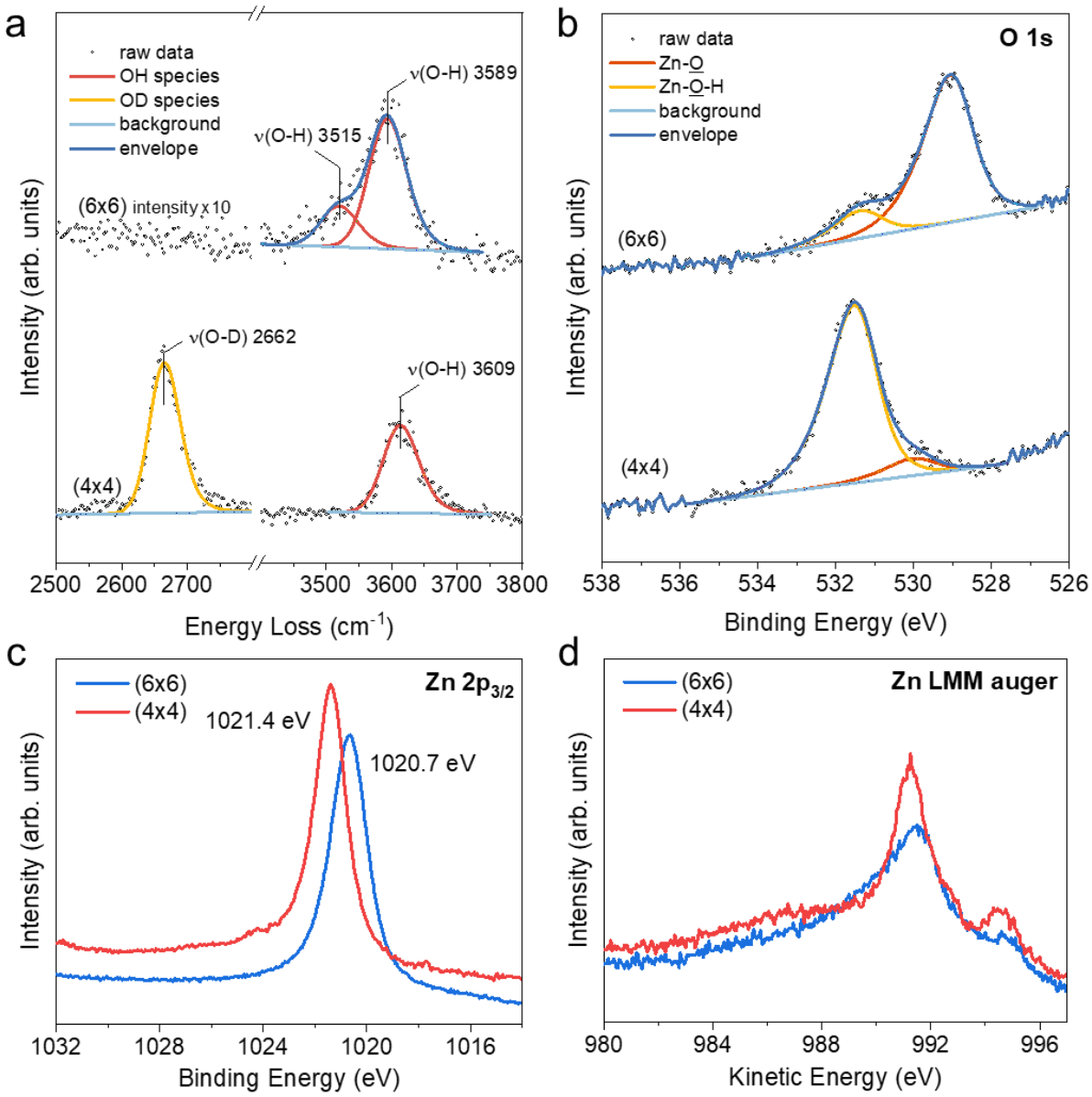

Figure 3.4. HREELS and XPS spectra of the (6x6) and the (4x4) structure. (a) ν(O-D) and ν(O-H) vibrations. The energy loss signal was normalized to the intensity of the elastic peak. (b) O 1s XPS peaks. (c) Zn $2p_{3/2}$ XPS peaks. (d) Zn $L_3M_{45}M_{45}$ auger peaks.

3.6 CO adsorption and desorption

The interactions of Pt with the two different zinc oxide and hydroxide films were investigated by CO adsorption measurements on clean Pt(111), ZnO/Pt(111), and

$Zn_6O_5H_5$/Pt(111) by HREELS. On clean Pt(111), CO molecules adsorb onto bridge and on-top sites at room temperature, giving two ν(CO) peaks at 1850 cm^{-1} and 2090 cm^{-1}, respectively (Figure 3.5a). The area ratio of the two peaks is 3:7. For ZnO/Pt(111) with 0.33 ML Zn coverage, after the same 10 L CO exposure, two peaks centered at 1855 cm^{-1} and 2095 cm^{-1} were observed, with a bridge-to-linear ratio of 3:7. The results indicated that the ZnO films did not change the chemical environment of the adjacent Pt patches, in other words, the electron transfer between compact ZnO and Pt is insignificant. Therefore, the nature of metal-oxide interaction in this case is solely geometric: ZnO-Pt boundary is created as a new type of active sites, but the property of Pt itself is unchanged.

On the other hand, after 10 L CO exposure, the 0.32 ML $Zn_6O_5H_5$/Pt(111) exhibited two peaks shifted towards lower frequencies. The bridging CO shows a stretching frequency at 1795 cm^{-1} and the linear CO shows a stretching frequency at 2040 cm^{-1} (Figure 3.5a). Moreover, the bridge-to-linear ratio now increased to 8:2, i.e., the dominant CO adsorption sites are the bridging sites. As demonstrated by STM (Figure 3.6a), the surface is almost completely covered by the (4x4), thus the major adsorption sites are the Pt atoms exposed within the $Zn_6O_5H_5$ rings. Therefore, the electronic environment of Pt atoms in the rings is altered by zinc hydroxide significantly, which will be illustrated by DFT calculations. It is worth noting that although the surface was covered visually, the amount of accessible active sites for CO adsorption is still large compared to ZnO/Pt(111) with a similar Zn coverage, as demonstrated by the intensity of ν(C-O) peaks. Comparing to ZnO islands, $Zn_6O_5H_5$ network modifies the surface more drastically, uniformly, and efficiently.

In order to investigate the adsorption energy of CO on the three different surfaces, we measured CO desorption by annealing each surface to 308 K, 323 K, and 338 K stepwise at a heating rate of 0.05 K/s. On Pt(111), the intensity of CO peaks gradually decreased during annealing, but the bridging-to-linear ratio was unchanged till 323 K (Figure 3.5b). CO desorbed completely when temperature reached 338 K. ZnO/Pt(111) showed similar behavior. CO peaks gradually decreased without changes in the bridging-to-linear ratio when the sample was annealed till 308 K. At the annealing temperature of 323 K, the bridging CO peaks disappeared due to the smaller coverage, and a small portion of linear CO remained, which further desorbed at 338 K. The results suggest that CO binding energy on Pt(111) was not affected by the ZnO films. In contrast, the bridging CO peak on $Zn_6O_5H_5$/Pt(111) decreased significantly while the

linear CO peak was unchanged upon annealing. At 338 K, the bridging CO desorbed completely, while the small linear peak remained on surface. The linear peak disappeared upon annealing to 373 K. In aggregate, the preference of bridging site adsorption, the shifted ν(C-O) stretching frequencies, and the selective desorption of bridging CO suggest that the surface chemistry of Pt have been changed by zinc hydroxide modification.

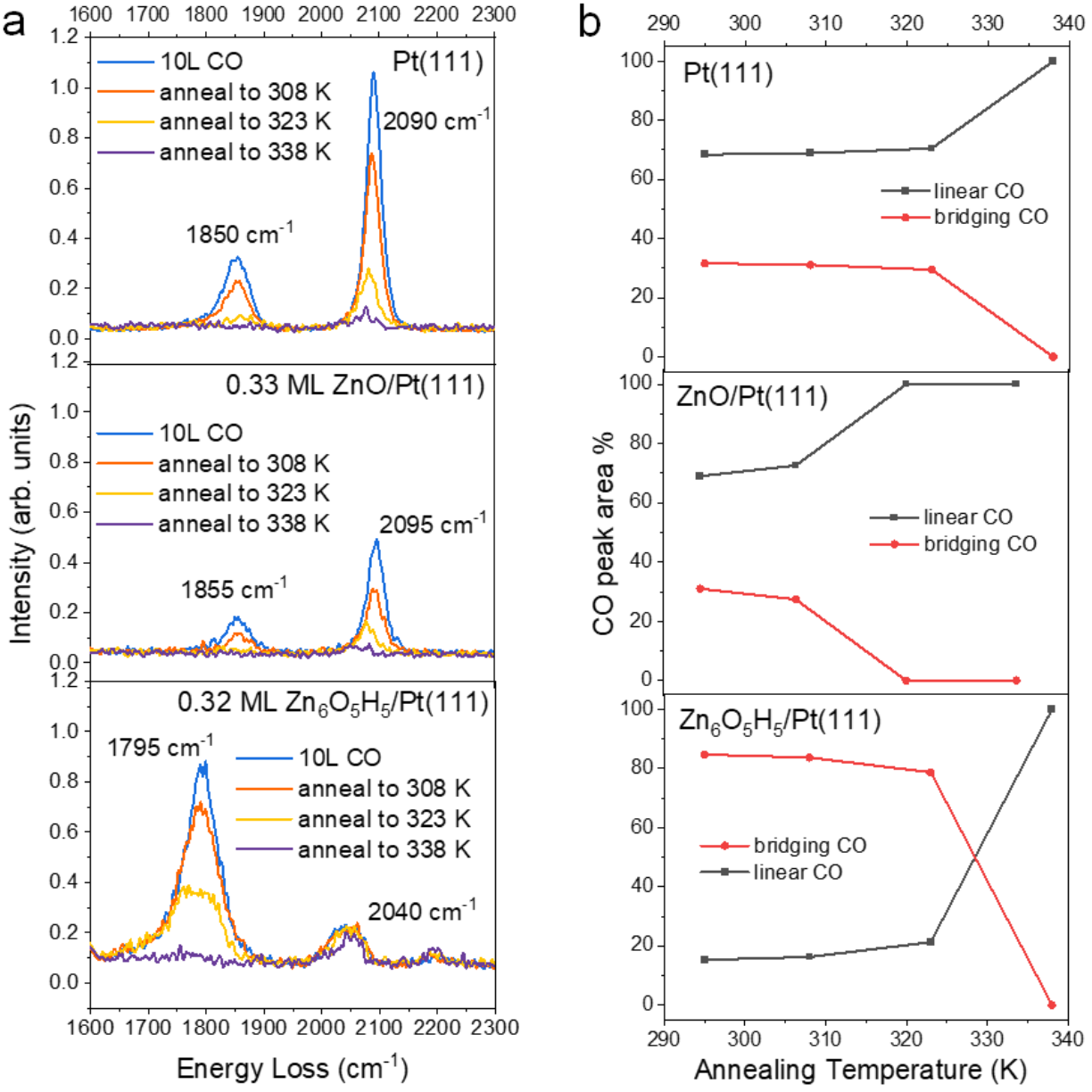

Figure 3.5. (a) HREELS spectra of CO adsorption on clean Pt(111), (6x6)-ZnO/Pt(111), and (4x4)-$Zn_6O_5H_5$/Pt(111). The coverage of zinc is controlled within 0.3~0.4 ML range. (b) CO peak area calculated from the HREELS peaks.

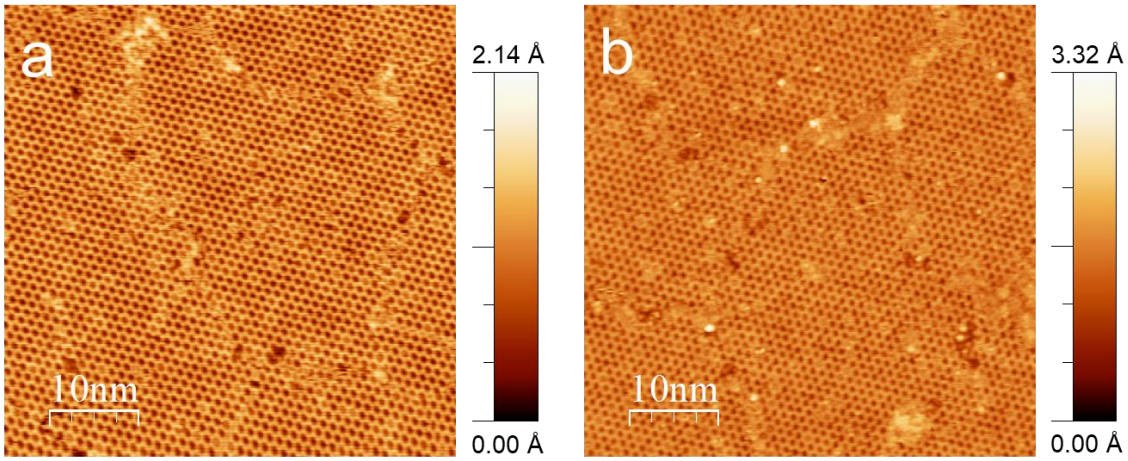

Figure 3.6. (a) STM image of the (4x4)-$Zn_6O_5H_5$/Pt(111) surface used for CO adsorption and desorption measurements. (b) STM image of the same sample after annealing to 338 K in UHV.

The surfaces after stepwise annealing were further examined to understand the thermal stability of films. XPS showed that ZnO was partially reduced after annealing to 338 K (Figure 3.7), indicating that (6x6) is very unstable in UHV conditions. STM (Figure 3.6b) of the annealed surface showed that the (4x4) structure remains stable. Extra treatments of $Zn_6O_5H_5$/Pt(111) samples (Figure 3.8) indicated that the (4x4) structure is stable in 5×10^{-5} mbar D_2 at room temperature. It is also stable in 1×10^{-7} mbar D_2 at 373 K but reduced to a PtZn alloy in 1×10^{-7} mbar D_2 at 473 K. In a word, the (4x4) structure is more stable than (6x6) under mild reducing conditions but is still prone to fully reduction under strong reducing conditions.

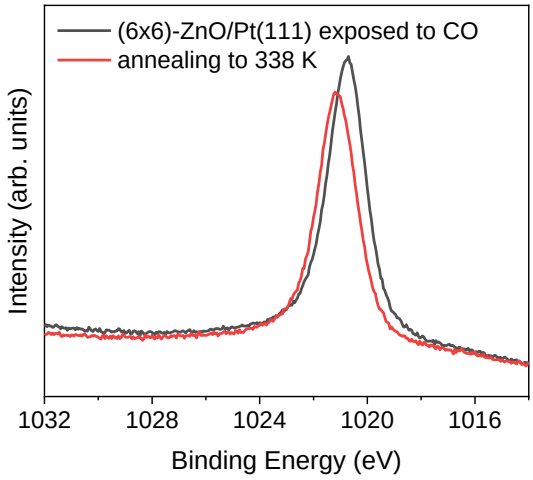

Figure 3.7. Zn $2p_{3/2}$ peaks of the (6x6) films after 10L CO exposure and after annealing to 338 K.

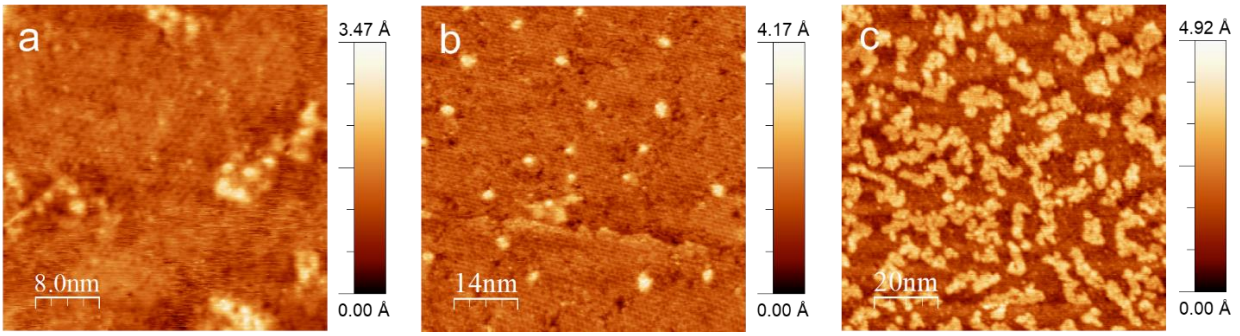

Figure 3.8. STM image of the (4x4) films treated under different conditions: (a) in 5×10^{-5} mbar D_2 at room temperature for 10 minutes. (b) in 1×10^{-7} mbar D_2 at 373 K for 10 minutes. (c) in 1×10^{-7} mbar D_2 at 473 K for 10 minutes.

In addition to the highly ordered (6x6) and (4x4) structures, we also investigated room temperature CO adsorption on the amorphous ZnO_xH_y structure (Figure 3.1d and 3.9a) which is formed by rapid hydroxylation of zinc oxide. As shown in Figure 3.9b, there were two ν(C-O) peaks at 2040 and 2180 cm^{-1}, respectively. The former one is on-top CO adsorbed on Pt sites, while the frequency of the latter one is too far away from CO species on Pt, and thus is ascribed to CO adsorbed on ionic Zn sites. The adsorption of CO on Zn is unusual to occur at room temperature since previous studies showed that CO desorbs from zinc oxide crystal surface at 130 K[46] and from zinc oxide thin films at 200 K[45]. Therefore, we proposed that the coordination of the Zn sites in the amorphous hydroxide structure is unsaturated, and thus is susceptible to CO adsorption. STM also imaged some bright dots at the grain boundaries of (4x4) films (Figure 3.9c) in accompany with a small peak at 2195 cm^{-1}, supporting the assignment of the high frequency peak to CO on unsaturated Zn sites. The unprecedented strong CO adsorption on Zn sites indicates that the defect sites of zinc hydroxide is more active than well-ordered zinc hydroxide and zinc oxide.

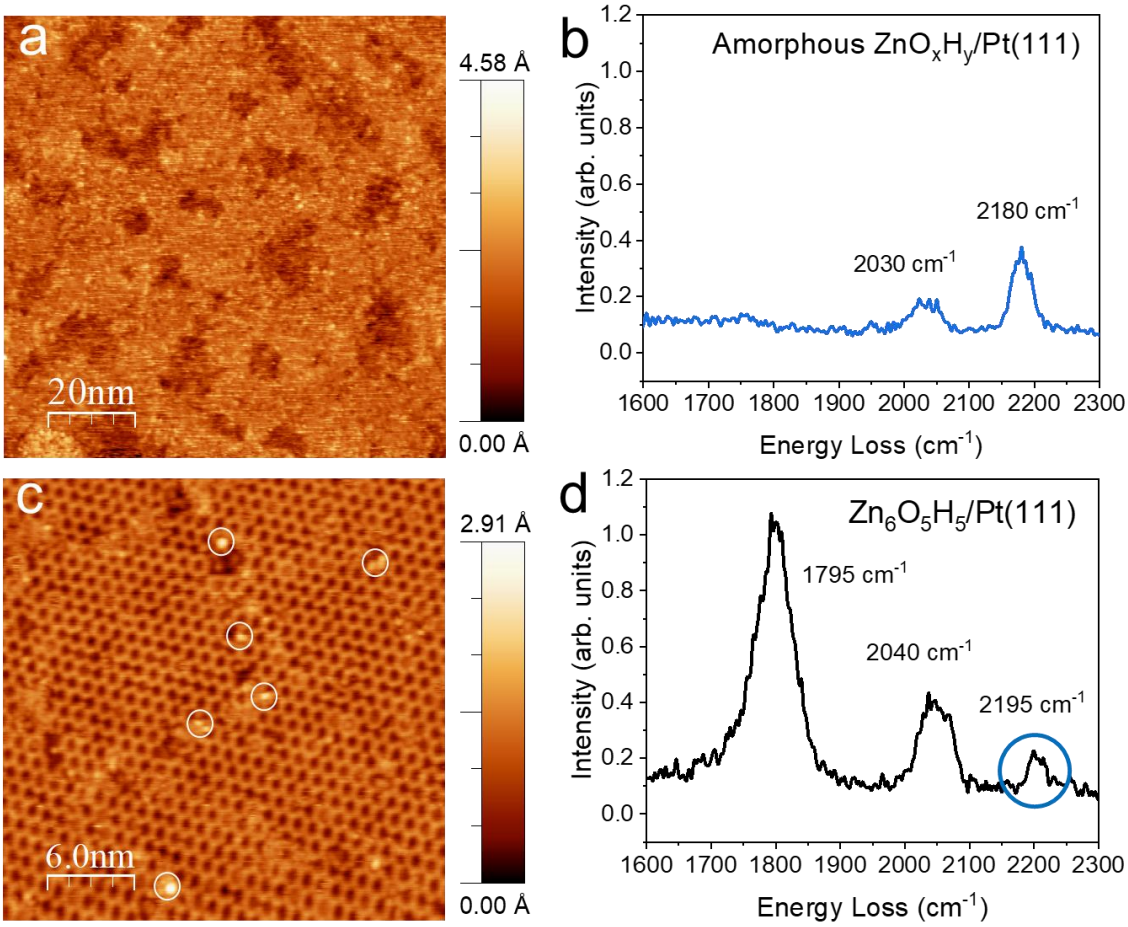

Figure 3.9. (a,b) STM image and HREELS spectrum of amorphous zinc hydroxide structure on Pt(111) exposed to 10 L CO at 295 K. (c,d) STM image and HREELS spectrum showing that CO molecules (circled in white) adsorbed on the grain boundary of (4x4)-$Zn_6O_5H_5$ films resulted in the high ν(C-O) frequency.

3.7 Ethylene adsorption

Selective acetylene hydrogenation is used for purification of ethylene feedstocks to produce polyethylene. Pt exhibits poor selectivity for this reaction since the strong adsorption of ethylene leading to deeper hydrogenation to ethane[45]. Ethylene molecules form stable ethylidyne (*CCH_3) species once adsorbed onto Pt(111) at room temperature[48,49]. Herein, we investigated the adsorption of ethylene and formation of ethylidyne on Pt(111) and $Zn_6O_5H_5$/Pt(111) by *in situ* HREELS.

As shown in Figure 3.10, C_2H_4 forms ethylidyne species on Pt(111) at 295 K, as evidenced by peaks at 1125, 1345, 2890, and 2950 cm^{-1}, which are ascribed to C-C stretching, CH_3 symmetric scissoring, C-H symmetric stretching, and C-H asymmetric stretching, respectively[48]. The low vibrational frequencies of C-H stretching are characteristic of sp^3-hybridization, supporting the assignment of ethylidyne species. The two peaks at 425 and 475 cm^{-1} are due to Pt-C stretching from Pt-C_2H_4 and Pt-CO bonding. For $Zn_6O_5H_5$/Pt(111), peaks at 450 and 975 cm^{-1} are ascribed to zinc hydroxide phonon peaks, since the two peaks did not change when the measurement condition changed from UHV to 1.5×10^{-8} mbar C_2H_4 atmosphere. A small peak at 1345 cm^{-1} is observed when the surface exposed to C_2H_4, indicating that the adsorption form does not change on the modified surface, but ethylidyne coverage deceased significantly. The C-H stretching peaks are also invisible due to the small surface coverage. The weakened intensity indicates that a large portion of Pt does not involve in C_2H_4 adsorption. Combining STM, there are small Pt patches uncovered by the (4x4) structure (Figure 3.11), and therefore, it could be deduced that ethylene only adsorbs on the uncovered Pt patches, and Pt atoms in $Zn_6O_5H_5$ rings do not participate in ethylidyne formation. In short, the $Zn_6O_5H_5$ rings weakened the adsorption of ethylene on Pt, which is the desired product of selective acetylene hydrogenation, and thus may inhibit deeper hydrogenation to ethane and contribute to a higher selectivity if applied in technical catalyst systems.

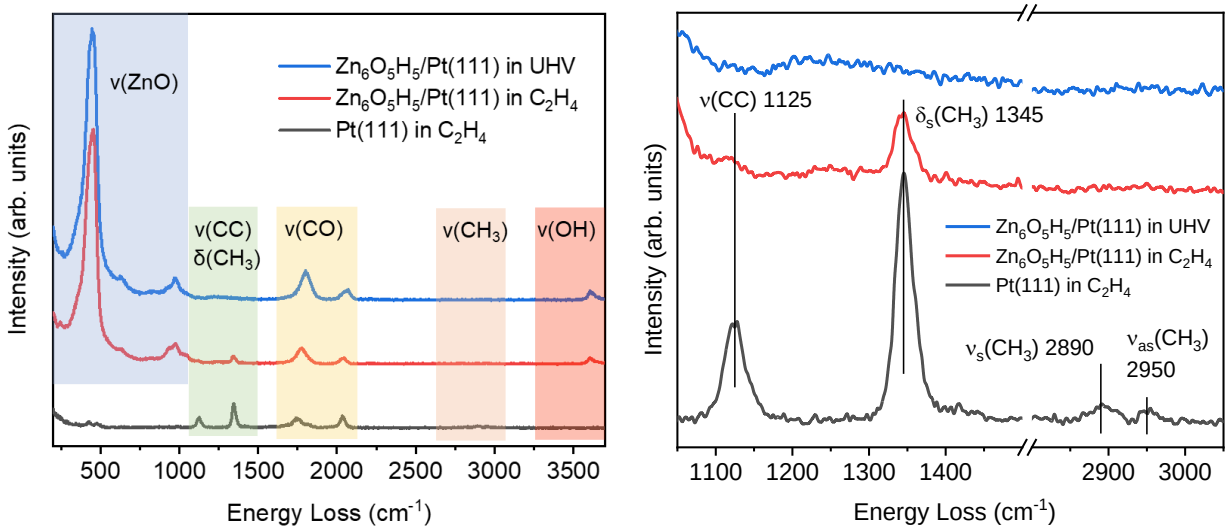

Figure 3.10. HREELS spectra of $Zn_6O_5H_5$/Pt(111) measured in UHV (blue line), in 1.5×10^{-8} mbar (red line) and bare Pt(111) measured in 1.5×10^{-8} mbar (black line). All the spectra were collected at 295 K. The right panel is the magnified spectra of selected hydrocarbon vibration regions.

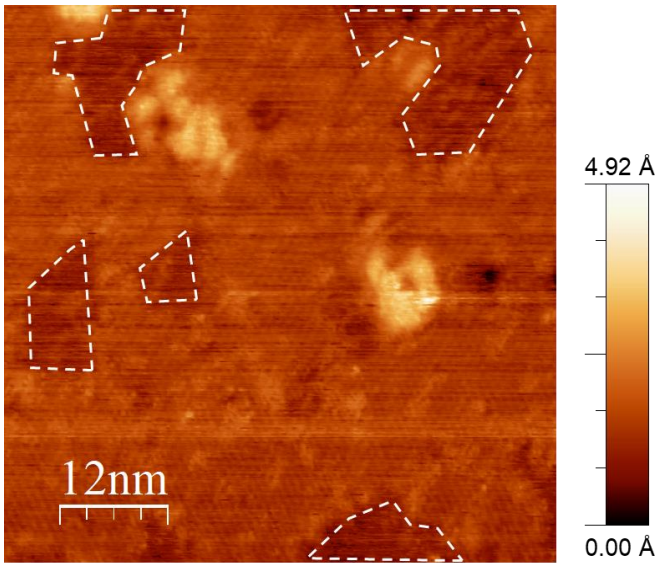

Figure 3.11. STM image of the (4x4)-$Zn_6O_5H_5$/Pt(111) surface used for C_2H_4 adsorption measurements. The white boxes indicate bare Pt patches.

3.8 NO adsorption and reaction

Nitric oxide (NO) and CO shared similar molecular orbital configuration, making it another important probe molecule for the study of surface chemistry. In addition, Nitric oxide is generated in combustion systems and the conversion of NO is crucial for environment protection. It has been well studied that NO adsorbs on Pt(111) molecularly and behaves inertly[50], but the addition of zinc hydroxide might provide extra active sites for NO molecules.

As shown in Figure 3.12a, Exposing clean Pt(111) to 10 L NO at room temperature resulted in a peak at 1455 cm^{-1}, ascribing to the NO molecules adsorbed onto three-fold Pt sites. Exposing fresh $Zn_6(OH)_5$/Pt(111) to 10 L NO at room temperature resulted in the same peak with weaker intensity. Intense CO peaks were also observed on both surfaces, since residual CO binds with Pt more strongly than NO and adsorbed onto the surface during long time data acquisition (~1 hour). STM showed that after NO exposure, $Zn_6O_5H_5$ changed into irregular monolayer islands with an apparent height of 1.3 Å, as shown in Figure 3.12b. Hydroxyl groups were retained on the transformed surface at the same frequencies, and XPS indicated little changes in chemical states of Zn (spectrum not shown). Since NO behaves inert on Pt(111), NO was more likely to interact with zinc hydroxide directly.

To confirm the hypothesis, we intentionally blocked Pt sites by external CO exposure in advance, and then exposed the CO adsorbed $Zn_6O_5H_5$/Pt(111) to 10 L NO. The structural transformation still occurred, as evidenced by the irregular islands with the same apparent height observed by STM (Figure 3.12c), indicating that NO was activated on zinc hydroxide without the assistance of Pt, and in turn, zinc hydroxide was disassembled into mobile ZnO_xH_y species which further formed the 1.3 Å high islands. Once these islands formed, D_2 treatment cannot recover the honeycomb-like (4x4) structure.

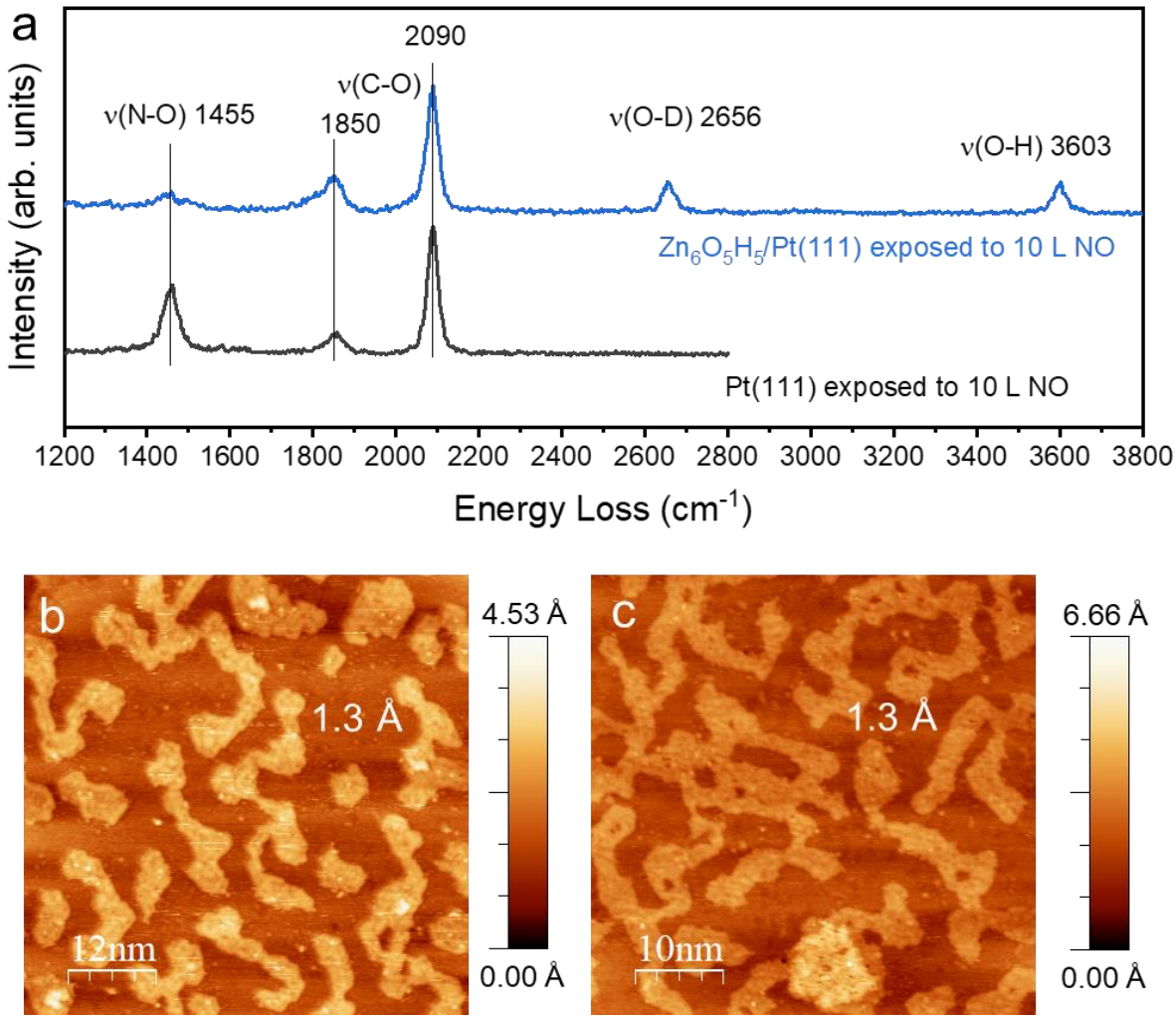

Figure 3.12. (a) HREELS spectrum of Pt(111) and (4x4)-$Zn_6O_5H_5$/Pt(111) after 10 L NO exposure at room temperature. (b) STM image of the (4x4)-$Zn_6O_5H_5$/Pt(111) after 10 L NO exposure at room temperature. (c) STM image of the (4x4)-$Zn_6O_5H_5$/Pt(111) after 10 L CO and 10 L NO exposure at room temperature.

However, when the $Zn_6O_5H_5$/Pt(111) was exposed to a NO/D_2 mixture with a ratio of 1:4, the surface was kept unchanged (Figure 3.13a). In other words, D_2 prevented the modification of the surface induced by NO, likely through the reaction between NO and D_2. To investigate the interaction among $Zn_6O_5H_5$, NO, and D_2, and more specifically, to distinguish if NO binds through OH (OD) or Zn, we prepared the $Zn_6O_5H_5$ films with only H and exposed to D_2 or D_2/NO mixture. As shown in Figure 3.13b, when exposing $Zn_6O_5H_5$ films to 2×10^{-7} mbar D_2 for 10 minutes, isotope exchange occurred due to the dissociation and recombination of hydrogen at Pt sites, leading to an OD:OH ratio of 5:5. If NO reacts with the OH groups, H will leave the surface in the product and D will be replenished through D_2 dissociation and spillover on Pt, leading to a higher OD:OH ratio. However, HREELS showed that when exposing $Zn_6O_5H_5$ films to 2×10^{-7} mbar D_2 and 5×10^{-8} mbar NO for 10 minutes, OD:OH ratio of the surface was 4:6, excluding the proposed pathway. Therefore, it is plausible that NO binds with Zn while D_2 dissociates on proximate Pt, and the reaction occurs at the hydroxide-metal boundaries; since part of D atoms react with NO, the percentage of OD groups is less than that of the control sample. We would like to point out that due to the limitation of small size of model catalyst and low reaction rate, we were not able to detect any reaction products or intermediates by MS or HREELS.

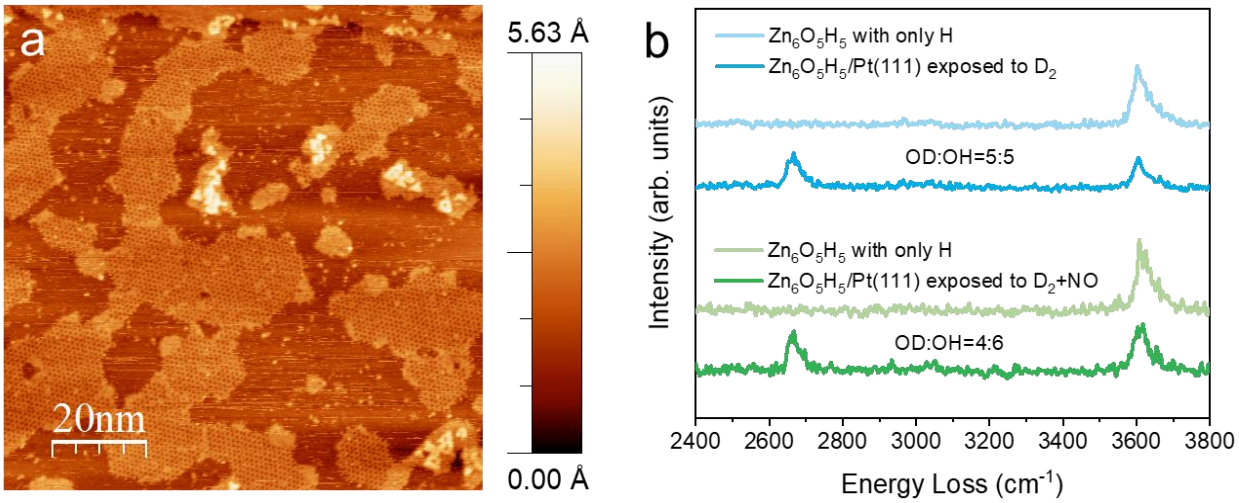

Figure 3.13. (a) STM image the (4x4)-$Zn_6O_5H_5$/Pt(111) after exposure to 2×10^{-7} mbar D_2 and 5×10^{-8} mbar NO for 10 minutes. (b) HREELS spectra of fresh $Zn_6O_5H_5$/Pt(111) and $Zn_6O_5H_5$/Pt(111) exposed to 2×10^{-7} mbar D_2 or 2×10^{-7} mbar D_2 and 5×10^{-8} mbar NO mixture, respectively.

3.9 Theoretical results

We used DFT calculations to better understand the experimentally observed CO adsorption behavior. Herein, we considered CO adsorption on the bare Pt(111) and $Zn_6O_5H_5$/Pt(111) surface to directly compare with experimental observations. Saeys *et al.*[40] reported that the rev-PBE functional accurately describes the CO adsorption site preference on bare Pt(111) surfaces. We used the calibrated DFT settings to calculate CO adsorption on the ring like $Zn_6O_5H_5$/Pt(111) surface. All the surface bridge and top sites were exhaustively studied to find the most energetically stable configuration. The results are summarized in Table 3.1a. Remarkably, we found that DFT accurately predicts that CO on $Zn_6O_5H_5$/Pt(111) prefers the bridge site rather than the top site. Saeys *et al.* reported that such a switch in CO adsorption preference is observed when the Pt substrate has excess negative charge. The negative charge adversely affects the CO adsorption and reduces the binding energy.

Table 3.1. (a) Gibbs free adsorption energy of CO adsorption referenced to gas phase CO (1×10^{-7} mbar, 300K). (b) DFT predicted adsorbed CO frequencies.

(a) Adsorption Energy (eV)	**Top**	**Bridge**
Bare Pt(111) (3x3)	-0.73	-0.69
$Zn_6H_5O_5$/Pt(111)	-0.66	-0.77

(b) CO Frequency (cm^{-1})	**Top**	**Bridge**
Bare Pt(111) (3x3)	2015	1805
$Zn_6H_5O_5$/Pt(111)	1971	1720

Using a Bader charge analysis, we found that the ring like $Zn_6O_5H_5$ film donates 0.49 electrons per Zn to the Pt slab. Although, majority of the charge is concentrated near the Zn atoms, there is spillover to adjacent Pt atoms as well (Figure 3.14a). The binding energy of CO on top site of $Zn_6O_5H_5$/Pt(111) surface is weaker than bare Pt(111), which is consistent with previous studies. However, the binding energy of CO on bridge site of $Zn_6O_5H_5$/Pt(111) surface is stronger than bare Pt(111). The discrepancy can be attributed to the favorable interaction between the OH in the ring structure and the CO, in addition to the destabilization due to charge transfer. Moving the OH away from the bridge CO led to decrease in the adsorption energy by

0.09 eV. Therefore, the ring like $Zn_6O_5H_5$ film can electronically as well as chemically affect the CO adsorption. Secondly, we observed that DFT predicts systematically lower frequencies as compared to experiment, but the values are within DFT error (~5%). The calculations correctly captures that CO vibration frequencies on the ring like $Zn_6O_5H_5$ structure are lower than bare Pt(111). Overall, the theoretical results show perfect consistency with experimental observations.

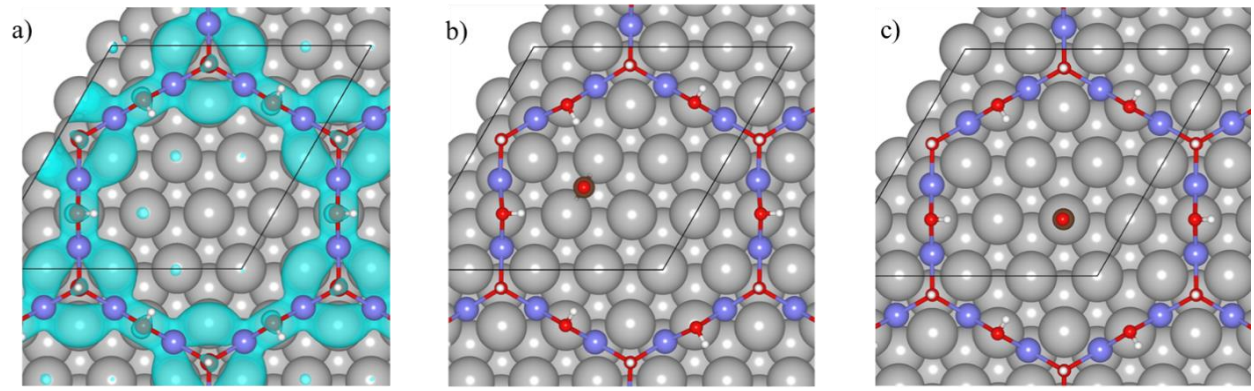

Figure 3.14. (a) Top view of charge difference plot of $Zn_6(OH)_5$/Pt(111). The light blue regions represent accumulation of negative charge. (b) Top view of CO adsorbed on a bridge site on $Zn_6(OH)_5$/Pt(111). (c) Top view of CO adsorbed on a top site on $Zn_6(OH)_5$/Pt(111). The Pt, Zn, O, C, and H atoms are represented by grey, purple, red, brown, and white colored balls.

3.10 Conclusions

In this work, by investigating the structure and surface chemistry of Pt(111), graphite-like (6x6)-ZnO/Pt(111), and honeycomb-like (4x4)-$Zn_6O_5H_5$/Pt(111), we distinguished metal-hydroxide interaction from traditional metal-oxide interactions. Unlike the compact (6x6)-ZnO films, the (4x4)-$Zn_6O_5H_5$ films tune the CO adsorption on Pt sites from linear to bridging positions and change the binding energy of CO on Pt, via charge transfer from Zn to Pt and OH + CO interaction. Moreover, the (4x4)-$Zn_6O_5H_5$/Pt(111) show a weakened ethylidyne formation compared to bare Pt(111), widen the possibility of utilizing Pt as a selective semi-hydrogenation catalyst. By forming the $Zn_6O_5H_5$ network on Pt surface, we created new metal-hydroxide boundary sites with little sacrifice of the total exposed Pt atoms. In summary, this work provides an approach to engineer the Pt catalytic surface uniformly and effectively, and the application of

zinc hydroxide decoration may be promising in some reactions performed under mild reducing conditions.

3.11 References

(1) Shishido, T.; Yamamoto, M.; Li, D.; Tian, Y.; Morioka, H.; Honda, M.; Sano, T.; Takehira, K. Water-Gas Shift Reaction over Cu/ZnO and Cu/ZnO/Al_2O_3 Catalysts Prepared by Homogeneous Precipitation. *Appl. Catal. A Gen.* **2006**, *303*, 62–71.

(2) Spencer, M. S. The Role of Zinc Oxide in Cu/ZnO Catalysts for Methanol Synthesis and the Water-Gas Shift Reaction. *Top. Catal.* **1999**, *8*, 259–266.

(3) Peppley, B. A.; Amphlett, J. C.; Kearns, L. M.; Mann, R. F. Methanol-Steam Reforming on Cu/ZnO/Al_2O_3. Part 1: The Reaction Network. *Appl. Catal. A Gen.* **1999**, *179*, 21–29.

(4) Peppley, B. A.; Amphlett, J. C.; Kearns, L. M.; Mann, R. F. Methanol-Steam Reforming on Cu/ZnO/Al_2O_3 Catalysts. Part 2. A Comprehensive Kinetic Model. *Appl. Catal. A Gen.* **1999**, *179*, 31–49.

(5) Iwasa, N.; Masuda, S.; Takezawa, N. Steam Reforming of Methanol over Ni, Co, Pd and Pt Supported on ZnO. *React. Kinet. Catal. Lett.* **1995**, *55*, 349–353.

(6) Chin, Y. H.; Wang, Y.; Dagle, R. A.; Li, X. S. Methanol Steam Reforming over Pd/ZnO: Catalyst Preparation and Pretreatment Studies. *Fuel Process. Technol.* **2003**, *83*, 193–201.

(7) Xu, J.; Su, X.; Liu, X.; Pan, X.; Pei, G.; Huang, Y.; Wang, X.; Zhang, T.; Geng, H. Methanol Synthesis from CO_2 and H_2 over Pd/ZnO/Al_2O_3: Catalyst Structure Dependence of Methanol Selectivity. *Appl. Catal. A Gen.* **2016**, *514*, 51–59.

(8) Lunkenbein, T.; Schumann, J.; Behrens, M.; Schlögl, R.; Willinger, M. G. Formation of a ZnO Overlayer in Industrial Cu/ZnO/Al_2O_3 Catalysts Induced by Strong Metal-Support Interactions. *Angew. Chemie Int. Ed.* **2015**, *54*, 4544–4548.

(9) Behrens, M.; Studt, F.; Kasatkin, I.; Kühl, S.; Hävecker, M.; Abild-pedersen, F.; Zander, S.; Girgsdies, F.; Kurr, P.; Kniep, B.; Tovar, M.; Fischer, R. W.; Nørskov, J. K.; Schlögl, R. The Active Site of Methanol Synthesis over Cu/ZnO/Al_2O_3 Industrial Catalysts. *Science.* **2012**, *336*, 893–897.

(10) Kattel, S.; Ramírez, P. J.; Chen, J. G.; Rodriguez, J. A.; Liu, P. Active Sites for CO_2 Hydrogenation to Methanol on Cu/ZnO Catalysts. *Science.* **2017**, *355*, 1296–1299.

(11) Kast, P.; Friedrich, M.; Girgsdies, F.; Kröhnert, J.; Teschner, D.; Lunkenbein, T.; Behrens, M.; Schlögl, R. Strong Metal-Support Interaction and Alloying in Pd/ZnO Catalysts for CO Oxidation. *Catal. Today* **2016**, *260*, 21–31.

(12) Li, D.; Xu, F.; Tang, X.; Dai, S.; Pu, T.; Liu, X.; Tian, P.; Xuan, F.; Xu, Z.; Wachs, I. E.; Zhu, M. Induced Activation of the Commercial Cu/ZnO/Al_2O_3 Catalyst for the Steam Reforming of Methanol. *Nat. Catal.* **2022**.

(13) Tauster, S. J.; Fung, S. C.; Garten, R. L. Strong Metal-Support Interactions. Group 8 Noble Metals Supported on TiO_2. *J. Am. Chem. Soc.* **1978**, *100*, 170–175.

(14) Meyer, B.; Marx, D.; Dulub, O.; Diebold, U.; Kunat, M.; Langenberg, D.; Wöll, C. Partial Dissociation of Water Leads to Stable Superstructures on the Surface of Zinc Oxide. *Angew. Chemie Int. Ed.* **2004**, *43*, 6641–6645.

(15) Grånäs, E.; Busch, M.; Arndt, B.; Creutzburg, M.; Semione, G. D. L.; Gustafson, J.; Schaefer, A.; Vonk, V.; Grönbeck, H.; Stierle, A. Role of Hydroxylation for the Atomic Structure of a Non-Polar Vicinal Zinc Oxide. *Commun. Chem.* **2021**, *4*, 1–8.

(16) Liu, B. H.; McBriarty, M. E.; Bedzyk, M. J.; Shaikhutdinov, S.; Freund, H. J. Structural Transformations of Zinc Oxide Layers on Pt(111). *J. Phys. Chem. C* **2014**, *118*, 28725–28729.

(17) Weirum, G.; Barcaro, G.; Fortunelli, A.; Weber, F.; Schennach, R.; Surnev, S.; Netzer, F. P. Growth and Surface Structure of Zinc Oxide Layers on a Pd(111) Surface. *J. Phys. Chem. C* **2010**, *114*, 15432–15439.

(18) Zhang, Z.; Chen, X.; Kang, J.; Yu, Z.; Tian, J.; Gong, Z.; Jia, A.; You, R.; Qian, K.; He, S.; Teng, B.; Cui, Y.; Wang, Y.; Zhang, W.; Huang, W. The Active Sites of Cu–ZnO Catalysts for Water Gas Shift and CO Hydrogenation Reactions. *Nat. Commun.* **2021**, *12*, 6–14.

(19) Claeyssens, F.; Freeman, C. L.; Allan, N. L.; Sun, Y.; Ashfold, M. N. R.; Harding, J. H. Growth of ZnO Thin Films - Experiment and Theory. *J. Mater. Chem.* **2005**, *15*, 139–148.

(20) Tusche, C.; Meyerheim, H. L.; Kirschner, J. Observation of Depolarized ZnO(0001) Monolayers: Formation of Unreconstructed Planar Sheets. *Phys. Rev. Lett.* **2007**, *99*, 2–5.

(21) Deng, X.; Yao, K.; Sun, K.; Li, W. X.; Lee, J.; Matranga, C. Growth of Single- and Bilayer ZnO on Au(111) and Interaction with Copper. *J. Phys. Chem. C* **2013**, *117*, 11211–11218.

(22) Pan, Q.; Liu, B. H.; McBriarty, M. E.; Martynova, Y.; Groot, I. M. N.; Wang, S.; Bedzyk, M. J.; Shaikhutdinov, S.; Freund, H. J. Reactivity of Ultra-Thin ZnO Films Supported by Ag(111) and Cu(111): A Comparison to ZnO/Pt(111). *Catal. Letters* **2014**, *144*, 648–655.

(23) Liu, B. H.; Boscoboinik, J. A.; Cui, Y.; Shaikhutdinov, S.; Freund, H. J. Stabilization of Ultrathin Zinc Oxide Films on Metals: Reconstruction versus Hydroxylation. *J. Phys. Chem. C* **2015**, *119*, 7842–7847.

(24) Yu, X.; Roth, J. P.; Wang, J.; Sauter, E.; Nefedov, A.; Heißler, S.; Pacchioni, G.; Wang, Y.; Wöll, C. Chemical Reactivity of Supported ZnO Clusters: Undercoordinated Zinc and Oxygen Atoms as Active Sites. *ChemPhysChem* **2020**, *21*, 2553–2564.

(25) Shaikhutdinov, S.; Freund, H.-J. Ultrathin Oxide Films on Metal Supports: Structure-Reactivity Relations. *Annu. Rev. Phys. Chem.* **2012**, *63*, 619–633.

(26) Martynova, Y.; Liu, B.-H.; McBriarty, M. E.; Groot, I. M. N.; Bedzyk, M. J.; Shaikhutdinov, S.; Freund, H.-J. CO Oxidation over ZnO Films on Pt(111) at near-Atmospheric Pressures. *J. Catal.* **2013**, *301*, 227–232.

(27) Liu, H.; Zakhtser, A.; Naitabdi, A.; Rochet, F.; Bournel, F.; Salzemann, C.; Petit, C.; Gallet, J.-J.; Jie, W. Operando Near Ambient Pressure XPS Study of the CO Oxidation Reaction on the Oxide/Metal Model Catalyst ZnO/Pt(111). *ACS Catal.* **2019**, *9*, 10212–10225.

(28) Su, N.; Mu, R.; Wu, H.; Zhang, R.; Zhao, S.; Li, Y.; Fu, Q.; Bao, X. Active Sites for H_2 and H_2O Activation over Bifunctional ZnO-Pt(111) Model Catalysts. *Appl. Surf. Sci.* **2020**, *503*, 144204.

(29) Fadley, C. S. Basic Concepts of X-Ray Photoelectron Spectroscopy. *Electron Spectrosc. theory, Tech. Appl.* **1978**, *2*, 1–156.

(30) Paul, R.; Reifenberger, R. G.; Fisher, T. S.; Zemlyanov, D. Y. Atomic Layer Deposition of FeO on Pt(111) by Ferrocene Adsorption and Oxidation. *Chem. Mater.* **2015**, *27*, 5915–5924.

(31) Gharachorlou, A.; Detwiler, M. D.; Nartova, A. V.; Lei, Y.; Lu, J.; Elam, J. W.; Delgass, W. N.; Ribeiro, F. H.; Zemlyanov, D. Y. Palladium Nanoparticle Formation on TiO_2(110) by Thermal Decomposition of Palladium(II) Hexafluoroacetylacetonate. *ACS Appl. Mater. Interfaces* **2014**, *6*, 14702–14711.

(32) Horcas, I.; Fernández, R.; Gómez-Rodríguez, J. M.; Colchero, J.; Gómez-Herrero, J.; Baro, A. M. WSXM: A Software for Scanning Probe Microscopy and a Tool for Nanotechnology. *Rev. Sci. Instrum.* **2007**, *78*, 013705–013712.

(33) Kresse, G.; Furthmüller, J. Efficient Iterative Schemes for Ab Initio Total-Energy Calculations Using a Plane-Wave Basis Set. *Phys. Rev. B* **1996**, *54*, 11169–11186.

(34) Kresse, G.; Furthmüller, J. Efficiency of Ab-Initio Total Energy Calculations for Metals and Semiconductors Using a Plane-Wave Basis Set. *Comput. Mater. Sci.* **1996**, *6*, 15–50.

(35) Kresse, G.; Joubert, D. From Ultrasoft Pseudopotentials to the Projector Augmented-Wave Method. *Phys. Rev. B* **1999**, *59*, 1758–1775.

(36) Perdew, J. P.; Burke, K.; Ernzerhof, M. Generalized Gradient Approximation Made Simple. *Phys. Rev. Lett.* **1996**, *77*, 3865–3868.

(37) Gao, J.; Sawant, K. J.; Miller, T.; Zeng, Z.; Zemlyanov, D.; Greeley, P. Structural and Chemical Transformations of Zinc Oxide Ultrathin Films on Pd (111) Surfaces. *ACS Appl. Mater. Interfaces* **2021**, *13*, 35113–35123.

(38) Zeng, Z.; Chang, K. C.; Kubal, J.; Markovic, N. M.; Greeley, J. Stabilization of Ultrathin (Hydroxy)Oxide Films on Transition Metal Substrates for Electrochemical Energy Conversion. *Nat. Energy* **2017**, *2*, 1–9.

(39) Feibelman, P. J.; Hammer, B.; Wagner, F.; Scheffler, M.; Stumpf, R.; Watwe, R.; Dumesic, J. The CO/Pt(111) Puzzle †. *J. Phys. Chem. B* **2001**, 105, 4018–4025.

(40) Kalhara Gunasooriya, G. T. K.; Saeys, M. CO Adsorption Site Preference on Platinum: Charge Is the Essence. *ACS Catal.* **2018**, *8*, 3770–3774.

(41) Klime, J.; Bowler, D. R.; Michaelides, A. Van Der Waals Density Functionals Applied to Solids. *Phys. Rev. B - Condens. Matter Mater. Phys.* **2011**, *83*, 1–29.

(42) Dion, M.; Rydberg, H.; Schröder, E.; Langreth, D. C.; Lundqvist, B. I. Van Der Waals Density Functional for General Geometries. *Phys. Rev. Lett.* **2004**.

(43) Martynova, Y.; Liu, B. H.; McBriarty, M. E.; Groot, I. M. N.; Bedzyk, M. J.; Shaikhutdinov, S.; Freund, H. J. CO Oxidation over ZnO Films on Pt(111) at near-Atmospheric Pressures. *J. Catal.* **2013**, *301*, 227–232.

(44) Gankanda, A.; Cwiertny, D. M.; Grassian, V. H. Role of Atmospheric CO_2 and H_2O Adsorption on ZnO and CuO Nanoparticle Aging: Formation of New Surface Phases and the Impact on Nanoparticle Dissolution. *J. Phys. Chem. C* **2016**, *120*, 19195–19203.

(45) Schott, V.; Oberhofer, H.; Birkner, A.; Xu, M.; Wang, Y.; Muhler, M.; Reuter, K.; Wöll, C. Chemical Activity of Thin Oxide Layers: Strong Interactions with the Support Yield a New Thin-Film Phase of ZnO. *Angew. Chemie Int. Ed.* **2013**, *52*, 11925–11929.

(46) Yang, C.; Wöll, C. IR Spectroscopy Applied to Metal Oxide Surfaces: Adsorbate Vibrations and Beyond. *Adv. Phys. X* **2017**, *2*, 373–408.

(47) Wang, Z.; Garg, A.; Wang, L.; He, H.; Dasgupta, A.; Zanchet, D.; Janik, M. J.; Rioux, R. M.; Román-Leshkov, Y. Enhancement of Alkyne Semi-Hydrogenation Selectivity by Electronic Modification of Platinum. *ACS Catal.* **2020**, *10*, 6763–6770.

(48) Ibach, H.; Lehwald, S. Identification of Surface Radicals by Vibration Spectroscopy: Reactions of C_2H_2, C_2H_4, and H_2 on Pt (111). *J Vac Sci Technol* **1978**, *15*, 407–415.

(49) Ibach, H.; Hopster, H.; Sexton, B. Analysis of Surface Reactions by Spectroscopy of Surface Vibrations. *Appl. Surf. Sci.* **1977**, *1*, 1–24.

(50) Kiskinova, M.; Pirug, G.; Bonzel, H. P. NO Adsorption on Pt(111). *Surf. Sci.* **1984**, *136*, 285–295.

4. SITE-SELECTIVE MODIFICATION OF METAL SURFACES BY METAL OXIDES

4.1 Abstract

Site-selective modification of metal catalysts is a promising approach to improve the activity and stability. For example, Mo doped Pt_3Ni catalyst is one of the best catalysts for electrocatalytic oxygen reduction reaction, where Mo was proposed to form surface oxides preferentially on the vertex and edge sites of the nanoparticle, preventing the dissolution of Ni and enhancing the durability. However, detailed experimental observations of the site preference of surface Mo oxides are lacking. Herein, we studied the structure of surface Mo oxides on Pt(111) and Pt(544) surfaces using scanning tunneling microscopy (STM), X-ray photoelectron spectroscopy (XPS), and high-resolution electron energy loss spectroscopy (HREELS). At 0.08 ML coverage, Mo oxide forms 1~2 nm clusters and the majority of Mo is in +5 oxidation state. The Mo oxide clusters tend to aggregate near the monoatomic Pt steps, showing a higher local density compared to the wide terraces. Therefore, such a site-selective modification is experimentally evidenced and could be potentially exploited in more catalytic systems.

4.2 Introduction

Metal nanoparticles usually expose both multiple low-index surfaces and unsaturated metal sites including steps, kinks, etc. Intrinsically, those sites may exhibit different catalytic properties, leading to the so-called structural sensitivity when the particle size or particle shape changes[1]. For example, N. Tian *et al.* synthesized tetrahexahedral Pd nanocrystals enclosed by {730} and vicinal high-index facets, which showed 4-6 times higher catalytic activity for ethanol electrooxidation than commercial Pd black, and they attributed the high catalytic activity to the high density of surface atomic steps on the tetrahexahedral Pd nanocrystals[2]. F. Calle-Vallejo *et al.* investigated the adsorption energies of reaction intermediates (*O, *OH, *OOH, $*OCH_3$) on different low-index, stepped and kinked surfaces of transition metals, and found that the coordination of the active site plays a main role in determining the scaling relations between the adsorption energies of oxygenates[3].

Since the complexity of the surface structure of metal nanoparticles is unavoidable, it has been of interest to researchers if certain sites can be passivated or modified by a second component. H. Wang *et al.* reported a site-selective blocking strategy via atomic layer deposition to selectively passivate the low-coordination sites or high-coordination sites of Pd nanoparticles with various particle sizes ranging from 2.1 to 19.1 nm[4]. By cycles of Al_2O_3 deposition, the low-coordination sites can be selectively blocked, while by cycles of FeO_x deposition, the high-coordination sites can be selectively blocked. The Pd catalysts were tested for aerobic oxidation of benzyl alcohol and both activity and selectivity showed a volcano relation with the Pd particle size. Owing to the site-selective blocking strategy, the geometric and electronic changed induced by the changing of particle size were able to be disentangled. The authors found that the geometric effect dominates the right side of the volcano with larger-size Pd particles while the electronic effect dominates the left side of the volcano with smaller-size Pd particles. Behind the strategy is the special interactions between metals and different types of oxides.

The structural sensitivity of the metal catalysts is also a key topic for the electrocatalytic oxygen reduction reaction (ORR), which is one of the most important reactions in energy conversion systems such as fuel cells[5]. Pt is the best single metal electrocatalyst for ORR reaction with high activity and durability under acidic conditions[6], and it has been found that the low-index facets of Pt have comparable activities towards this reaction, and in contrast, (211) steps are less active than the terraces[7]. Alloying Pt with a secondary metal was considered to improve the catalytic performance and reduce the usage of expensive Pt[8,9,10]. Pt-Ni catalysts show superior activity but suffer from low durability as Ni leaches out under acidic conditions[11]. X. Huang *et al.* found that by doping a third transition metal (Cr, Mn, Fe, Vo, Mo, Re, W) with Pt_3Ni nanostructures, the activity and durability can be enhanced[12]. Among them, the Mo-Pt_3Ni catalyst showed the best performance, and maintained high activity after 8000 cycles. A following study performed by the same group showed that Mo atoms are preferentially located on the vertex and edge sites of the Mo-PtNi/C catalyst in the form of oxides, which are stable within the potential window of the electrochemical cycle and thus protect Ni from acid dissolution, as evidenced by theoretical calculations[13]. Similarly, Mo doping in the Pt-Cu catalyst also improves the activity and stability for ORR reaction in acidic media[14].

To provide a detailed experimental evidence for the selective location of Mo oxides on Pt surface and give a deeper understanding about the structural and chemical nature of the Mo

dopant, we performed surface science studies on MoO_x/Pt(111) and MoO_x/Pt(544) model catalysts. The model catalysts were treated in O_2 and $NO/O_2/NO_2$ mixture to simulate the strong oxidative conditions for ORR reaction. By using STM and XPS, we investigated the site-selective growth of Mo oxides on the desired low-index surface and the undesired stepped surface where leaching happens more easily. STM showed that Mo oxide forms clusters with an average size around 1-2 nm on both Pt surfaces. On the Pt(111) surface, the local density of the Mo oxide clusters at the steps is significantly higher than the terraces, suggesting a preferential agglomeration at step sites. On the Pt(544) surface, due to the narrowed width of terraces, the distribution of Mo oxide seems evenly. The different growth modes on the low-index surface and stepped surface suggested the structural sensitivity of the interaction between Mo oxide and different Pt sites. XPS revealed that the surface Mo oxide mainly exhibits +5 oxidation state. HREELS showed that the surface Mo oxide clusters are free of hydroxylation upon hydrogen dose. From these results, we showed the feasibility of selective passivation of undercoordinated Pt step sites by Mo oxide clusters. We also extended the idea of selective passivation to the ZnO_x/Pt system. The growth of ZnO islands on Pt(111) is insensitive to different sites, but the structural sensitivity could be evoked by pre-oxidizing the surface of Pt. In summary, we explored the possibility of site-selective modification of metal surfaces by oxides.

4.3 Experimental methods

Experiments were carried out in an Omicron surface analysis cluster consisting of two ultra-high vacuum (UHV) chambers. The preparation chamber (base pressure is ~6×10^{-10} mbar) is equipped with gas manifolds, a Zn evaporator for physical vapor deposition (PVD), and a mass spectrometer (MS). The analysis chamber (base pressure is ~6×10^{-11} mbar) is equipped with room temperature Omicron scanning tunneling microscopy (STM), X-ray photoelectron spectroscopy (XPS), high-resolution electron energy loss spectroscopy (HREELS), and low energy electron diffraction (LEED).

The Pt(111) and Pt(544) single crystals were purchased from Princeton Scientific Corporation. The crystals are one side polished with roughness < 0.01 micron and orientation accuracy < 0.1 degree. The Pt crystals were cleaned by cycles of Ar^+ sputtering, annealing in 1×10^{-6} mbar of O_2, and annealing in UHV up to 943 K. The cleanliness of the crystal surfaces

was monitored by XPS. ZnO films on Pt(111) were prepared by oxidative deposition of metallic Zn in 1×10^{-7} mbar O_2 at room temperature, followed by post-oxidation in 5×10^{-7} mbar O_2 at 550 K for 10 minutes. The coverage of Zn on Pt was controlled by deposition parameters (current of the power supply and exposure time) and was calculated using the area of Zn $2p_{3/2}$ and Pt 4f XPS peaks under the assumption of a non-attenuating ZnO adlayer.[15] Therefore, one monolayer (ML) is defined as equivalent number of Zn atoms to the number of Pt atoms in a Pt monolayer throughout the paper. This approach has been well validated and is described in detail elsewhere.[16,17] MoO_x films on Pt(111) and Pt(544) surfaces were prepared by e-beam evaporation of metallic Mo in 5×10^{-6} Torr O_2 at room temperature followed by oxidation in O_2 or $NO/O_2/NO_2$ mixture at 623 K. The coverage of Mo is determined by calculating the area of Mo 3d and Pt 4f XPS peaks using the same method as Zn. The $NO/O_2/NO_2$ mixture is made by pre-mixing of NO and O_2 in a small cylinder which is connected to the preparation chamber via a leak valve. After days NO_2 formed as the product of $NO+O_2$ reaction, and the concentration of this gas mixture is determined by mass spectrometer.

After oxide film preparation, the sample stage was cooled fast, and the sample was then transferred within 1-2 minutes to the analysis chamber for characterization by HREELS, STM, LEED and XPS. HREELS measurements were performed using an ELS 5000 (LK Technologies). The scattered electrons were collected with a 60° incidence angle and a 50° reflection angle with primary electron beam energy of 7 eV. The FWHM of the elastic peak of samples was between 2.5~3.5 meV (equivalent to 20~48 cm^{-1}). The intensity of energy loss was normalized to the intensity of the elastic peak.

XPS data were collected using a non-monochromatic Mg Kα x-ray source at an incidence angle of 45°. The emitted photoelectrons were collected using Omicron EAC 125 analyzer and Omicron EAC 2000 analyzer controller at a photoelectron emission angle of 45° with respect to the surface normal. XPS data were analyzed using CasaXPS software. Since the sample is conductive and grounded, no charge correction was necessary. The Pt $4f_{7/2}$ peak for the clean Pt(111) surface was observed at 71.0 eV. The background was subtracted using linear or Shirley line shape, and the peak was fitted using a Lorentzian asymmetric line shape with a tail damping parameter. During the fitting, the full width at half maximum (FWHM) was set to be equal for different Mo oxidation states.

STM imaging was performed at a constant current mode at room temperature with tungsten tips, which were prepared by electrochemical etching of 0.25 mm (or 0.175 mm) tungsten wires and cleaned by electron bombardment in UHV. The bias voltage varied from +0.8 to +1.5 V with tunneling current ranging from 0.4 to 0.8 nA. STM images were analyzed using WSxM software.[18]

4.4 Site-selective growth of MoO_x films on Pt(111)

The clean Pt(111) surface shows wide terraces and monoatomic (111) steps due to miscut of the crystal, providing a platform for the study of selective growth of molybdenum oxides. STM was used to visualize the growth of Mo after oxidation deposition and post-oxidation steps. As shown in Figure 4.1 a and b, 0.08 ML Mo is randomly dispersed on the Pt(111) surface and forms clusters right after oxidative deposition. After post-oxidation in 1×10^{-5} Torr O_2 at 623 K for 10 minutes, the clusters agglomerate and form films (Figure 4.1 c,d). The apparent height of the films is 1.2 Å (the apparent height measured based on the local density of states may not be the true physical height), indicating that the film is one monolayer thick. Notably, the local coverage near the monoatomic steps (boxed by white dashed line) is higher than that on the wide terraces, i.e. the step is selectively blocked by MoO_x. The sample is further oxidized in a $NO/O_2/NO_2$ mixture, in which NO_2 serves as a stronger oxidant than O_2. The second oxidation resulted in more dispersed MoO_x clusters with an average diameter of 1.6 nm, but the decoration of the steps can still be clearly seen (Figure 4.1 e,f).

The oxidation states of Mo are monitored by XPS. As shown in Figure 4.2, after oxidative oxidation, the Mo 3d spectrum showed a major peak at 230.2 eV with a shoulder on the higher binding energy side. After the first oxidation in pure O_2, the peak shifted to 231.0 eV, and after the second oxidation in the mixture, the peak position did not change while the peak shape is narrowed. A. M. Robinson *et al.* studied a 0.40 ML MoO_x/Pt(111) sample using ambient pressure XPS and ascribed the peaks at 229.8 eV and 231.2 eV to Mo^{4+} and Mo^{5+}, respectively[19]. Mo^{5+} does not exist in bulk molybdenum oxides but may exist in ultrathin oxide films provided the electronic interaction with metal substrates. In their study, Mo^{5+} took part of 85% in the sample after strong oxidation in 0.6 Torr O_2 at 800 K. Therefore, we considered the co-existence of Mo^{4+}, Mo^{5+}, and Mo^{6+} species in our sample and performed peak fitting. The peak

deconvolution results are listed in Table 4.1. The as-deposited sample contains primarily Mo^{4+} species, and the oxidized sample contains 80% Mo^{5+} and 20% Mo^{6+}. Even under the harsh oxidative conditions with the presence of NO_2, the majority of Mo maintain in +5 state,

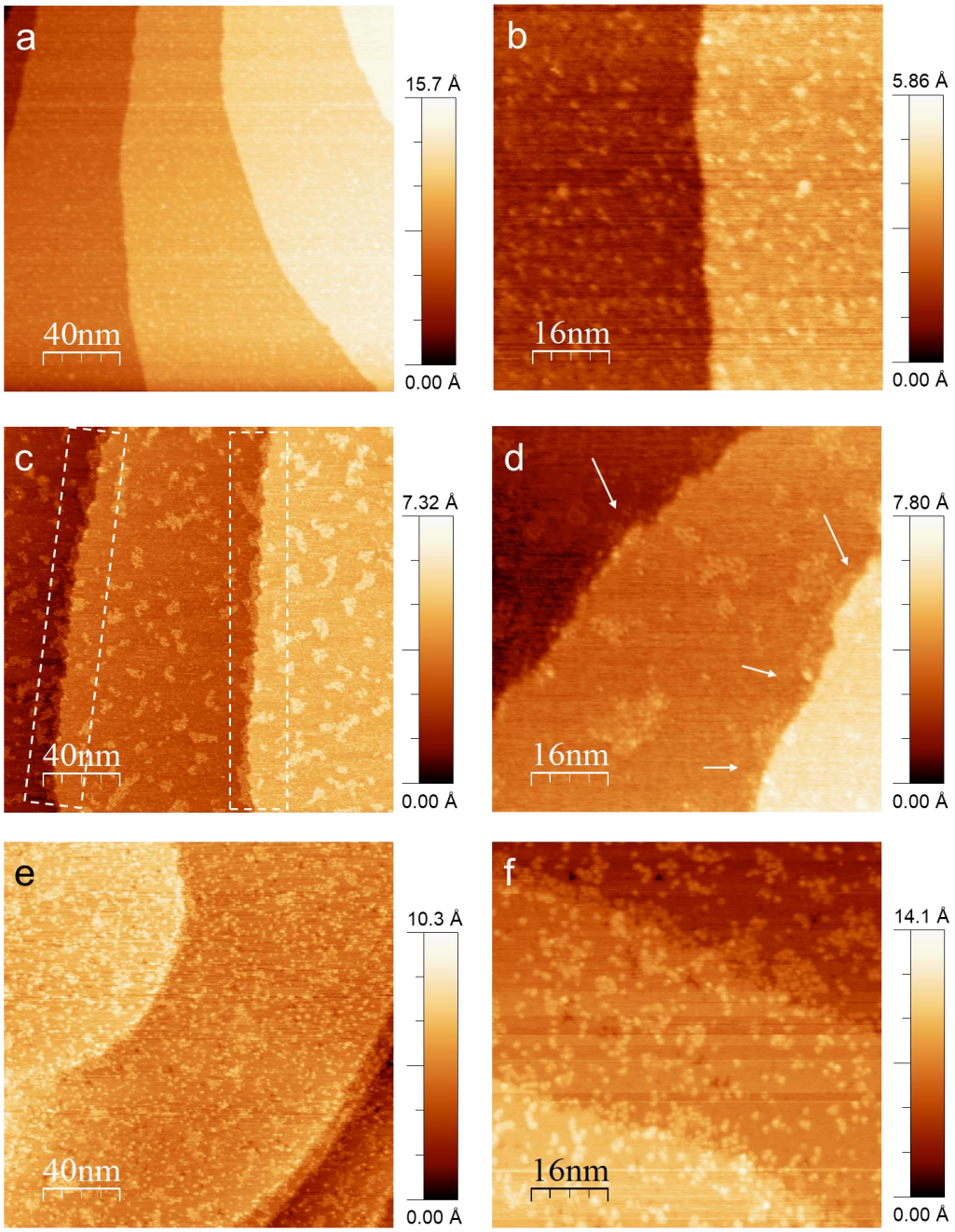

Figure 4.1. STM images of MoO_x clusters and films deposited on Pt(111). The coverage of Mo is 0.08 ML. Two sizes of images (200×200 nm and 80×80 nm) are shown for each experimental step to show statistics and key features. (a, b) The Pt(111) surface after e-beam evaporation of metallic Mo in 5×10^{-6} Torr O_2. (c, d) Surface after the first post-oxidation in 1×10^{-5} Torr O_2 at 623 K for 10 minutes. (e, f) Surface after the second post-oxidation in 1×10^{-5} Torr $NO/O_2/NO_2$ mixture (with a ratio of 20:70:10) at 623 K for 10 minutes.

indicating that a fully oxidized state (Mo^{6+}) cannot be achieved due to the electronic interaction with Pt when the coverage of Mo is within sub monolayer range. The O:Mo ratio was also determined by calculating the relative selectivity factor (RSF) corrected peak area of O 1s and Mo 3d peaks, which indicates the composition of the MoO_x clusters or films. The O:Mo ratio of the as-deposited sample is 1.9 and increases to 2.3 for the O_2 treated surface. After the treatment in $NO/O_2/NO_2$, the O:Mo ratio increased to 7.0, suggesting that 30-40% of surface Pt is also oxidized under the strong oxidative condition as well.

Table 4.1. XPS analysis of Mo oxidation states in the 0.08 MoO_x/Pt(111). The binding energy of $3d_{5/2}$ component of each oxidation state is listed.

Treatment conditions	FWHM (eV)	Mo^{4+} (eV)	Mo^{4+} area%	Mo^{5+} (eV)	Mo^{5+} area%	Mo^{6+} (eV)	Mo^{6+} area%	O:Mo ratio
As deposited	1.4	230.1	54	231.3	32	232.5	14	1.9
Oxidized in O_2	1.5	--	--	231.1	80	232.7	20	2.3
Oxidized in $NO/O_2/NO_2$	1.3	--	--	231.1	81	232.5	19	7.0

HREELS analysis shows the surface vibrations of Mo oxide clusters on Pt(111). As shown in Figure 4.3, bridging and linear CO peaks were observed at 1845 and 2085 cm^{-1}, respectively. The ν(CO) frequencies are consistent with those on clean Pt(111), suggesting negligible electronic changes on surface Pt. The small peaks in the ν(CH) region are due to the contamination from residual hydrocarbons during long time experimental measurements. Notably, no ν(OH) was observed on the post-oxidized MoO_x/Pt(111), indicating the absence of spontaneous hydroxylation of the MoO_x clusters. No ν(OD) signal was observed after treating the sample in 1×10^{-6} Torr D_2 at room temperature for 10 minutes, confirming that the MoO_x clusters are resistant to hydroxylation. In aggregate, our results indicate that MoO_x mainly forms clusters and presents +5 oxidation state on Pt(111), and preferably occupies the step sites compared to the terraces.

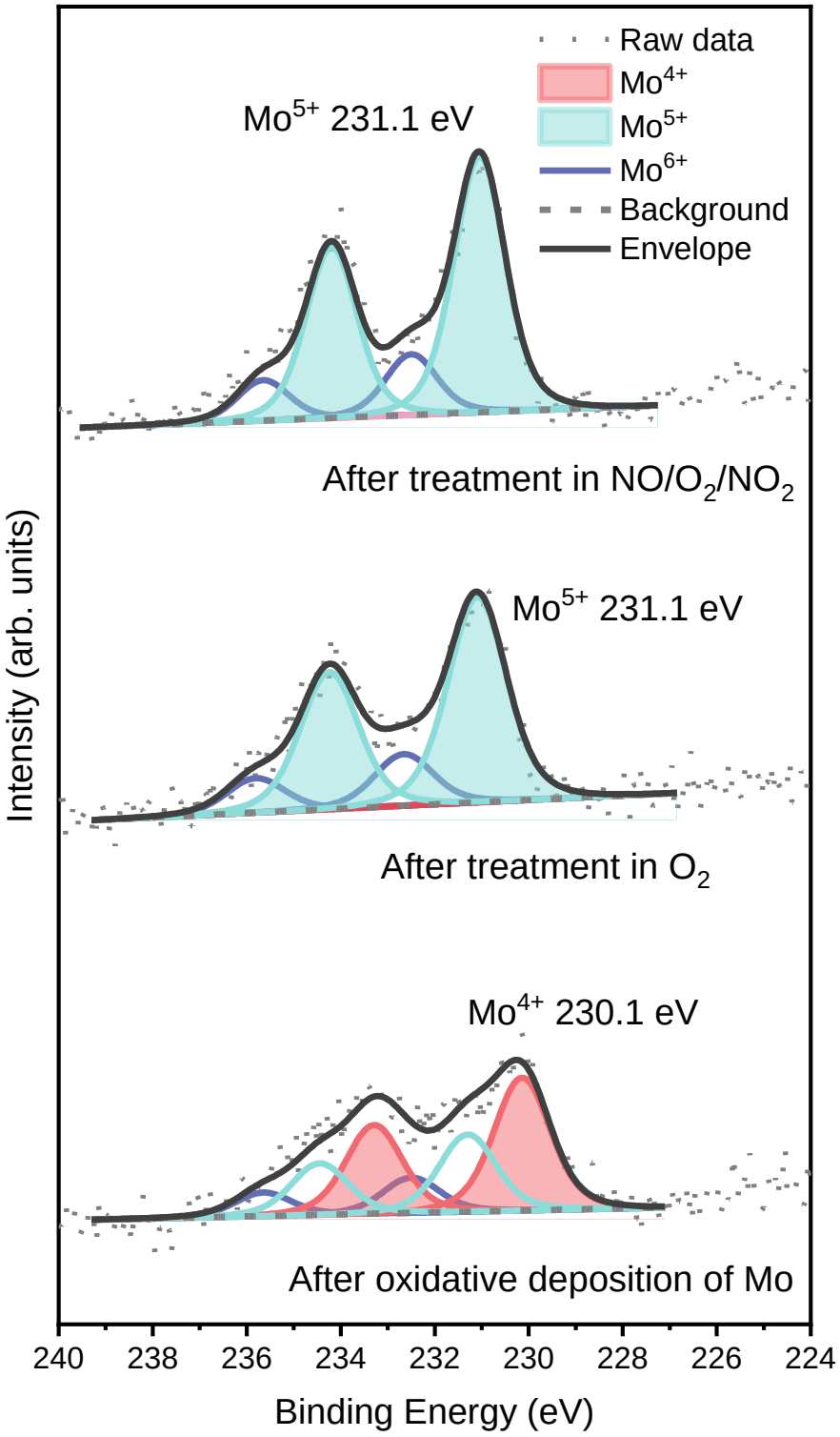

Figure 4.2. Mo 3d XPS spectra of the 0.08 ML MoO_x/Pt(111) sample after oxidation deposition, O_2 treatment, and $NO/O_2/NO_2$ treatment.

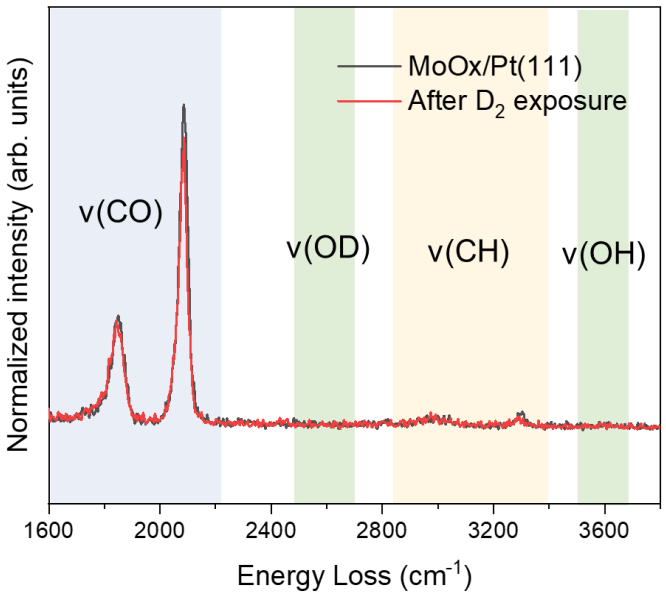

Figure 4.3. HREELS spectra of the MoO_x clusters on Pt(111) after post-oxidation in $NO/O_2/NO_2$ (black line) and after treatment in 1×10^{-6} Torr D_2 at room temperature for 10 minutes (red line).

4.5 Site-selective growth of MoO_x films on Pt(544)

Step surfaces served as an idea model to investigate the growth of oxides at step sites. Among all available step surfaces, Pt(544) were chosen to compromise between step density and acceptable terrace width for STM imaging. The Pt(544) stepped surface contains (100) steps and (111) terraces with 9 atoms on each terrace, as shown in Figure 4.4. STM image shows the width and height of the terraces are not even, indicating that the real surface might be the mix of mono-atomic and bi-atomic steps. The average width of the terrace is 2.2 nm, and the average height is 2.1 Å, in agreement with the simulated model.

Mo oxides on Pt(544) were prepared using the same method as on Pt(111). The coverage of Mo was controlled at 0.08 ML as well. Similar to MoO_x/Pt(111), Small clusters were randomly dispersed on the surface after oxidative deposition, as shown in Figure 4.5a. It is worth noting that for better eye guidance, the whole image was flattened, so the brightness does not necessarily correspond to the height. After oxidation in O_2, the terraces appeared to be wider, as shown in Figure 4.5b. Clusters are observed on the terraces, with an average diameter of 1.2 nm. In addition to the clusters, there are bigger extrusions observed, which will be referred to as

"film" in order to be distinguished from the "cluster". There are two possible explanations for the widening of the terraces: 1) the monolayer Mo oxide films cover one of two adjacent terraces so that the two terraces appear at the same horizontal level; 2) Mo oxide induced restructuring of the stepped Pt.

After the second oxidation, the surface coverage increased a lot. Treating the bare Pt(544) surface under the same condition resulted in the formation of Pt oxide clusters, as shown in Figure 4.5d, therefore, the clusters observed in Figure 4.5c contain both Mo oxides and Pt oxides. It is worth noting that the size of clusters formed by oxidizing bare Pt(544) is smaller than the size of clusters formed by oxidizing the MoO_x/Pt(544), and the terrace width of the former sample was kept the same as the clean stepped surface. By comparing the two samples, it can be concluded that MoO_x partly aggregates on the narrow terraces and induced the widening of them.

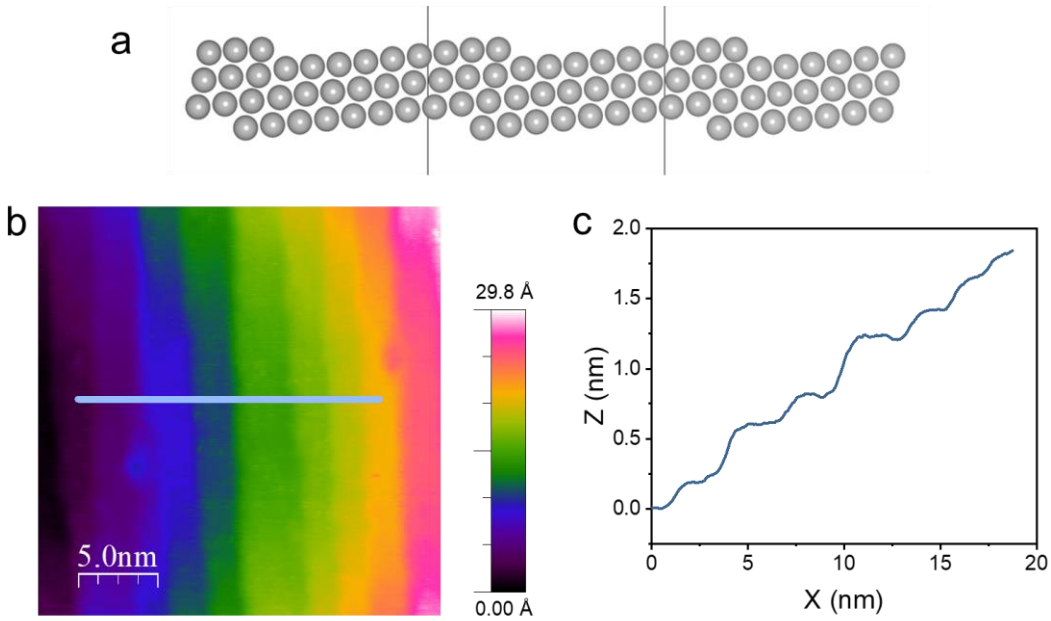

Figure 4.4. (a) Model of the Pt(544) stepped surface. (b) STM image of the bare Pt(544) surface. (c) The histogram along the line in b.

XPS resolved the oxidation states of Mo on the stepped surface (Figure 4.6). Again, the co-existence of Mo^{4+}, Mo^{5+}, and Mo^{6+} species were considered when fitting the data. It turned out that the as-deposited Mo contains 22% Mo^{4+}, 58% Mo^{5+}, and 20% Mo^{6+}. It is likely that the stepped Pt shows a higher activity towards oxygen dissociation and thus half of the deposited Mo

was oxidized to Mo^{5+} right after room temperature deposition. After O_2 treatment, all Mo^{4+} was further oxidized into Mo^{5+}, resulted in 77% Mo^{5+} and 23% Mo^{6+}. After the second treatment in the mixture, the sample contains 82% Mo^{5+} and 18% Mo^{6+}. Similarly, the O:Mo ratio increased from 2 to 7.6 due to the oxidation of Pt under strong oxidative conditions. Again, HREELS analysis showed that Mo oxide on Pt(544) is resistant to hydroxylation (spectrum not shown). In short, the composition of MoO_x clusters formed on Pt(111) and Pt(544) are similar. The formation of film on the Pt(544) surface is consistent with the aggregation of clusters on the steps of Pt(111), and the potential restructuring of Pt(544) suggests a strong interaction between MoO_x and Pt step sites.

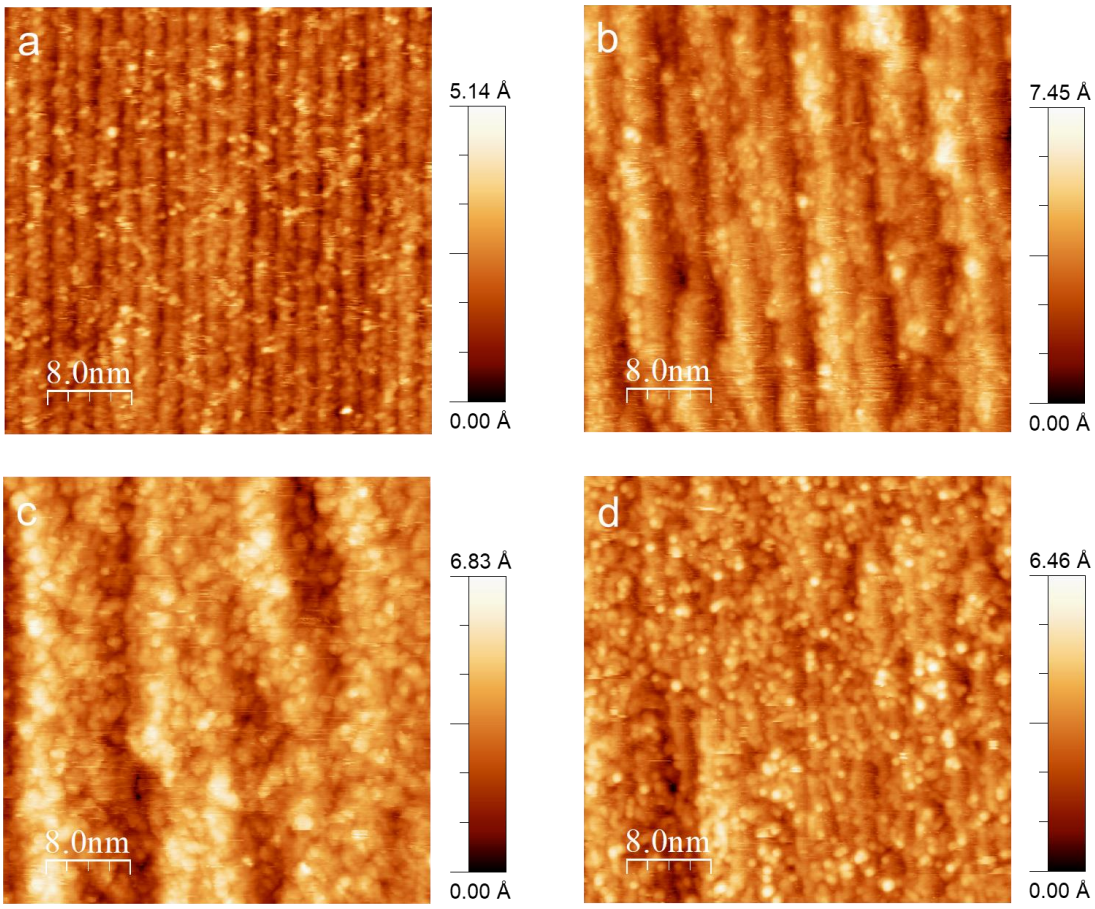

Figure 4.5. (a-c) STM images of 0.08 ML MoO_x/Pt(544) sample. (a) The Pt(544) surface after e-beam evaporation of metallic Mo in 5×10^{-6} Torr O_2. (b) Surface after the first post-oxidation in 1×10^{-5} Torr O_2 at 623 K for 10 minutes. (c) Surface after the second post-oxidation in 1×10^{-5} Torr $NO/O_2/NO_2$ mixture (with a ratio of 20:70:10) at 623 K for 10 minutes. (d) The bare Pt(544) surface treated in 1×10^{-5} Torr $NO/O_2/NO_2$ mixture (with a ratio of 20:70:10) at 623 K for 10 minutes. All the STM images were flattened in order to give better eye guidance, and the contrast does not correspond to the real height.

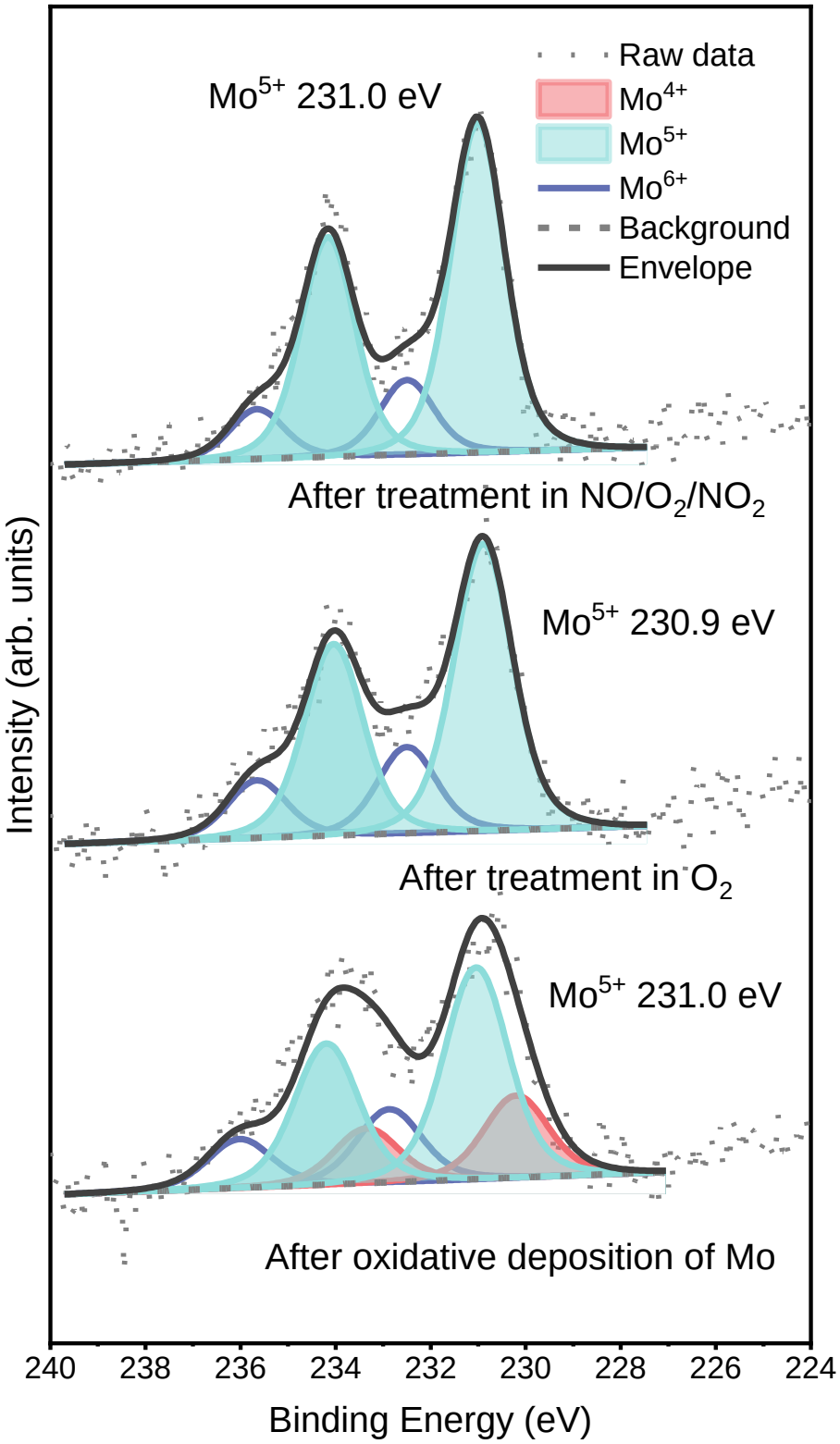

Figure 4.6. Mo 3d XPS spectra of the 0.08 ML MoO_x/Pt(544) sample after oxidation deposition, O_2 treatment, and $NO/O_2/NO_2$ treatment.

Table 4.2. XPS analysis of Mo oxidation states in the 0.08 MoO_x/Pt(544). The binding energy of $3d_{5/2}$ component of each oxidation state is listed.

Treatment conditions	FWHM (eV)	Mo^{4+} (eV)	Mo^{4+} area%	Mo^{5+} (eV)	Mo^{5+} area%	Mo^{6+} (eV)	Mo^{6+} area%	O:Mo ratio
As deposited	1.6	230.2	22	231.0	58	232.9	20	2.1
Oxidized in O_2	1.5	--	--	230.9	77	232.5	23	1.9
Oxidized in $NO/O_2/NO_2$	1.4	--	--	231.0	82	232.5	18	7.6

4.6 Site-selective growth of ZnOx films on Pt(111)

We also studied if such a site-selective growth is universal for other ultrathin oxide/metal systems, and if not, could it be achieved by pre-treating the metal substrates. Thus, the ZnO_x/Pt system was revisited. As discussed before, oxidative deposition of Zn and post-oxidation in 5×10^{-7} mbar resulted in the formation of the graphite-like ZnO structure, as shown in Figure 4.7a. Triangular islands and films formed on the surface, with the monoatomic steps partially covered. No obvious selective growth from steps was observed. Therefore, the step segregation of MoO_x at Pt steps is unique due to the properties of the oxides.

In contrast, the growth mode of ZnO changed when the Pt(111) was pre-exposed to O_2. Surface Pt oxide was formed by exposing the Pt(111) to 5×10^{-7} mbar O_2 at 583 K for 10 minutes, and then Zn was deposited onto the O/Pt(111) surface at room temperature. As shown in Figure 4.7b, zinc oxide triangular islands dispersed randomly on the terraces, and the entire monoatomic step was decorated by smaller triangular islands on both sides. It is hypothesized that the surface oxide formed at the steps show a higher reactivity with the deposited metallic Zn, leading to the oxide decoration of the steps. Therefore, it is demonstrated that preferential growth of oxides at certain step sites can be achieved by changing the properties of the substrate.

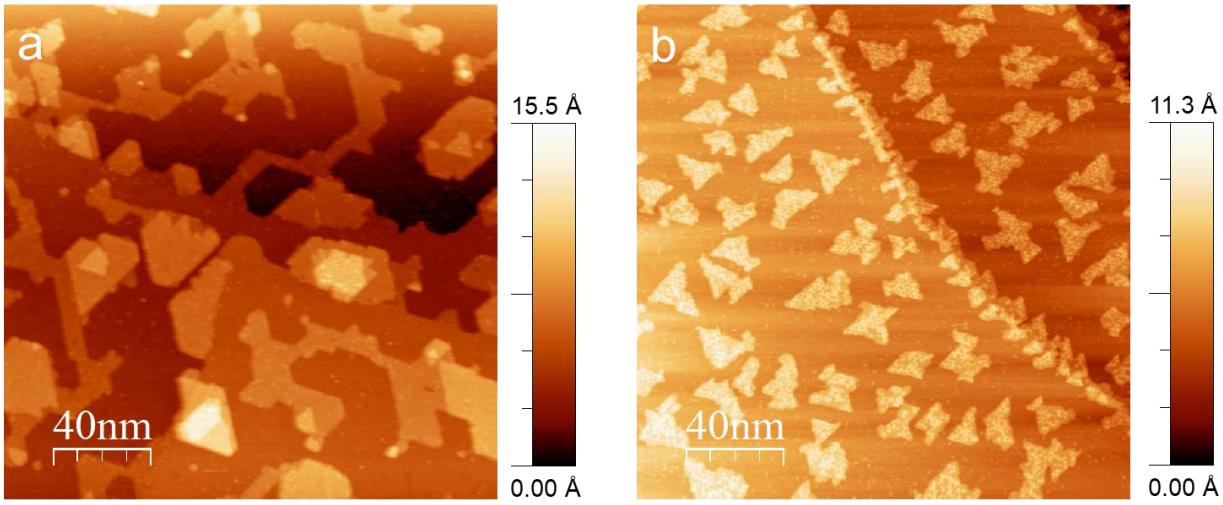

Figure 4.7. (a) STM image of the ZnO_x/Pt(111) surface prepared by oxidative Zn deposition in 1×10^{-7} mbar O_2 and post-oxidation in 5×10^{-7} mbar O_2 at 550 K for 10 minutes. (b) STM image of the ZnO_x/Pt(111) surface prepared by treating the Pt(111) substrate in 5×10^{-7} mbar O_2 at 583 K for 10 minutes followed by Zn deposition in 5×10^{-7} mbar O_2 at room temperature.

4.7 Conclusions

In this chapter, we studied the formation and structure of Mo oxides on the low-index and stepped surfaces of Pt. Oxidation treatment of the evenly dispersed Mo leads to the formation of 1-2 nm Mo oxide clusters on Pt(111), and the clusters tend to aggregate near the monoatomic steps, leading to a higher local density of Mo oxides at step sites compared to the (111) terraces. On the stepped Pt(544) surface, Mo oxide forms both clusters and films, in accompany with the widening of the terraces. The results supported the theoretical analysis of the site preference of Mo surface oxides in Pt-based electrocatalysts. The site-selective growth was also observed in the ZnO_x/Pt system by pre-treating the Pt(111) in O_2 prior to the deposition of zinc oxide. Therefore, the site-selective modification of metal catalyst was conceptually validated and could be exploited for better catalyst design.

4.8 References

(1) Zhou, K.; Li, Y. Catalysis Based on Nanocrystals with Well-Defined Facets. *Angew. Chemie Int. Ed.* **2012**, *51*, 602–613.

(2) Tian, N.; Zhou, Z. Y.; Yu, N. F.; Wang, L. Y.; Sun, S. G. Direct Electrodeposition of Tetrahexahedral Pd Nanocrystals with High-Index Facets and High Catalytic Activity for Ethanol Electrooxidation. *J. Am. Chem. Soc.* **2010**, *132*, 7580–7581.

(3) Calle-Vallejo, F.; Loffreda, D.; Koper, M. T. M.; Sautet, P. Introducing Structural Sensitivity into Adsorption-Energy Scaling Relations by Means of Coordination Numbers. *Nat. Chem.* **2015**, *7*, 403–410.

(4) Wang, H.; Gu, X. K.; Zheng, X.; Pan, H.; Zhu, J.; Chen, S.; Cao, L.; Li, W. X.; Lu, J. Disentangling the Size-Dependent Geometric and Electronic Effects of Palladium Nanocatalysts beyond Selectivity. *Sci. Adv.* **2019**, *5*, 1-9.

(5) Keith, J. A.; Jacob, T. Theoretical Studies of Potential-Dependent and Competing Mechanisms of the Electrocatalytic Oxygen Reduction Reaction on Pt(111). *Angew. Chemie Int. Ed.* **2010**, *49*, 9521–9525.

(6) Sui, S.; Wang, X.; Zhou, X.; Su, Y.; Riffat, S.; Liu, C. jun. A Comprehensive Review of Pt Electrocatalysts for the Oxygen Reduction Reaction: Nanostructure, Activity, Mechanism and Carbon Support in PEM Fuel Cells. *J. Mater. Chem. A* **2017**, *5*, 1808–1825.

(7) Greeley, J.; Rossmeisl, J.; Hellman, A.; Nørskov, J. K. Theoretical Trends in Particle Size Effects for the Oxygen Reduction Reaction. *Zeitschrift fur Phys. Chemie* **2007**, *221*, 1209–1220.

(8) Stamenkovic, V. R.; Fowler, B.; Mun, B. S.; Wang, G.; Ross, P. N.; Lucas, C. A.; Markovic, N. M. Improved Oxygen Reduction Activity on $Pt_3Ni(111)$ via Increased Surface Site Availability. *Science.* **2007**, *315*, 493–497.

(9) Bu, L.; Guo, S.; Zhang, X.; Shen, X.; Su, D.; Lu, G.; Zhu, X.; Yao, J.; Guo, J.; Huang, X. Surface Engineering of Hierarchical Platinum-Cobalt Nanowires for Efficient Electrocatalysis. *Nat. Commun.* **2016**, *7*, 1–10.

(10) Zhu, E.; Li, Y.; Chiu, C. Y.; Huang, X.; Li, M.; Zhao, Z.; Liu, Y.; Duan, X.; Huang, Y. In Situ Development of Highly Concave and Composition-Confined PtNi Octahedra with High Oxygen Reduction Reaction Activity and Durability. *Nano Res.* **2016**, *9*, 149–157.

(11) Cui, C.; Gan, L.; Heggen, M.; Rudi, S.; Strasser, P. Compositional Segregation in Shaped Pt Alloy Nanoparticles and Their Structural Behaviour during Electrocatalysis. *Nat. Mater.* **2013**, *12*, 765–771.

(12) Huang, X.; Cao, L.; Chen, Y.; Zhu, E.; Lin, Z.; Li, M.; Yan, A.; Zettl, A.; Wang, Y. M.; Duan, X.; Mueller, T. High-Performance Transition Metal – Doped Pt_3Ni Octahedra for Oxygen Reduction Reaction. *Science.* **2015**, *348*, 1230–1234.

(13) Jia, Q.; Zhao, Z.; Cao, L.; Li, J.; Ghoshal, S.; Davies, V.; Stavitski, E.; Attenkofer, K.; Liu, Z.; Li, M.; Duan, X.; Mukerjee, S.; Mueller, T.; Huang, Y. Roles of Mo Surface Dopants in Enhancing the ORR Performance of Octahedral PtNi Nanoparticles. *Nano Lett.* **2018**, *18*, 798–804.

(14) Luo, Y.; Kirchhoff, B.; Fantauzzi, D.; Calvillo, L.; Estudillo-Wong, L. A.; Granozzi, G.; Jacob, T.; Alonso-Vante, N. Molybdenum Doping Augments Platinum–Copper Oxygen Reduction Electrocatalyst. *ChemSusChem* **2018**, *11*, 193–201.

(15) Fadley, C. S. Basic Concepts of X-Ray Photoelectron Spectroscopy. *Electron Spectrosc. theory, Tech. Appl.* **1978**, *2*, 1–156.

(16) Paul, R.; Reifenberger, R. G.; Fisher, T. S.; Zemlyanov, D. Y. Atomic Layer Deposition of FeO on Pt(111) by Ferrocene Adsorption and Oxidation. *Chem. Mater.* **2015**, *27*, 5915–5924.

(17) Gharachorlou, A.; Detwiler, M. D.; Nartova, A. V.; Lei, Y.; Lu, J.; Elam, J. W.; Delgass, W. N.; Ribeiro, F. H.; Zemlyanov, D. Y. Palladium Nanoparticle Formation on TiO2(110) by Thermal Decomposition of Palladium(II) Hexafluoroacetylacetonate. *ACS Appl. Mater. Interfaces* **2014**, *6*, 14702–14711.

(18) Horcas, I.; Fernández, R.; Gómez-Rodríguez, J. M.; Colchero, J.; Gómez-Herrero, J.; Baro, A. M. WSXM: A Software for Scanning Probe Microscopy and a Tool for Nanotechnology. *Rev. Sci. Instrum.* **2007**, *78*, 013705–013712.

(19) Robinson, A. M.; Montemore, M. M.; Tenney, S. A.; Sutter, P.; Medlin, J. W. Interactions of Hydrogen, CO, Oxygen, and Water with Molybdenum-Modified Pt(111). *J. Phys. Chem. C* **2013**, *117*, 26716–26724.

5. SUMMARY

5.1 Summary of current work

The work in this dissertation elucidates some fundamental knowledge of metal-oxide interactions in heterogeneous catalysts by using surface science approaches. Through atomic-level characterization of inverse model catalysts, we investigated how the surface oxide films influence the properties of metals in various ways.

In Chapter 2, the dynamic transformations of the ZnO_x/Pd(111) model catalyst were studied. By treating the bilayer ZnO_xH_y islands under an intermediate condition, a new metastable monolayer structure was discovered, and alloy formation was shown to be the thermodynamic driving force for the migration of zinc species on Pd(111) surface. This discovery implies that the co-existence of SMSI and alloy formation should be considered for ZnO-metal systems. The experimental and theoretical combined study also provides a template to calibrate calculations using sophisticated UHV experiments and give reliable predictions under real reaction conditions.

In Chapter 3, a unique open $Zn_6O_5H_5$ structure was focused. This structure shows a strong metal-hydroxide interaction different from traditional metal-oxide interactions. It is highlighted that compact oxide films form oxide-metal interfaces as a new type of active sites, but the properties of the metal itself remain unchanged. However, open structures could provide two types of modification simultaneously by forming new interfaces and tuning the electronic properties of metal. More than this specific $Zn_6O_5H_5$ structure studied in this work, it is likely that other open structures could also show the similar dual effects. Therefore, the geometry of oxide/hydroxide films needs more attention when designing metal-oxide interfaces for certain reactions.

In Chapter 4, the site-selective passivation of Pt step sites by intentional doping of oxides was investigated. Mo oxide was found to migrate towards the monoatomic steps, demonstrating the feasibility of utilizing a second oxide component to passivate certain active sites. Extra deposition of oxides could be used as a new approach to tune the catalytic surface more proactively and precisely.

Overall, these findings emphasize the necessity of understanding the atomic-level structure of catalytic surfaces and dynamic changes of the structure depending on reaction conditions. Those findings could shed light on more effective and rational design of oxide supported metal catalysts.

5.2 Possible future directions

Based on the projects conducted in this dissertation, there are several topics which could be considered for future work.

5.2.1 Structure sensitivity of ZnO SMSI

The structure sensitivity of metal-oxide interactions between different crystallographic facets in metal nanoparticles and oxide supports plays a significant role in catalytic properties but remains underexplored. In the SMSI condition, the nanoparticle is partially or completely covered by an oxide overlayer, and the overlayer changes with reaction conditions, resulting in a more complicated system. M. G. Willinger *et al.* reported that Pt particle on Fe_3O_4(111) film, exhibiting both Pt(111) and Pt(100) facets, was completely encapsulated by FeO(111) layer in SMSI state, as observed by HRTEM[1]. STM studies of iron oxide monolayer film on Pt(100) substrate show hexagonal FeO(111) layer on square Pt lattice[2], which also supports the insensitivity of SMSI in Pt/Fe_3O_4 system.

The thermodynamic stability of oxide overlayer comes from the difference between cohesion energy of oxide bulk and adhesion energy of oxide film to metal surface, which is a good descriptor for the quantification of the metal-oxide interaction. In the case of iron oxide on Pt(100), the formation of a hexagonal FeO(111) layer regardless of the substrate-overlayer lattice mismatch suggests that the interaction within the FeO layer is stronger than that with Pt substrate. However, the FeO(111) film on Pt(100) is less stable compared to that on Pt(111) upon annealing in O_2 at 1000 K[2], therefore, the stability of oxide overlayer on different low-index facets of metal substrate is still worth investigating. Moreover, this insensitivity has never been confirmed on other oxide supports, like ZnO. It is intuitive that the adhesion energy of oxide films on metal surfaces will be influenced by lattice symmetries. For example, the graphite-like depolarized ZnO (0001) film epitaxially grown on Pt(111), Pd(111) and Ag(111) is in hexagonal symmetry, which matches the symmetry of (111) surface of a face centered cubic (FCC) metal

crystal and mismatches the rectangular symmetry of (110) surface and square symmetry of (100) surface, thus, the structure may not form on (110) and (100), or may form in a distorted fashion. The stability of the film is also expected to change accordingly.

To compare the structure and transformations of ultrathin zinc oxide films on Pd(100) and Pd(111), some preliminary experiments have been done and the results are summarized here. Zinc oxide was formed by oxidative evaporation of Zn and post-oxidation in 1×10^{-6} mbar O_2 at 620 K. As shown in Figure 5.1a, zinc oxide formed discontinuous islands on Pd(100). Surface Pd was also oxidized during the post-oxidation step, forming the $(\sqrt{5}\times\sqrt{5})R27°$-PdO structure[3]. This PdO structure decomposed gradually in UHV in hours, leaving small holes on the surface (circled by white dashed line). Most of the zinc oxide is in bilayer form, with an apparent height of 3.0 Å (labeled as BL). There are also a few monolayer islands formed, with an apparent height of 1.3 Å (labeled as ML). Depositing zinc oxide under the same conditions resulted in the formation of 3.4 Å high bilayer islands on Pd(111), as shown in Figure 5.1b.

The two surfaces were treated in 5×10^{-7} mbar D_2/O_2 (1:4) mixture at 620 K for 10 minutes. It has been discussed in Chapter 2 that treating zinc oxide under the gas phase condition at 550 K led to the formation of a monolayer $(18\times18)R20°$ structure on the Pd(111) surface. The same transformation occurred at 620 K, as shown in Figure 5.1d (labeled as ML). The high resolution image in Figure 5.1f confirmed the $(18\times18)R20°$ structure. This monolayer ZnO film formed due to short time treatment and will convert to near-surface alloys if treated further in the D_2/O_2 mixture. In contrast, treating ZnO_x/Pd(100) for 10 minutes resulted in complete reduction of Zn. As shown in Figure 5.1c, the surface coverage decreased a lot, and the patches show an apparent height of 2.0 Å, as the same height of monoatomic Pd steps, indicating that the patches are Pd (Figure 5.1e). Zn LMM auger spectra also confirmed that Zn was reduced to metallic state on Pd(100), while Zn was in a mix of monolayer oxide and metallic state on Pd(111) (spectra not shown). Therefore, the reduction of zinc occurs faster on Pd(100) than on Pd(111). In real catalytic systems, it is possible that the (111) facets are covered by oxide while the (100) facets show alloy as the topmost layer.

Future work could involve the study of the two surfaces after longer treatments to reach thermodynamic equilibrium. It is foreseeable that near-surface alloys would form on both Pd(100) and Pd(111) surfaces, but the composition might be different, due to the different abilities of dissolving heteroatoms. CO could be used as a probe molecule to study the adsorption

properties of the two surfaces. Phase diagrams of ZnO_x/Pd(100) could be established under UHV conditions and high pressure conditions, and Wulff construction[4] could be used to study any possible reconstruction of Pd nanoparticles during ZnO SMSI and PdZn alloy formation.

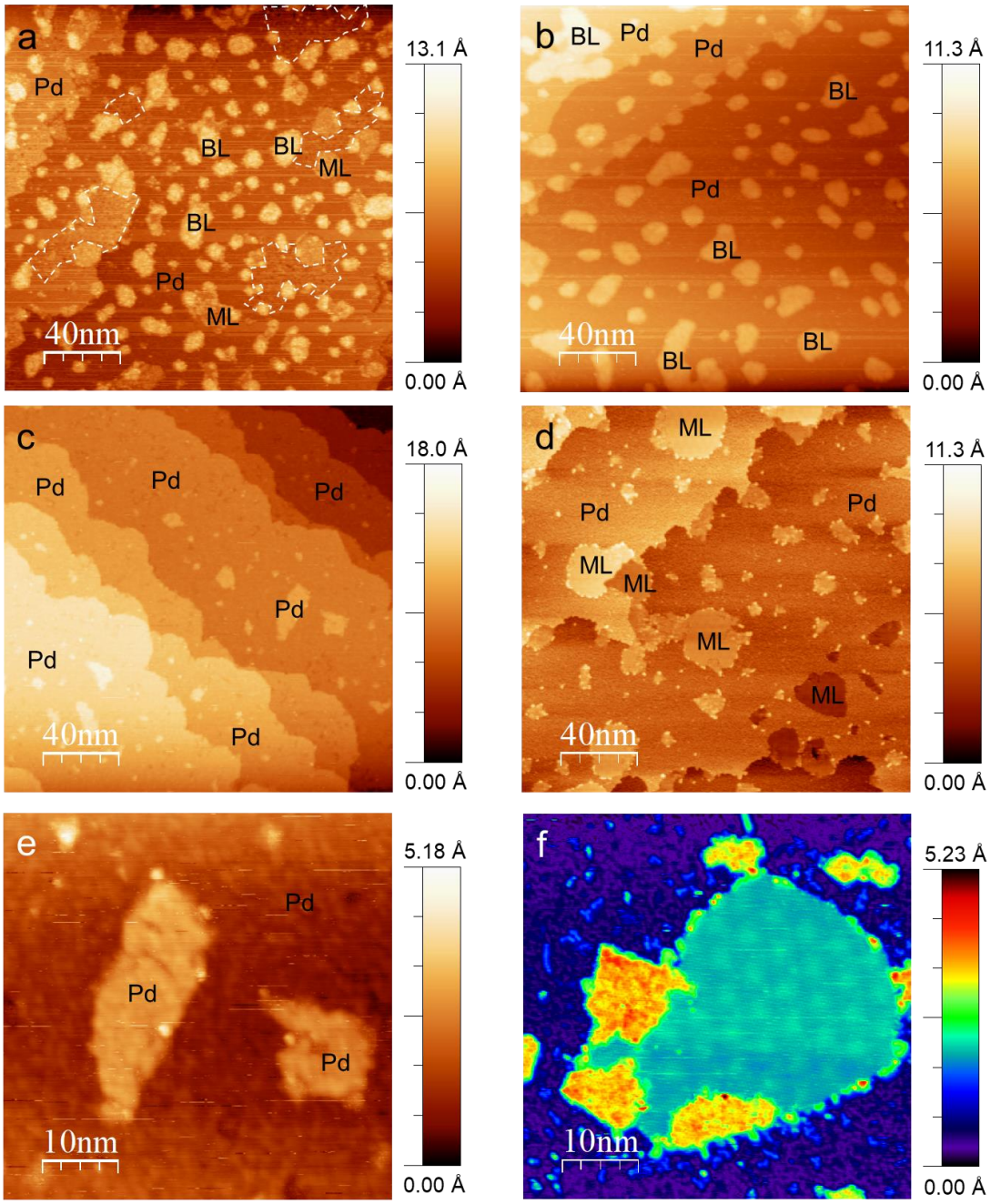

Figure 5.1. STM images of 0.4 ML ZnO_x/Pd(100) (a,c,e) and 0.3 ML ZnO_x/Pd(111) (b,d,f). (a,b) Zinc oxide islands formed by oxidative evaporation of Zn in 1×10^{-7} mbar O_2 following post-oxidation in 1×10^{-6} mbar O_2 at 620 K for 10 minutes. (c,d) The two surfaces after treatments in 5×10^{-7} mbar D_2/O_2 (1:4) at 620 K for 10 minutes. (e,f) High resolution images of the two surfaces shown in c and d.

5.2.2 Tuning the porosity of SMSI overlayer in technical catalysts

Surface science studies helped elucidate the fundamental thermodynamics and mechanisms of SMSI, while the understanding should be tested by technical catalyst system in turn. In Chapter 3, it has been demonstrated that the open zinc hydroxide structure allows the maximum usage of surface metal sites and shows electronic effect, while the compact and crystalline oxide overlayers are chemically inert to catalysis. It is hypothesized that porous oxide layers would promote the catalytic performance of SMSI catalysts, since they allow the access of metal sites, and show geometric and electronic effects to the metal surfaces. Therefore, exploring how to tune the porosity of SMSI oxide/hydroxide layers would be valuable for rational design of catalysts. Different preparation methods, gas phase compositions, and treatment temperatures could be used to tune the surface overlayer structure. DFT calculations could help make predictions for the surface structure, while XPS, XAS, TEM, CO-IR, and probe reaction tests could be used for structure characterization.

5.2.3 Improving the site selectivity of partial oxide coverage on metals

Extensive studies of SMSI demonstrated that the partial coverage of metal surfaces by oxides could improve the catalytic performance and stability for metal catalysts. Historically SMSI is a spontaneous process occurred during reduction of catalysts, and many studies focused on treating the catalyst precursors in reducing conditions to evoke a partial or full coverage of metal nanoparticles. In fact, the extra oxide overlayer could also be introduced by impregnation, atomic layer deposition (ALD), electro-deposition, etc. Efforts could be made to seek for a more accurate and selective way to grow oxides on metals.

For example, based on the work in Chapter 4, STM results showed that e-beam evaporation of metallic Mo resulted in evenly dispersed Mo on the surface regardless of the property of substrates. It is hypothesized that ALD might be used to improve the selectivity of Mo oxide growth. The interactions between organometallic ALD precursors (such as $(NtBu)_2(NMe_2)_2Mo$ and $Mo(CO)_6$) and substrates may make the first deposition step site selective. Then, with the migration of oxides in the post-oxidation step, the passivation could be more accurately.

5.3 References

(1) Willinger, M. G.; Zhang, W.; Bondarchuk, O.; Shaikhutdinov, S.; Freund, H. J.; Schlögl, R. A Case of Strong Metal-Support Interactions: Combining Advanced Microscopy and Model Systems to Elucidate the Atomic Structure of Interfaces. *Angew. Chemie Int. Ed.* **2014**, *53*, 5998–6001.

(2) Shaikhutdinov, S.; Ritter, M.; Weiss, W. Hexagonal Heterolayers on a Square Lattice : A Combined STM and LEED Study of FeO(111) on Pt(100). **2000**, *62*, 7535–7541.

(3) Kostelník, P.; Seriani, N.; Kresse, G.; Mikkelsen, A.; Lundgren, E.; Blum, V.; Šikola, T.; Varga, P.; Schmid, M. The Pd (100)-(√5×√5)R27°-O Surface Oxide: A LEED, DFT and STM Study. *Surf. Sci.* **2007**, *601*, 1574–1581.

(4) Ringe, E.; Van Duyne, R. P.; Marks, L. D. Wulff Construction for Alloy Nanoparticles. *Nano Lett.* **2011**, *11*, 3399–3403.

APPENDIX. SUPPLEMENTARY INFORMATION FOR CHAPTER 2

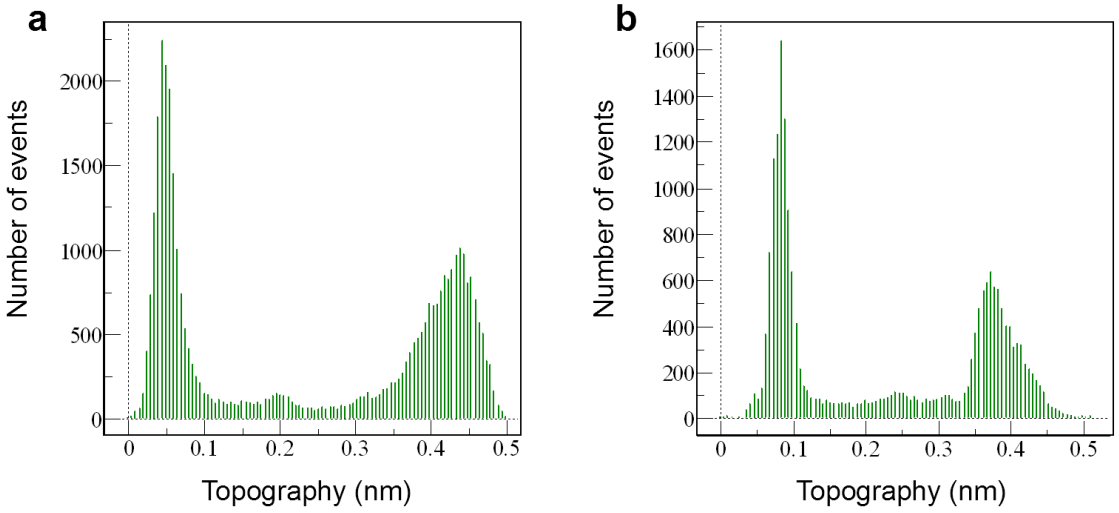

Figure S1. Histogram of apparent height of (a) the upper region and (b) the lower region of a bilayer island shown in Figure 2.2b.

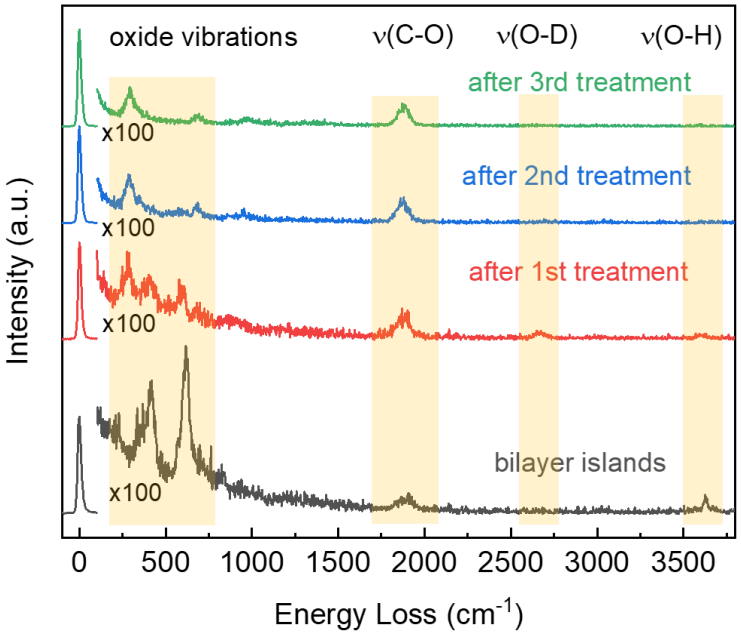

Figure S2. Wide range HREELS spectra of the 0.32 ML ZnO_x/Pd(111) sample after post-oxidation (forming bilayer islands) and sequential treatments in D_2/O_2. The narrow peaks on the left-hand side are elastic peaks with an intensity set to 1. The intensity of energy loss signal was magnified 100 times.

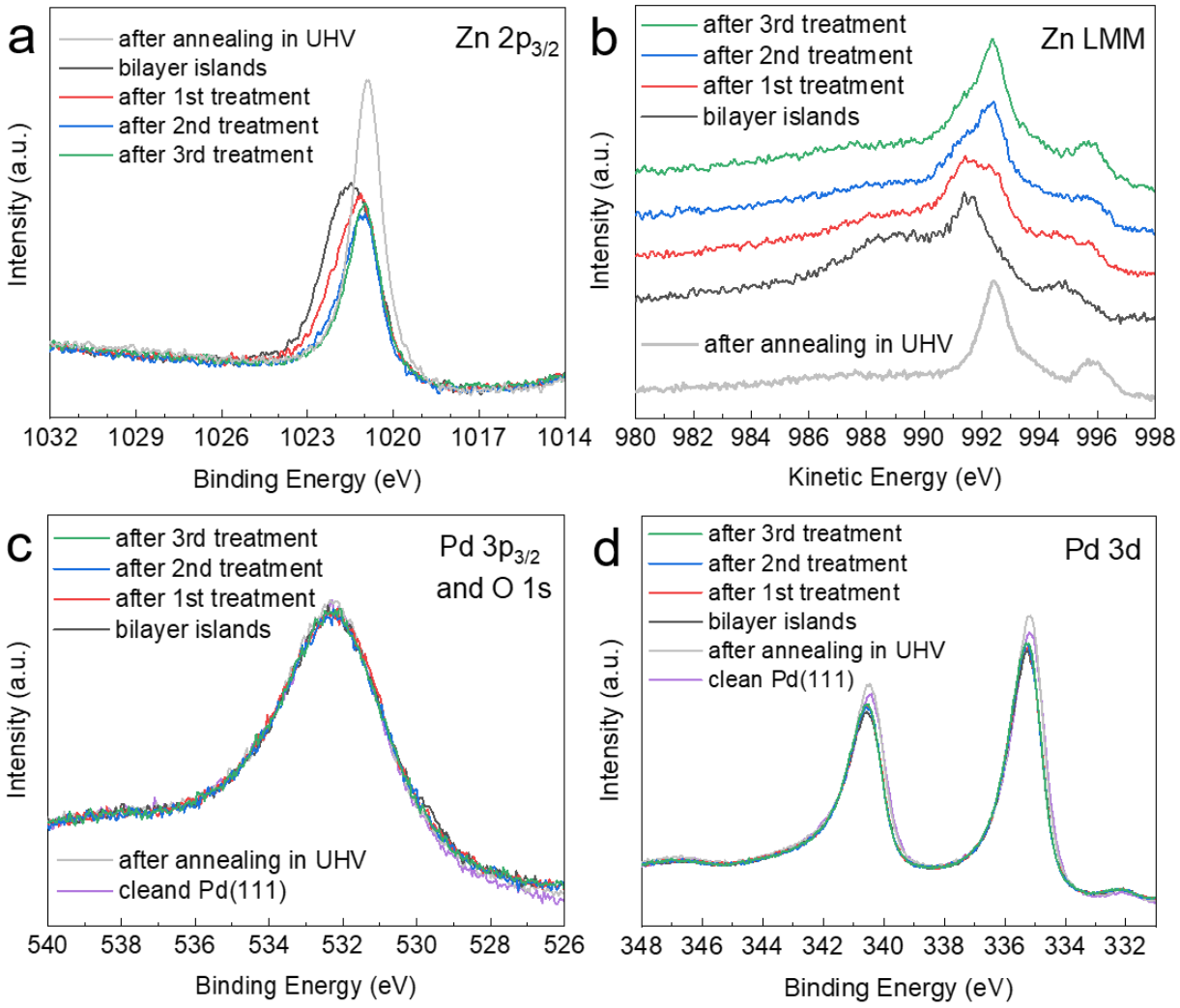

Figure S3. XPS peaks of the 0.32 ML ZnO_x/Pd(111) sample after diethylzinc deposition and annealing in UHV, after post-oxidation (forming bilayer islands), and after sequential treatments in D_2/O_2. (a) Zn 2p3/2 peaks (same data as Figure 3). (b) Zn LMM auger peaks. (c) Pd $3p_{3/2}$ peaks. O 1s peaks are overlapped with Pd $3p_{3/2}$ peaks, and due to the small amount of oxygen compared to the Pd substrate, O 1s signal is not seeable in our case. Therefore, the spectra of the sample after each step are very similar to the spectrum of clean Pd(111). (d) Pd 3d peaks. Due to the small amount of deposited zinc oxide, the spectra of the sample are very similar to that of the clean Pd(111). The shift of the peak is smaller than 0.1 eV. The Pd $3d_{5/2}$ peak is centered at 335.2 eV, which is in well agreement with metallic Pd and supporting that no charge correction is needed during XPS measurements.

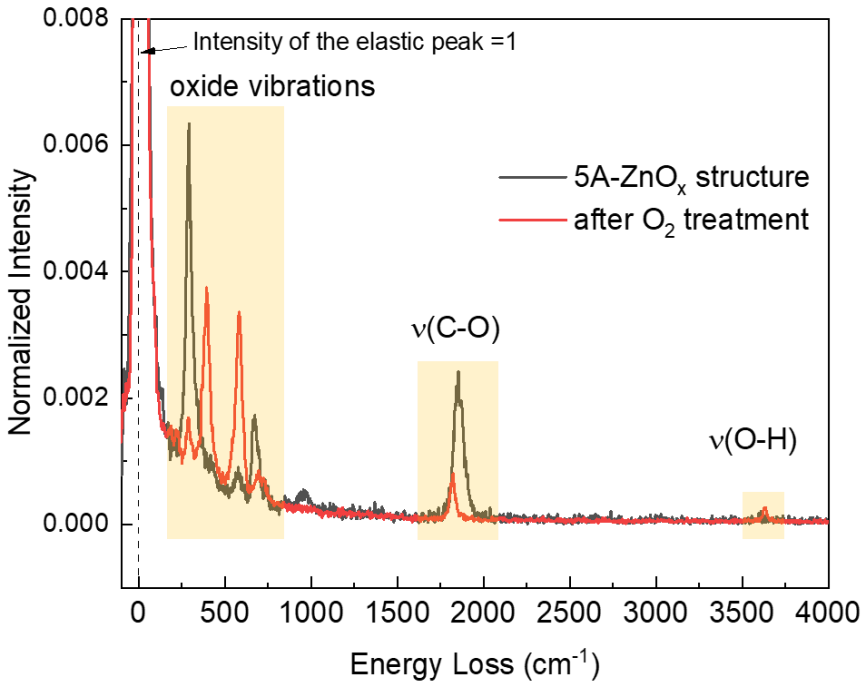

Figure S4. Wide range HREELS spectrum of the 0.33 ML ZnO_x/Pd (111) sample with dominant 5Å-ZnO_x structure (black line) and surface after re-oxidation in O_2 at 5×10^{-7} mbar at 550 K for 10 min.

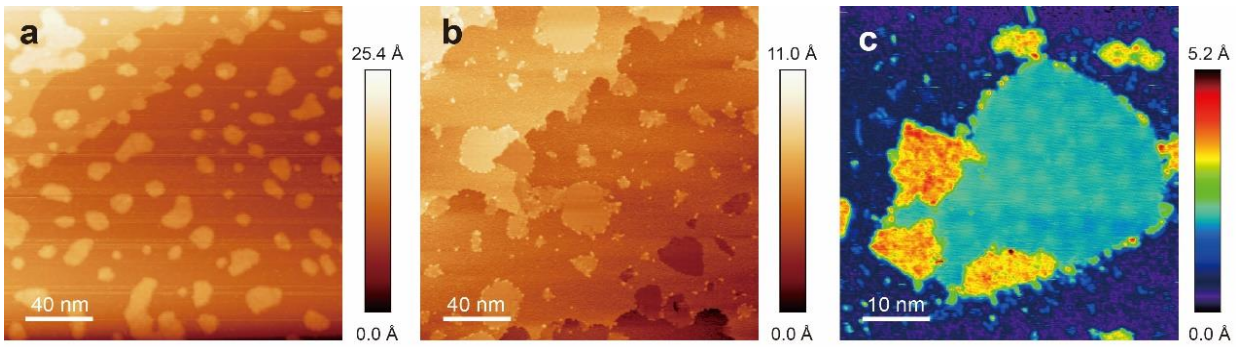

Figure S5. STM images of (a) the as-prepared 0.28 ML ZnO_x/Pd(111) surface with dominant bilayer islands and (b) the surface after treatment a in D_2/O_2 (1:4) mixture at 620 K with a dominant 5Å-ZnO_x structure. (c) Magnified image of a 5Å-ZnO_x monolayer island.

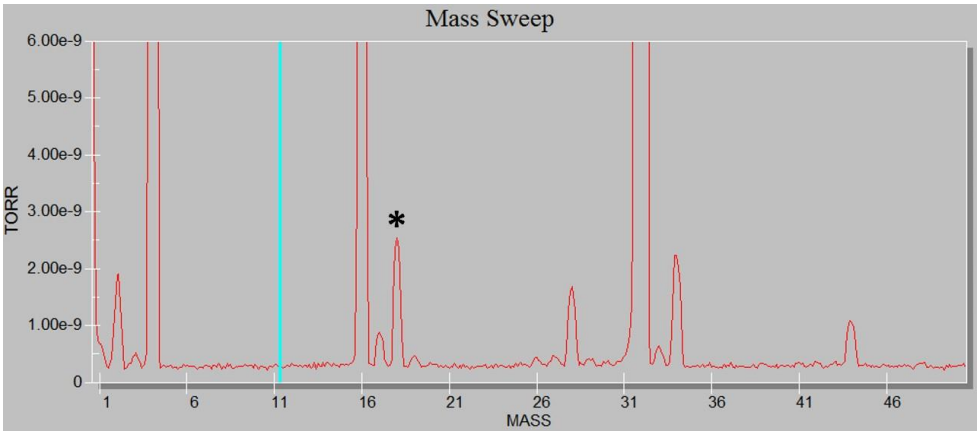

Figure S6. Mass spectrum of the gas phase collected during the treatment of bilayer islands in 5×10^{-7} mbar of a D_2/O_2 (1:4) mixture at 550 K. The asterisk marked peak at a mass-to-charge ratio 18 can be ascribed to H_2O and DO fragments.

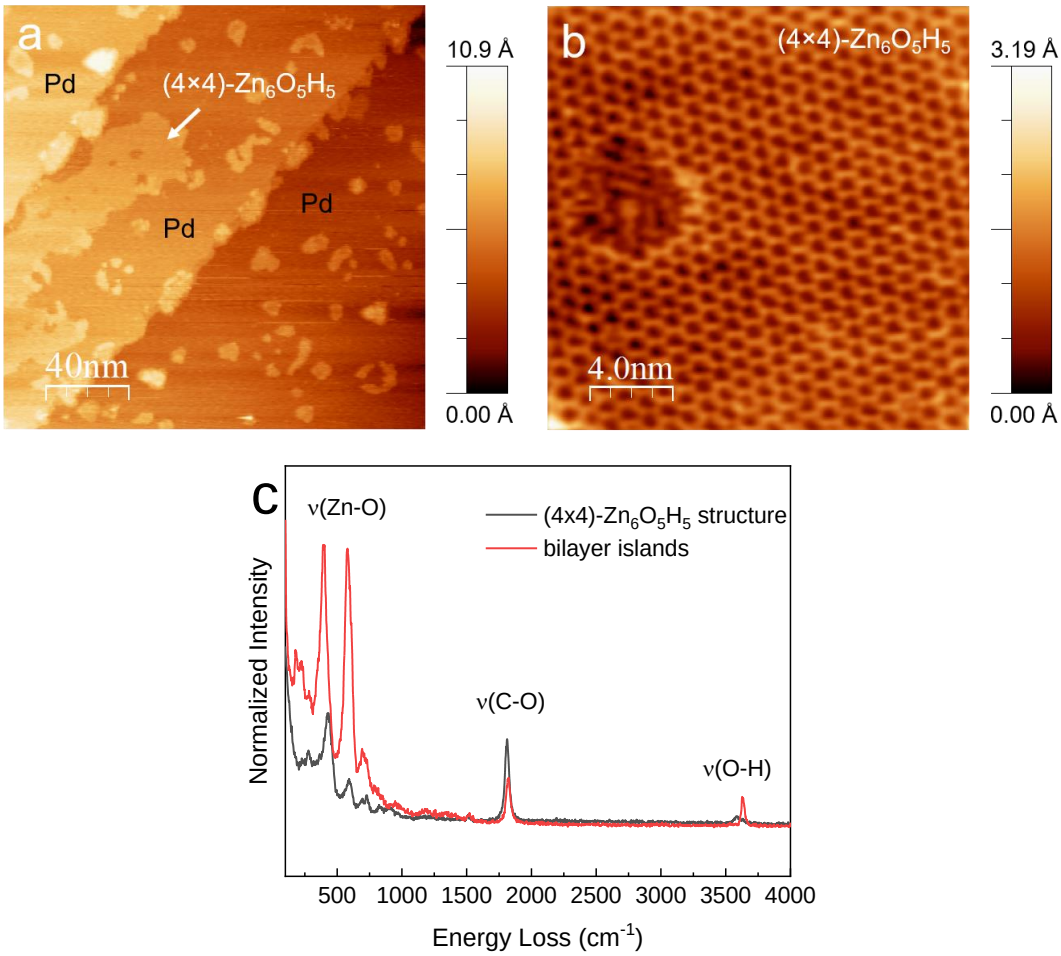

Figure S7. (a, b) STM images of the (4x4)-$Zn_6O_5H_5$ structure prepared by diethylzinc deposition and post-oxidation in 5×10^{-7} mbar O_2 at 550 K for 10 minutes. The Zn coverage is 0.14 ML. (c) HREELS spectrum of the (4x4) structure showing a different OH stretching frequency to that of bilayer islands.

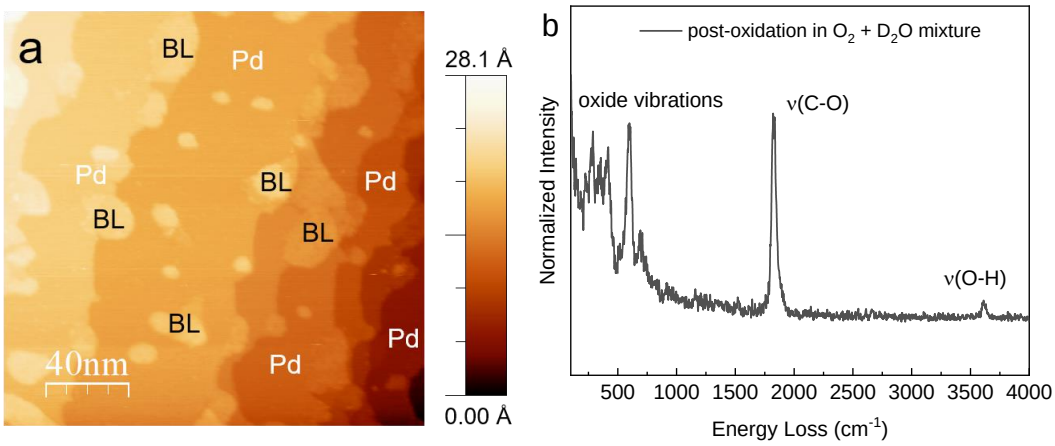

Figure S8. (a) STM images of the bilayer islands prepared by diethylzinc deposition and post-oxidation in 5×10^{-7} mbar $D_2O:O_2$ = 1:9 mixture at 550 K for 10 minutes. The Zn coverage is 0.32 ML. (b) HREELS spectrum of the surface showing no ν(O-D) vibration.

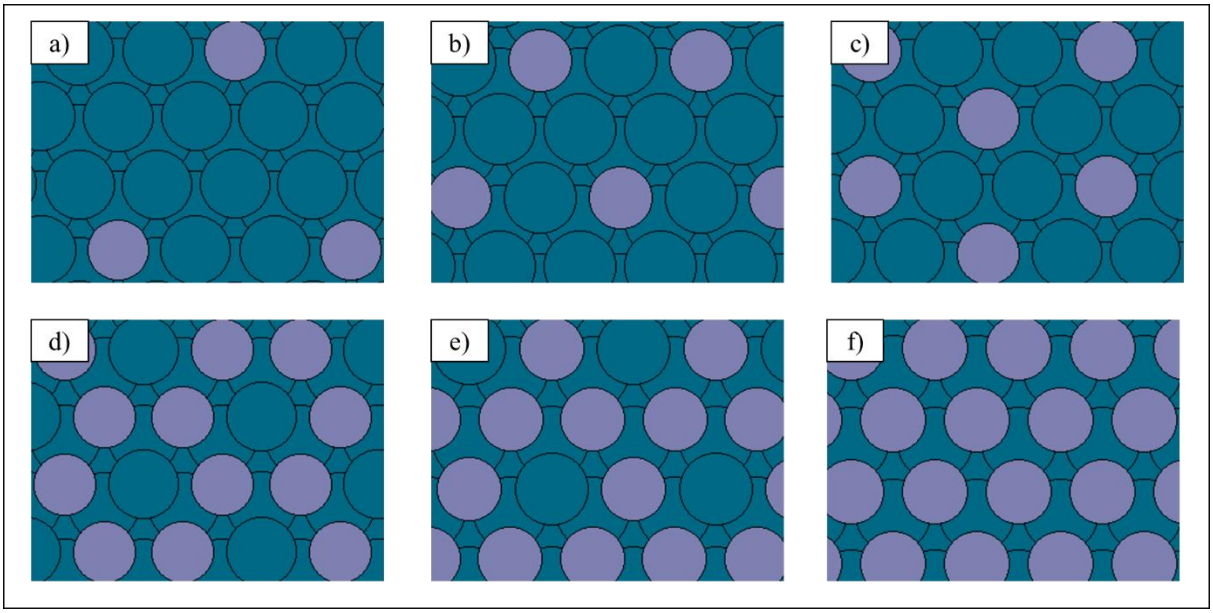

Figure S9. Surface alloy at different Zn/Pd ratios for the topmost layer. a) 0.11 b) 0.25 c) 0.33 d) 0.67 e) 0.75 f) 1.00.

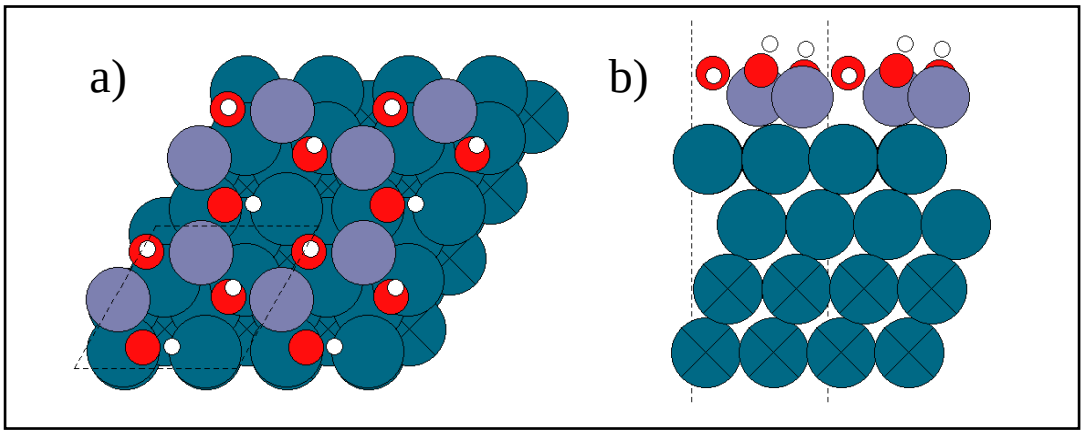

Figure S10. Monolayer $Zn_2O_3H_3$/Pd open structure. a) Top view b) Lateral view. The formation energy difference between the monolayer and bilayer is 0.02 eV/Zn.

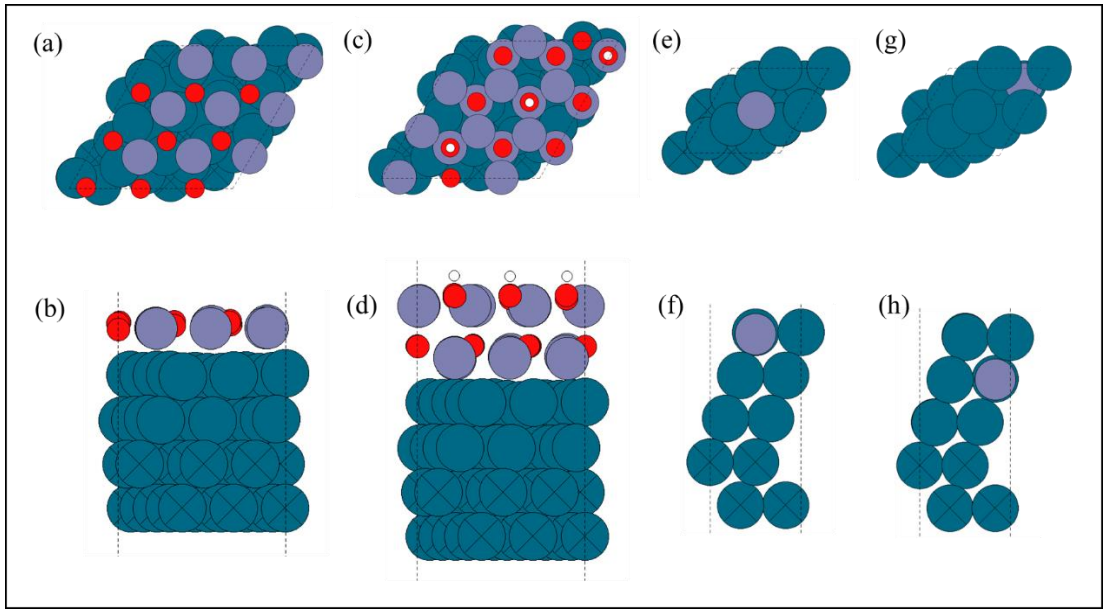

Figure S11. (a)Top and (b)side view of monolayer ZnO/Pd(111). (c)Top and (d)side view of bilayer ZnO/Pd(111) with 3/9 OH coverage. (e)Top and (f)side view of surface ZnPd alloy/Pd(111). (e)Top and (f)side view of subsurface ZnPd alloy/Pd(111).

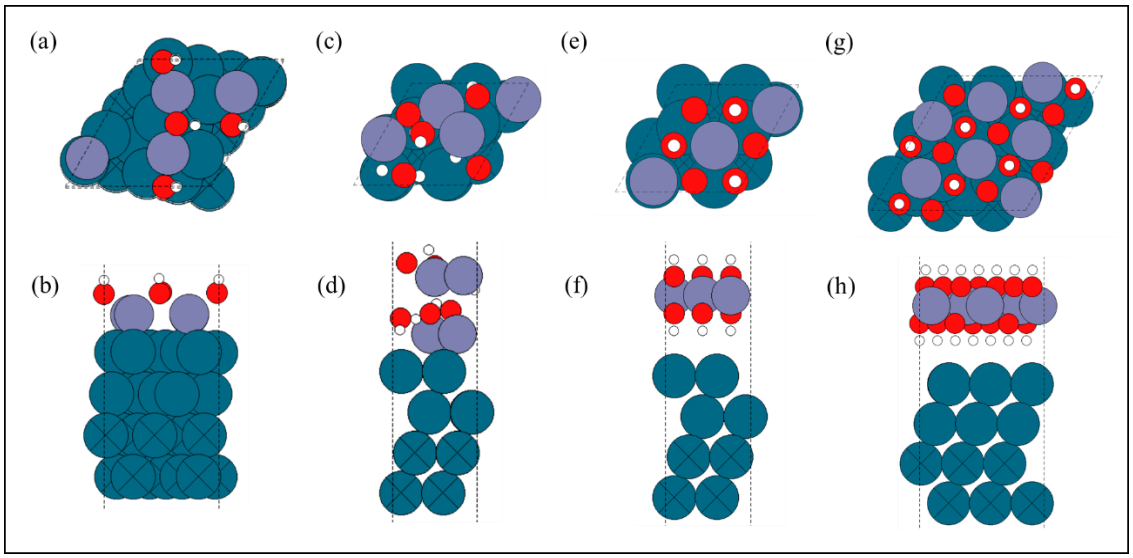

Figure S12. (a)Top and (b)side view of linear ZnOH/Pd(111) (Ratio:0.57). (c)Top and (d)side view of bilayer $Zn_2O_3H_3$/Pd(111) (Ratio:1.00). (e)Top and (f)side view of $Zn(OH)_2$/Pd(111) (Ratio:0.75). (e)Top and (f)side view of $Zn(OH)_2$/Pd(111) (Ratio:0.78).

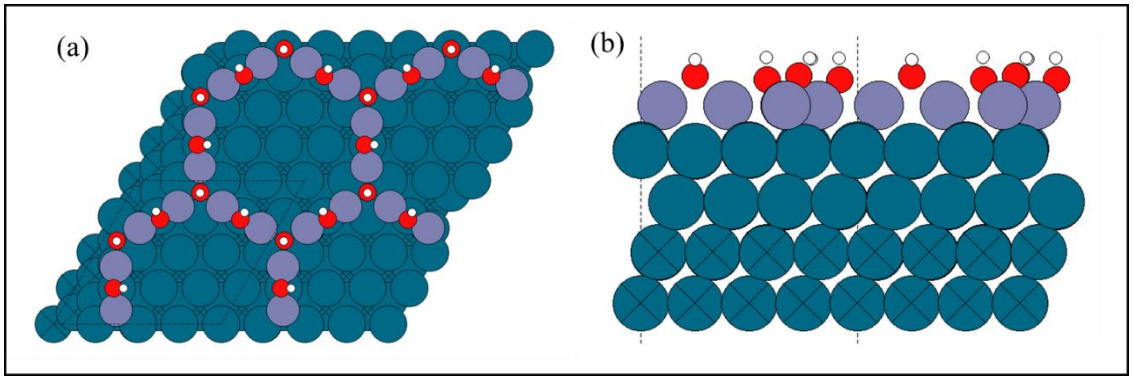

Figure S13. Monolayer $Zn_6O_5H_5$/Pd open structure. a) Top view b) Lateral view. This structure is known as the (4x4) structure in literature. (STM image – Figure S7)

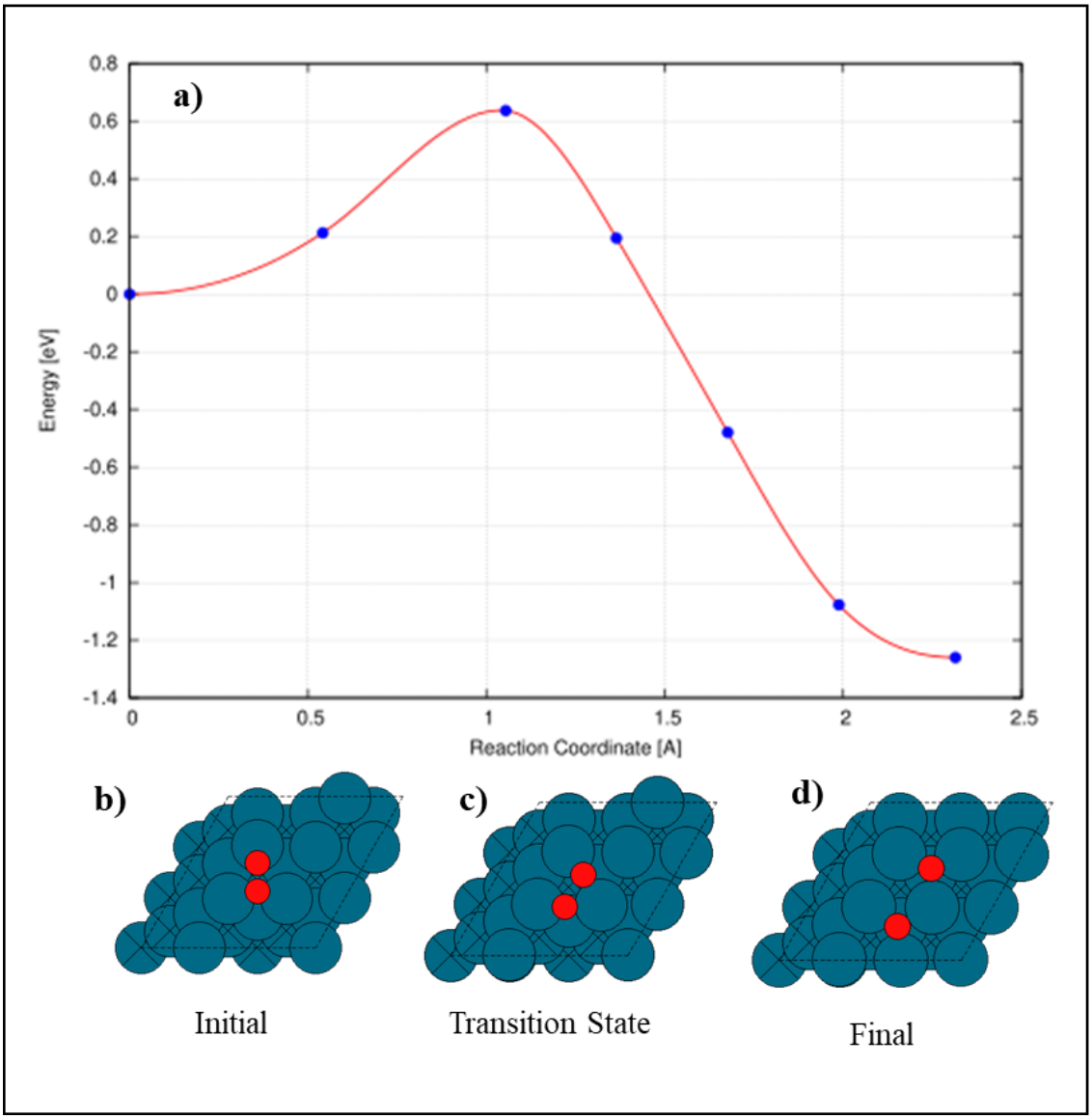

Figure S14. Nudged elastic band (NEB) calculations were performed using DFT-VASP-vtst codes. a) The energy is plotted against reaction coordinate to locate the transition state. (b,c,d) show the initial, transition state, and final state structures, respectively.

VITA

Junxian Gao was born to Xia Ding and Cao Gao in 1997. She grew up in Sixian, a small town in Anhui province, and then went to high school in Hefei, China. During high school, she was recommended by the principal for admission to Peking University. She studied in College of Chemistry and Molecular Engineering from 2014 to 2018. In the summer of 2016, she joined Dr. Ding Ma's group as an undergraduate researcher and worked on developing heterogenous catalysts for CO_2 hydrogenation and styrene hydroformylation. In the summer of 2017, she did a research intern on photocatalysis at University College London under the supervision of Dr. Junwang Tang. After obtaining her bachelor's degree in Chemistry from Peking University, she joined Davidson School of Chemical Engineering, Purdue University as a Ph.D. student, and started her work under the guidance of Dr. Jeffrey T. Miller and Dr. Dmitry Zemlyanov. Her dissertation research focused on surface science studies of strong metal-support interactions. She applied surface science techniques to investigate the structure and properties of ultrathin oxide films on metal surfaces. She graduated with a Ph.D. degree in Chemical Engineering in May 2022.

PUBLICATIONS

J. Gao, K. J. Sawant, J. T. Miller, Z. Zeng, D. Zemlyanov, J. P. Greeley. Structural and Chemical Transformations of Zinc Oxide Ultrathin Films on Pd(111) Surface. *ACS Appl. Mater. Interfaces.* **2021**, *13*, 35113-35123.

J. Z. Chen, J. Gao, P. R. Probus, W. Liu, X. Wu, E. C. Wegener, A. J. Kropf, D. Zemlyanov, G. Zhang, X. Yang, J. T. Miller. The Effect of Strong Metal-Support Interaction (SMSI) on Pt-Ti/SiO_2 and Pt-Nb/SiO_2 Catalysts for Propane Dehydrogenation. *Catal. Sci. Technol.* **2020**, *10*, 5973-5982.

R. Ma, T. Yang, J. Gao, J. Kou, J. Z. Chen, Y. He, J. T. Miller, D. Li. Composition Tuning of Ru-Based Phosphide for Enhanced Propane Selective Dehydrogenation. *ACS Catal.* **2020**, *10*, 10243-10252.

Z. Li, M. Dadsetan, J. Gao, S. Zhang, L. Cai, A. Naseri, M. Jimenez-castaneda, T. Filley, J. T. Miller, M. J. Thomson, V. G. Pol. Revealing the Thermal Safety of Prussian Blue Cathode for Safer Nonaqueous Batteries. *Adv. Energy Mater.* **2021**, *11*, 2101764.

J. Kou, J. Z. Chen, J. Gao, X. Zhang, J. Zhu, A. Ghosh, W. Liu, A. Kropf, D. Zemlyanov, R. Ma, X. Guo, A. Datye, G. Zhang, L. Guo, J. T. Miller. The Structural and Catalytic Properties of Isolated Pt^{2+} Sites in Platinum Phosphide (PtP_2). *ACS Catal.* **2021**, *11*, 13496-13509.

C. A. Milligan, R. R. Seemakurthi, J. Gao, J. P. Greeley, J. T. Miller, F. H. Ribeiro, D. Y. Zemlyanov. Structure-controlled Catalytic Properties of PdZn Near-surface Alloys. *J. Phys. Chem. C. under review*.

J. Gao, K. J. Sawant, Z. Zeng, D. Zemlyanov, J. P. Greeley, J. T. Miller. Tunning Pt catalytic surface by self-assembly of monolayer zinc hydroxy-oxide films, *manuscript in preparation*.